

Physics-based Modelling of Junction Fires at Laboratory Scale: Sensitivity, Validation and Parametric Studies

Ahmad HASSAN

Thesis submitted for the fulfilment of the requirements for the degree of
Masters of Research Practice

Victoria University, Australia

Institute of Sustainable Industries and Liveable Cities

August 2022

Abstract

The process of modelling and replicating extreme fire behaviour like junction fires is essential for understanding the phenomena associated with extreme fires. Junction fires – an extreme wildfire phenomenon – occur when two fire lines merge in a wildfire. The junction point's (apex) rate of spread and the fire intensity can quickly increase; this effect can be exacerbated by slopes and driving wind speed.

The aim of this study is to look into junction fire behaviour using a physics-based model. In particular, the study is aimed at examining the key factors that influence junction fire spread, namely slope angle, junction angle and driving wind speed.

A three-dimensional full physics-based model FIRESTAR3D, jointly developed by Aix-Marseille University, France, the Lebanese University, Lebanon, and Toulon University, France, was used in this study. For model validation, numerical simulations of laboratory-scale experiments of junction fire (conducted at the University of Coimbra, Portugal), replicating experiments with no imposed wind, were performed for a shrub fuel bed with slopes ranging from 0° to 30° . The simulations of junction fires were conducted for two junction angles, 30° and 45° . For each validation scenario, the sensitivities of the rate of spread (ROS) to various numerical, atmospheric and physical parameters were investigated. The behaviours of intersecting fire lines were explored in a parametric study for three crucial parameters (mentioned above) using the validated model.

In the validation study, the experimental trends of the compared quantities were well reproduced by the simulations. Accelerating and decelerating propagation phases were

observed in all simulations, with a dependence on the slope angle, while the maximum ROS depended critically on the junction angle. As was the case for wildfires in other studies simulated by FIRESTAR3D, it was found that this physics-based model is capable of simulating junction fire propagation. Validation tests performed using FIRESTAR3D for laboratory-scale experiments confirmed the potential of the model and provided a framework to extend the analysis to more general conditions, namely to explain the behaviour of real fires.

The results suggested that junction fire spread appears to be sensitive to conditions change; with a slight reduction in junction angle, the ROS can increase significantly. For junction angles lower than 30° , accelerative and decelerative behaviour is observed, while the junction angle 45° was found to be the threshold angle at which propagation becomes steady. The heat release rate (HRR) followed the opposite trend and it was found that the peak value over time rose with the increase in junction angle. This may be due to the slow ROS and longer residence time. With no slope, radiation is the dominant method of heat transfer, but convection dominates on sloped terrain.

In the case of wind-driven simulations of junction fire, strong interaction between fire lines was observed in response to wind, resulting in higher ROS. In the case of the 30° junction angle, junction point propagation and ROS were highly affected by both the slope and driving wind speed. However, for the cases with wider and narrower junction angles, the behaviour was not much affected by the driving wind speed. Considering the modes of heat transfer, higher wind velocity was accompanied by higher convection and lower

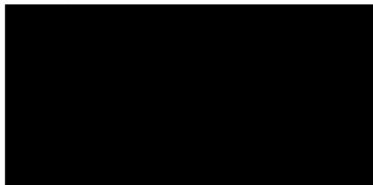
radiation for the cases with wide junction angles and non-sloped terrain; however, no significant changes were observed in the cases with higher slope.

Overall, the physics-based modelling conducted in this study provided some important insights into junction fire behaviour. The modelling process gave insights into many crucial parameters over wide ranges of slope angle, junction angle and wind speed, and allowed the development of a significant initial understanding of such phenomena at the laboratory scale. By better understanding junction fires, operational predictions and firefighter safety can be improved.

Declaration of Authenticity

I, Ahmad Hassan, declare that the Master of Research Practice thesis entitled 'Physics-based Modelling of Junction Fires at Laboratory Scale: Sensitivity, Validation and Parametric Studies' is no more than 50,000 words in length including quotes and exclusive of tables, figures, appendices, bibliography, references and footnotes. This thesis contains no material that has been submitted previously, in whole or in part, for the award of any other academic degree or diploma. Except where otherwise indicated, this thesis is my own work". "I have conducted my research in alignment with the Australian Code for the Responsible Conduct of Research and Victoria University's Higher Degree by Research Policy and Procedures.

Signature



Date 19/Aug/2022

Acknowledgements

The research work presented in this master's dissertation was conducted at Victoria University for one year. This period of research was a very worthwhile stage in my education, as well as in my personal development. The wise guidance of my scientific advisers and their continuous encouragement to investigate allowed me to improve my knowledge in the field of wildfire modelling and different research skills.

I particularly wish to express my sincere gratitude to my scientific advisers Professor Khalid Moinuddin and Professor Gilbert Accary, for their valuable guidance, support and consistent encouragement during my Masters. Their dedicated supervision and step-by-step guidance were essential for me to complete my thesis. I highly appreciate their outstanding scientific expertise, as well as their trust and incessant care to provide me with the best possible working conditions. I also want to express my appreciation for the effort expended in this work and for the critical reading and suggestions for the dissertations. I treasure their encouragement for me to participate in the IX International Conference on Forest Fire Research in Coimbra, Portugal (next November), and publish the research work in the International Journal of Wildland Fire.

I also would like to express my thanks to Doctor Duncan Sutherland for his valuable input, advice and expertise. His comments and suggestions were crucial for the fulfilment of this work.

I would like to thank all university officials and coursework instructors for their generous efforts in this exceptional year to ensure excellent study conditions. Thank you for the

generosity and the valuable opportunity. I am sincerely honoured for having had the exceptional opportunity to study within a world-class university and a leading research community.

I would like to thank the whole collaborative team working in Lebanon and France in the field of wildfire modelling who gladly shared with us all information we sought. The simulations were conducted at the Mesocentre, the computing facility of Aix-Marseille University, France. The work was partially funded by the Australian Research Council (grant DP210102540) and Victoria University.

Finally, I want to express my warmest thanks to my family who provided me with profound support so that I could finish my studies. All this would not have been possible without their support and encouragement.

Table of Contents

Abstract.....	II
Declaration of Authenticity.....	V
Acknowledgements	VI
Table of Contents	VIII
List of Figures.....	XI
List of Tables.....	XVI
List of Symbols	XVII
Chapter 1 : Introduction.....	1
1.1 Junction Fires.....	2
1.2 Problem and Motivation	2
1.3 Addressing the Research Gap	4
Chapter 2 : Literature Review.....	7
2.1 Wildfire Modelling Objectives	7
2.2 Wildfire Modelling Approaches.....	9
2.2.1 Physics-Based Models	12
2.2.2 Coupled Fire–Atmosphere Models	12
2.3 Environmental Factors	13
2.3.1 Wind Speed	14
2.3.2 Slope	16
2.4 Fire Regimes.....	17
2.5 Relevant Previous Studies	19
2.6 Research Gap.....	22
Chapter 3 : The Mathematical and Numerical Model	23
3.1 Introduction	23
3.2 Mathematical Model.....	24

3.2.1 Solid-Fuel Model	25
3.2.2 Gas-Fuel Model	30
3.2.3 Turbulence Modelling: Large Eddy Simulation Approach	35
3.2.4 Combustion Modelling	36
3.2.5 Radiation Heat Transfer.....	40
3.3 Numerical Method	42
3.3.1 Fluid Phase and Solid-Phase Meshes	42
3.3.2 Solving Procedure and Solver Performance	44
3.3.3 Time Scheme Transport Equations	46
3.3.4 Convection Scheme.....	48
Chapter 4 : Junction Fire Configuration Setup	50
4.1 Physical Problem	50
4.2 Experiments Against which Model Validation was Conducted	51
4.3 Shrub Junction Fire Numerical Configuration.....	54
Chapter 5 : Sensitivity Study	61
5.1 Soot Fraction.....	62
5.2 Convective Heat Transfer Coefficient	66
5.3 Thermal Emissivity.....	69
5.4 Particle Shape.....	70
5.5 Ambient Humidity and Temperature	71
5.5.1 Humidity.....	72
5.5.2 Temperature	72
5.6 Burner Parameters.....	74
5.7 Domain Size and Mesh.....	77
5.8 Fuel Description	78
5.9 Discussion.....	80
Chapter 6 : Validation Study.....	82
6.1 Effect of Slope Angle	84
6.2 Effect of Junction Angle	86

6.3 Effect of Moisture Content.....	87
6.4 Discussion.....	88
Chapter 7 : Parametric Study – Junction Fire without Wind	89
7.1 Configuration Description and Numerical Parameters	89
7.2 Junction Fire Evolution.....	91
7.3 Fire Front and ROS.....	93
7.3.1 Effect of Slope Angle	94
7.3.2 Effect of Junction Angle	97
7.4 Heat Transfer Mode	99
7.5 Heat Release Rate.....	101
Chapter 8 : Parametric Study – Junction Fire with Wind	104
8.1 Configuration Description and Numerical Parameters	104
8.2 Streamlines	105
8.3 Fire Front and ROS.....	108
8.4 Heat Transfer Mode	114
8.5 Heat Release Rate.....	117
Chapter 9 : Conclusion.....	119
9.1 Discussion.....	119
9.2 Conclusion	120
References.....	124
Appendix A : Junction Point Positions and Dynamic ROS	130

List of Figures

Figure 1.1: Flow diagram of the structure of the Masters thesis..... 6

Figure 2.1: Conceptual model describing the controls of fire across spatial and temporal scales [16]: dominant factors that influence fire at the scale of a flame, a single wildfire and a fire regime. This is an extension of the traditional ‘fire triangle’ concept, here including broad scales of space and time, and the feedbacks that fire has on the controls themselves (small loops), as well as feedbacks between processes at different scales (arrows)..... 9

Figure 2.2: Relationship between average wind speed at a height of 10 m and rate of forward spread. The threshold wind speed is the speed at which the fire spreads as a continuously heading fire. Above this speed, the relationship is slightly curvilinear; increase in rate of spread lessens slowly with increasing wind speed [22, 23]. 15

Figure 2.3: The effect of slope on rate of forward spread where 1 represents the relative rate of spread on level ground (the relative rate is referenced to the basic value in the same fuel bed in no-wind and no-slope conditions) [24]..... 16

Figure 2.4: Cartoon showing a sketch of the flame geometries expected from the two fire propagation modes taken from Khan et al. [30]: (a) wind-driven flame, (b) buoyancy-driven flame. L_f and F_h represent the flame length and flame height respectively. 18

Figure 3.1: Structures of the fluid-phase mesh (—) and of the solid-phase mesh (•) in the x-y plane, and staggered locations of the fluid-phase variables (scalar variables ϕ and velocity field components u and v). 44

Figure 3.2: Fluid-phase mesh structure and notations in one direction 49

Figure 4.1: Schematic representation of junction fire on a slope with a single component of wind..... 50

Figure 4.2: Photo of the canyon table DE4 [58]..... 52

Figure 4.3: General view of combustion table DE4 during preparation and tests: (a) reference image before the test. The Pitot tubes can be seen on the left side of the table. At ignition: (b) time $t = 0$ s; (c) $t = 2$ s; (d) $t = 18$ s [9]. 53

Figure 4.4: Infrared frames from a junction fire test. The time between frames is 4 s [9]. 54

Figure 4.5: Perspective view showing the computational domain and the vegetation cover used in a V-shape.	55
Figure 4.6: Solid-phase dry-material density (kg/m^3), charcoal density (kg/m^3) and gas-mixture temperature (K) within vegetation thickness in the midplane of V-shaped vegetation.....	58
Figure 5.1: Junction point position for $\alpha = 20^\circ$, $\theta = 30^\circ$ with two values of soot mass fraction.	63
Figure 5.2: Local soot volume fraction for two value of soot mass fraction (above for 0.05 kg/kg, below for 0.005 kg/kg) in the midplane of the V-shape at $t - t_{\text{ignition}} = 9$ s for $\alpha = 20^\circ$, $\theta = 30^\circ$	64
Figure 5.3: Total volume flow rate of soot for two values of soot mass fraction in case with $\alpha = 20^\circ$, $\theta = 30^\circ$	65
Figure 5.4: Cross-sectional views of the vegetation layer in the midplane of V-shaped vegetation showing the mass of dry material (α_{sp} in kg/m^3) at different simulation times: (a) and (c) at $t - t_{\text{ignition}} = 9$ s; (b) and (d) at $t - t_{\text{ignition}} = 14$ s, for two values of soot mass fraction: (a) and (b) for $f = 0.005$ kg/kg; (c) and (d) for $f = 0.05$ kg/kg for $\alpha = 20^\circ$, $\theta = 30^\circ$	65
Figure 5.5: Junction point position with a fifth of the value of the heat transfer coefficient for $\alpha = 0^\circ$, $\theta = 30^\circ$	68
Figure 5.6: Junction point position with a fifth of heat transfer coefficient value for $\alpha = 20^\circ$, $\theta = 30^\circ$	68
Figure 5.7: Total irradiance (W/m^2) at $t - t_{\text{ignition}} = 15$ s in the midplane of V-shaped vegetation for a horizontal fuel bed ($\alpha = 0^\circ$, $\theta = 30^\circ$) with different convective heat transfer coefficients.	69
Figure 5.8: Junction point position for two vegetation emissivity values for the case $\alpha = 0^\circ, \theta = 30^\circ$	70
Figure 5.9: Junction point position for the case $\alpha = 20^\circ$, $\theta = 30^\circ$	71
Figure 5.10: Junction point position for the four combinations of ambient temperature and humidity ratio.	73
Figure 5.11: Junction point position in four simulations testing burner parameters (width and injection velocity) for $\alpha = 20^\circ$, $\theta = 30^\circ$	76
Figure 5.12: Junction point position in three simulations testing burner parameters (width and injection velocity) for slope angle $\alpha = 0^\circ$	76

Figure 5.13: Junction point position in four sensitivity tests for $\alpha = 0^\circ$, $\theta = 30^\circ$	78
Figure 5.14: Junction point position for the different fuel combinations	80
Figure 6.1: 3D front view (left) and side view (right) of an isovalue surface of the soot volume fraction (1.6×10^{-7}) coloured by gas temperature and an isovalue surface of the water mass fraction (9×10^{-3}) (in grey with 50% transparency) obtained for simulation S3030-M14, at $t - t_{\text{ignition}} = 10\text{s}$	83
Figure 6.2: Evolution of fire perimeter according to pyrolysis edge (dry material $\alpha_{\text{SPS}} = 0.001 \text{ kg/m}^3$) for S3000-M24. The first perimeter (outer) is at $t - t_{\text{ignition}} = 5 \text{ s}$ and the time difference between each perimeter is 5 s	84
Figure 6.3: Evolution of the value of ROS for three different slope values (α) as a function of time.	85
Figure 6.4: Evolution of the value of ROS for two different junction angles θ as a function of time.	86
Figure 6.5: Evolution of the value of ROS for two different moisture content values (m_f) as a function of time.	87
Figure 7.1: Computational domain and vegetation zone for junction angles 15° and 90°	90
Figure 7.2: Evolution of fire perimeter according to pyrolysis edge (dry material $\alpha_{\text{SPS}} = 0.001 \text{ kg/m}^3$) for cases (a) S1500, (b) S3020, (c) S4500, (d) S6030, and (e) S9040 respectively. The first perimeter (outer) is at $t - t_{\text{ignition}} = 0 \text{ s}$ and the time difference between each perimeter is 5 s (the time corresponding to each perimeter is indicated next to it).	92
Figure 7.3: (a) Junction point position and (b) evolution of ROS as a function of time for four different slope angles for $\theta = 15^\circ$	94
Figure 7.4: (a) Junction point position and (b) evolution of ROS as a function of time for three different slope angles for the case $\theta = 30^\circ$	95
Figure 7.5: (a) Junction point position and (b) evolution of ROS as a function of time for three different slope angles for the case $\theta = 45^\circ$	96
Figure 7.6: (a) Junction point position and (b) evolution of ROS as a function of time for five different slope angles for the case $\theta = 60^\circ$	97
Figure 7.7: (a) Junction point position, and (b) evolution of ROS as a function of time for five different slope angles for the case $\theta = 90^\circ$	97

Figure 7.8: Evolution of ROS for four different junction angles and (a) $\alpha = 0$, (b) 20° and (c) 40° as a function of time..... 98

Figure 7.9: Power density received by the solid fuel by convection from the gas mixture and by radiation, in the case of slope angles 0 and 40° , for the five junction angles (a) 15° , (b) 30° , (c) 45° , (d) 60° , and (e) 90° 100

Figure 7.10: Time evolution of the heat release rate (HRR) of the fire obtained from the rate of total mass loss evaluated for the whole solid-fuel layer with different slope angles for cases simulated with junction angles of (a) 15° , (b) 30° , (c) 45° , (d) 60° , and (e) 90° .
..... 102

Figure 8.1: Temperature fields and streamlines of the gaseous phase obtained numerically at $t - t_{\text{ignition}} = 6$ s in the vertical median plane for junction angle $\theta = 15^\circ$, and (a) $\alpha = 0^\circ$, $U = 0$ m/s; (b) $\alpha = 0^\circ$, $U = 4$ m/s; (c) $\alpha = 40^\circ$, $U = 0$ m/s; and (d) $\alpha = 40^\circ$, $U = 4$ m/s. 106

Figure 8.2: Temperature fields and streamlines of the gaseous phase obtained numerically at $t - t_{\text{ignition}} = 15$ s in the vertical median plane for junction angle $\theta = 60^\circ$, and (a) $\alpha = 0^\circ$, $U = 0$ m/s; (b) $\alpha = 0^\circ$, $U = 4$ m/s; (c) $\alpha = 40^\circ$, $U = 0$ m/s; and (d) $\alpha = 40^\circ$, $U = 4$ m/s. 107

Figure 8.3: Junction point position (left-hand column) and evolution of ROS (right-hand column) as a function of time for three different slope angles for $\theta = 15^\circ$ 109

Figure 8.4: Junction point position (left-hand column) and evolution of ROS (right-hand column) as a function of time for three different slope angles for $\theta = 30^\circ$ 110

Figure 8.5: Junction point position (left-hand column) and evolution of ROS (right-hand column) as a function of time for three different slope angles for $\theta = 60^\circ$ 111

Figure 8.6: Junction point position (left-hand column) and evolution of ROS (right-hand column) as a function of time for three different slope angles for $\theta = 90^\circ$ 112

Figure 8.7: Evolution of the nominal ROS for three slope angles: 0° (red), 20° (green), and 40° (blue), showing the effect of wind and junction angle ($\theta = 15^\circ$, \blacktriangledown ; $\theta = 30^\circ$, \blacksquare ; $\theta = 60^\circ$, \blacktriangle ; and $\theta = 90^\circ$ \blacklozenge)..... 114

Figure 8.8: Power density received by the solid fuel by convection and radiation for two wind speeds (0 and 4 m/s) in cases: (a) S1500, (b) S1540, (c) S3000, (d) S3040, (e) S6000, (f) S6040, (g) S9000, and (h) S9040..... 116

Figure 8.9: Time evolution of the heat release rate (HRR) obtained from the rate of total mass-loss evaluated for the whole solid-fuel layer with two slope angles (0 and 40°) in

cases simulated with junction angles (a) 15°, (b) 30°, (c) 60°, and (d) 90° without wind and with wind speed $U = 4$ m/s. 118

List of Tables

Table 3.1: Summary of main characteristics of four fully physical fire models. (1) Work in progress. (2) The radiation heat transfer was increased empirically. (3) Pyrolysis and combustion take place at the same location without transport into the gaseous phase. (4) With the limitation introduced by the 2D assumption	24
Table 4.1: Geometric and physical properties of the shrubland vegetation [9, 60].	57
Table 5.1: Parameters tested in the sensitivity analysis	61
Table 5.2: Values of ambient temperature and humidity ratio used in the sensitivity study.	73
Table 5.3: Set of values for burner width and CO injection velocity used in the sensitivity study.....	75
Table 5.4: Mesh parameters for the mesh sensitivity test (for a computational domain size of $29 \times 29 \times 12 \text{ m}^3$).....	77
Table 5.5: Domain size for the sensitivity tests	77
Table 5.6: Geometric and physical properties of leaves and twigs of shrub vegetation.	79
Table 6.1: Physical parameters of the junction fires cases considered in the validation study.....	82
Table 6.2: Maximum ROS values deduced numerically.....	85
Table 7.1: Cases simulated in the parametric study.....	90
Table 7.2: Maximum value of heat release rate (HRR) for different junction angles. ..	101
Table 8.1: Wind speeds (m/s) used in parametric study for different angles of slope (α) and junction fire (θ).....	104

List of Symbols

a_L	Leaf area density
C_D	Drag coefficient of solid particles
C_S	Heat capacity of solid particles
C_p	The specific heat of the ambient temperature
C_{PW}, C_{EW}	Turbulence model constants
D	Diameter of cylindrical solid particles
d_{soot}	Carbon spheres diameter
E_{char}, E_{CO}	Charcoal and CO activation energy in Arrhenius law
F_{Di}	Drag force in direction i resulting from solid particles
Fr	Froude number
F_h	Flame height
f_v	Volume fraction of soot in the gas mixture
f	Mass fraction of soot in the gas mixture
g	Acceleration due to gravity
g_i	Gravity acceleration in direction i
h, h_α	Enthalpy of gas mixture and enthalpy of chemical species α
h_s	Heat transfer coefficient between gas mixture and solid particles

$\Delta h_{Char}, \Delta h_{Pyr}, \Delta h_{Vap}$	Charcoal combustion heat, pyrolysis heat, and water vaporisation heat
I	Radiation intensity
I_f	The fire line intensity
J	Total irradiance
k	Turbulent kinetic energy
K_{char}, K_{CO}	Charcoal and CO frequency factor in Arrhenius law
L	Solid particle length
L_f	Flame length
L_{SGS}	Subgrid scale cut-off width
m	Vegetation family
m_b, m_{b0}	Mass of dry material available above the burner area and initially available above the burner area
m_f	Vegetation moisture content
\dot{M}_α	Mass rate of production of chemical species α resulting from vegetation decomposition
Nc	Byram's convective number
Nu	Nusselt number of solid particles
Nu_{FC}	Forced convection Nusselt number

Nu_{NC}	Natural convection Nusselt number
P, P_α	Pressure of gas mixture and partial pressure of chemical species α in the mixture
P_f, P_w	Buoyancy and inertial force of the wind
P_{th}, P_{hs}	Thermodynamic and hydrostatic pressures of the gas mixture
P_t	Turbulence production term
Pr_{SGS}	Sub-grid Prandtl number
$\dot{Q}_S, \dot{Q}_{S,Char}, \dot{Q}_{S,Conv}$	Rate of heat transferred to the solid particles: total, from solid-fuel combustion, and by convection
Q_{conv}, Q_{rad}	Convective and radiative heat transfer energy
R_0, R_α	Universal ideal gas constant and specific gas constant of chemical species α
Re_T	Turbulent Reynolds number
RH	Ambient humidity ratio
ROS	Rate of spread of the junction point
t	Time
T, T_S, T_a	Temperature of gas mixture, solid particles, and ambient temperature
T_0	Temperature of the ambient air

T_{adiab}	Adiabatic flame temperature
U	Wind speed
u_i	Velocity vector component in direction i
x_i	Cartesian coordinate in direction i
Y	Transverse width of fuelbed
Y_α	Mass fraction of chemical species α in the gas mixture
$Y_{Ash}, Y_{Char}, Y_{Dry}, Y_{H2O}$	Mass fraction of ash, charcoal, dry material, and water in solid particles
W	Width of rectangular cross section of solid particles
V_{inj}	CO injection velocity in the burner
X_α	Mole fraction of chemical species α
<i>Greek Letters</i>	
α	Slope angle or Chemical species
α_G, α_S	Volume fraction of gaseous phase and of solid phase
α_{SG}	Fraction of combustion heat absorbed by solid particles
α_T	Inverse of turbulent Prandtl number
α_ϕ	Inverse of Schmidt number
δ	Fuel bed height
ε	Dissipation rate of turbulent kinetic energy

φ	Multiplying factor for $v_{O_2}^S$ dependent on molar ratio of CO to CO ₂ gases produced from charcoal combustion
$\bar{\phi}, \tilde{\phi}, \phi'$	Reynolds average, Favre average, and fluctuation of a generic field variable ϕ
λ	Thermal conductivity of the gas mixture
μ, μ_T, μ_e	Dynamic viscosity, turbulent viscosity, and effective viscosity of the gas mixture
θ	Junction angle
τ_{mix}	Turbulence mixing time
τ_η	Kolmogorov time scale
$v_{Char}, v_{Soot}, v_{CO_2}, v_{Ash}$	Mass fraction of charcoal, soot, CO ₂ gas, and ash resulting from the pyrolysis of dry material
$\nu_{O_2}^S, \nu_{O_2}^G, \nu_{O_2}^{Soot}$	Mass stoichiometric coefficient of charcoal, CO, and soot combustion
$\dot{\omega}_{Char}, \dot{\omega}_{Pyr}, \dot{\omega}_{Vap}$	Rate of charcoal combustion, of dry material pyrolysis, and of water vaporisation in solid particles
$\rho, \rho_{Dry}, \rho_G, \rho_S, \rho_{Soot}, \rho_S^e$	Density of the gaseous phase, of dry material, of the gas mixture, of the solid phase, of soot, and of solid-fuel elements
σ	Stephan–Boltzmann constant
σ_S	Surface area-to-volume ratio of solid particles

σ_G

Absorption coefficient of the gas/soot mixture

$\dot{\omega}_\alpha$

Rate of production of chemical species α resulting from reaction in the gaseous phase

Chapter 1 : Introduction

Forest fires are a common phenomenon in many parts of the world, sometimes as a result of natural causes, but often as a result of human activities. Several factors contribute potentially to increasing fire hazards in many regions worldwide, like global warming, extensive urbanisation, or reduction of agricultural activities. To reduce this natural hazard, we need a better understanding of wildfire behaviour, the physical mechanisms governing the heat exchange between the fire front and the vegetation layer located ahead, and all the factors contributing to the global behaviour of a fire. In this context, and as in many other fields of science, new physics-based simulation tools have been developed in order to gain more insights into the underlying physics; these simulations appear to be a promising approach [1]. The tools are designed to forecast fire behaviour and the course of a fire front over landscapes on a broad scale, while describing the intricacies of the interaction between flames and possible targets on a smaller scale (houses, vegetation, etc.). FIRESTAR3D is one such three-dimensional model, developed in close collaboration between Aix-Marseille University, the Lebanese University, and Toulon University. FIRESTAR3D is based on a multi-phase formulation and solves the conservation equations of the coupled system formed by the vegetation and the surrounding gaseous medium. The model takes into account the vegetation degradation processes (drying, pyrolysis and combustion), the interaction between the atmospheric boundary layer and vegetation (aerodynamic drag, heat transfer by convection and radiation and mass transfer), and transport in the gaseous phase (convection, turbulence and combustion). The predictive potential of the FIRESTAR3D model was tested at a

large scale in grassland [2] and at a small scale for litter fires (fire propagation through a homogeneous fuel bed in a wind tunnel [3]) and rigorously validated against laboratory-scale experiments.

1.1 Junction Fires

The interaction of two fire fronts is known as a junction fire. The interaction of contiguous fire lines is a form of strong and dynamic fire phenomena characterised by unpredictable behaviour and a relatively high speed of propagation. As with any sort of wildfire, a junction fire's constituents are weather, topography and fuel.

The merging of two fire fronts is considered among the strongest forms of extreme fire behaviour [4]. The rate of spread (ROS) that can be reached when two contiguous fire fronts merge (also known as zippering effect) is at least tenfold the rate of a single line [4]. A junction fire, also called a jump or eruptive fire, is the case when two fire fronts merge, increasing their propagation speed through the strong interaction that occurs between the two fire lines. High-level impacts and fatalities are very often associated with short-lived fire behaviour events characterised by very high rates of spread and fire line intensity, rapid heat release rates and erratic propagation through all available fuel layers [5, 6]. Junction fire is recognised as a typical example of such a phenomenon.

1.2 Problem and Motivation

One example, in particular, motivated researchers to study junction fires: the fire that occurred in the vicinity of Canberra on 18 January 2003 when the MacIntyre's hut and Bendora fires merged in the early afternoon near Pierces Creek [7]. According to testimonies and ground evidence [7], the fire spread associated with these merging fires

was very fast and a tornado formed ahead of the advancing fire front in the space between the two main fires. The fires merging led to a devastating intense fire that spawned the first reported pyrogenic tornado [8]. In the case of the Canberra 2003 fires, the problem was compounded by the presence of non-flat terrain, non-uniform vegetation cover, very strong wind and the influence of other very intense fires.

There has been limited research into the interactions of junction fires, especially using a physics-based model. The physical problem associated with junction fire has been studied experimentally at laboratory and field scales [9, 4, 10, 11, 12], and numerically using a coupled fire-atmosphere semi-empirical model [13]. The findings gave interesting insights into the associated phenomena, despite major limitations. It is desirable to make an endeavour to replicate the behaviour with a physics-based model and examine the influence of some critical parameters.

Physics-based modelling is a very complex approach. The complexity comes from the numerous thermo-physical and numerical parameters used in the simulations. In order to use computational fluid dynamics (CFD) models for fire simulations, it must be ensured that the software is capable of modelling real-world fire, which is confirmed with a sensitivity analysis followed by a validation investigation. The sensitivity of the simulations to the numerical parameters (size of the computational domain, mesh size, burner parameters) must be investigated to ensure the validity of results and efficacy of the simulation and to cope with instability problems. Nevertheless, a limited sensitivity study of some atmospheric and thermo-physical parameters was carried out in the present study to assess their role in numerical modelling. Within the limited scope of this Masters

study, how junction fire behaviour changes with the variation of some weather and topographical features was investigated at a laboratory scale.

1.3 Addressing the Research Gap

To address the research gap in modelling the behaviour of junction fires (discussed in section 2.6), this study aims to quantify the behaviour of junction fires with variation in the slope of the terrain, the speed of the driving wind and the junction angle. The slope of the terrain is the primary topographical parameter and the speed of the driving wind is the primary atmospheric parameter. The junction angle is a characteristic parameter for junction fire, and highly influences the pattern of propagation and affects fire behaviour. FIRESTAR3D is used for physics-based modelling. This study using a physics-based model aims to expand previous research work by taking advantage of such models and trying to develop an understanding of this phenomenon.

The simulation of extreme fire behaviour is complicated and simulation can be conducted effectively using physics-based models for many practical and research purposes. The particular feature of such models is their ability to replicate the phenomenon using pertinent physical laws without considering any specific phenomenological description or observation. This particular advantage makes physics-based modelling the best approach as it is not based on the assumptions of steady ROS. We aimed to investigate the dynamic behaviour resulting from the merging of two fire lines (a junction fire) and study the mechanisms underlying this behaviour. We critically examined the three parameters that can lead to more useful operational models by functioning as a proxy for some of the processes underlying dynamic fire behaviour.

In order to make the problem more amenable to analysis, we decided to study it in steps, starting with the model validation of simple cases of a junction fire in the absence of wind in order to justify the numerical outcomes. A sensitivity analysis to numerical parameters was carried out with a twofold objective: to assess the suitability of the numerical implementation of the junction fire configuration, and to determine the most appropriate grid resolution to be used within the vegetation, as well as the acceptable size of the computational domain. Then, we conducted a thorough parametric study in order to try to describe clearly some of the relevant processes that had previously been observed. The parametric study aimed to capture the approximate range of the ROS values, the primary factors determining the spread and how the parameters interact so that the information can be used to improve understanding of the junction fire phenomenon, in this way identifying the aspects of the phenomenon.

The structure of this Masters thesis is illustrated and described in Figure 1.1.

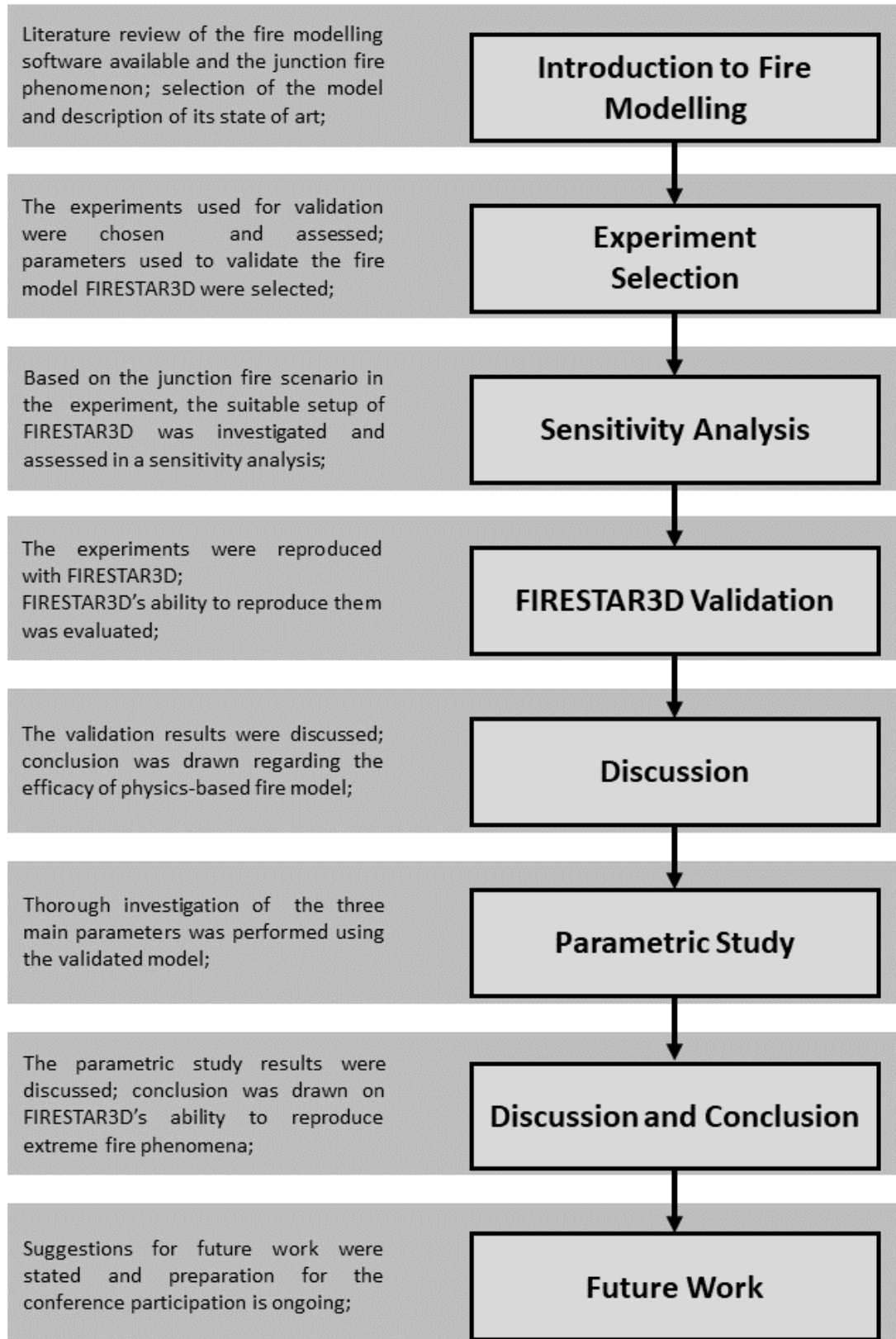


Figure 1.1: Flow diagram of the structure of the Masters thesis.

Chapter 2 : Literature Review

2.1 Wildfire Modelling Objectives

Wildfire modelling deals with the numerical simulation of wildland fires in order to understand and predict their behaviour. Wildfire modelling attempts to reproduce fire behaviour and estimate fire spread characteristics, such as how quickly the fire spreads, in which direction, how much heat it generates and what factors contribute and affect the propagation. A key input to behaviour modelling is the type of fuel (fuel strata) through which the fire is burning. Behaviour modelling can also include whether the fire transitions from the surface (surface fire) to tree crowns (crown fire), as well as extreme fire behaviour including rapid ROS, fire whirls and tall, well-developed convection columns. Fire modelling also attempts to estimate fire effects, such as the ecological and hydrological effects of the fire, fuel consumption, tree mortality, and amount and rate of smoke produced.

Wildfire modelling can fundamentally support suppression operations, the safety of firefighters and citizens, the mitigation of damage and the reduction of risk. For instance, before a fire, modelling helps evaluate risk factors and helps firefighters to determine areas with high risk and develop better infrastructure. Likewise, during fires, modelling is used for planning firefighting strategies, which helps fire crews position equipment on the ground near the burnt zone; therefore, they can minimise damage and stay safe. By conducting fire modelling, one can endeavour to predict a fire's ecological and hydrological consequences, as well as its fuel consumption, tree mortality, and the amount and rate of smoke generated. Modelling also aids in protecting air quality,

ecosystems and watersheds. In prescribed burning, modelling helps in setting planned fires to reduce hazardous fuel loads near developed areas, managing landscapes and restoring natural woodlands. It helps in reducing risk of potential exposure to fire to have better spacing and placement of both permanent and temporary buildings and facility siting.

Through modelling, attempts can be made to replicate wildfire behaviour, such as how rapidly it spreads, in which direction and how much heat it generates. The fundamental difficulties involved with modelling wildfire behaviour result from the complexity of the associated phenomena, the quantity and quality of information required to accurately specify the condition of the fuel, topography and atmosphere, and the large disparity in scales at which these phenomena occur. Fuel elements in a wildfire can be at 10^{-3} – 10^{-2} m scale, topographical characteristics are generally detailed at scales of 10^1 – 10^3 m, atmospheric processes are described at scales of 10^0 – 10^4 m, and a larger fire's range can reach 10^4 – 10^5 m [14]. These difficulties have prompted researchers to diversify approaches in order to attain the desired results.

Although we have a moderate understanding of what controls fire behaviour and its effects at different scales, much less is known about interactions between these scales and how emergent properties of ecosystems are generated. More realistic models would include additional variation in all of the aspects and scales of event initiation and propagation, as suggested in Figure 2.1. Much fire science focuses on understanding fire behaviour, which is sensitive to weather, fuels and topography. Fire regimes describe the characteristic patterns of wildfires over large spatial and temporal scales, and they are sensitive to changes in climate, vegetation and ignitions [15, 16]. Fundamental fire

elements represented at the smallest scale are treated as definitive elements in physics-based simulations.

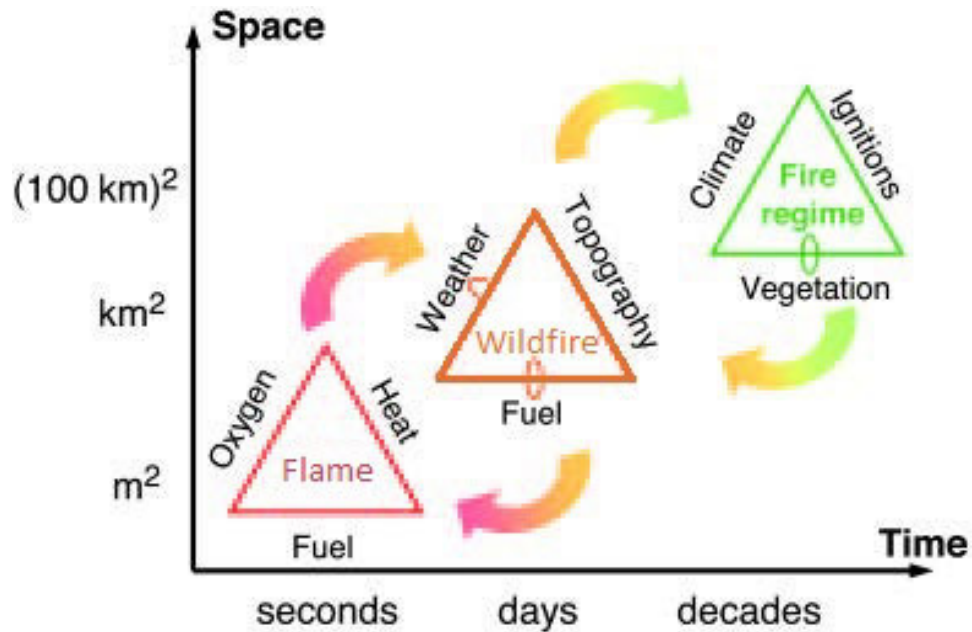


Figure 2.1: Conceptual model describing the controls of fire across spatial and temporal scales [16]: dominant factors that influence fire at the scale of a flame, a single wildfire and a fire regime. This is an extension of the traditional 'fire triangle' concept, here including broad scales of space and time, and the feedbacks that fire has on the controls themselves (small loops), as well as feedbacks between processes at different scales (arrows).

2.2 Wildfire Modelling Approaches

The complexity of the wildfire phenomenon requires conserving a balance between fidelity, availability of data and execution, and this has led to a number of modelling approaches. Sullivan [17] divided these into broad categories: physical¹ and quasi-

¹ one that attempts to represent both the physics and chemistry of fire spread, such as FIRESTAR3D (currently 3Ds)

physical² models; empirical³ and quasi-empirical⁴ models; and simulation⁵ and mathematical analogue⁶ models.

The range of methods that have been used represents a continuous spectrum of possible modelling ranging from the purely physical (those that are based on fundamental understanding of the physics and chemistry involved in the combustion of biomass fuel and behaviour of a wildland fire) to the purely empirical (those that are based on a phenomenological description or statistical regression of observed fire behaviour) [17].

The traditional approach to predicting wildfire spread and flame properties was empirically based on a few parameters like fuel moisture content and the type of fuel. It incorporated the heat from fuel consumption but there was no differentiation of different types of heat transfer such as radiation and convection. These purely empirical models are those that have been based on phenomenological description with no physical understanding at all (and are generally only statistical in nature). A quasi-empirical model is one that uses some form of physical framework on which the statistical modelling is based. Future events can be predicted using such conceptual models derived from experience and intuition from previous fires.

² attempts to represent only the physics (only up to 2D)

³ contains no physical understanding whatsoever (generally only statistical in nature), such as McArthur models

⁴ uses some form of physical framework on which the statistical modelling is based, such as Rothermel model

⁵ implement a pre-existing fire behaviour model (often based on Huygen's wavelet principle) in a landscape spread application and thus address a different set of computation-related problems, such as FARSITE, which includes BEHAVE and Rothermel models

⁶ utilise a mathematical precept (such as Genetic Algorithm, Neural Network) rather than a physical one for modelling the spread of wildland fire

These methods only used simplified mesoscale weather models, excluding the more thorough combustion and heat budget models. Two-dimensional geometry and statistical presumptions were used to simplify the three-dimensional spread, fuel fluctuation, and the precise connection to atmospheric processes.

The most distinguishing attribute of physical models in comparison with empirical models is the presence of combustion chemistry, heat transfer, and fluid dynamics.

Physical fire models numerically solve equations for the fluid dynamics and thermochemistry of fires. They are based on fundamental understanding of the physics and chemistry involved in the combustion of biomass fuel and behaviour of a wildland fire. This category contains those models which differentiate among the modes of heat transfer and attempt to predict the fire spread rate using more fundamental physical and mathematical means. A quasi-physical model attempts to represent only the physics and some chemistry but not the flow (no CFD or feedback upon the atmosphere). However, the semi-physical fire module can be fully coupled to the atmospheric model, while wildland fire processes occur at scales several orders of magnitude smaller than the atmospheric grid size with effective computational consumption.

These tools have diverse dimensions and have been used to understand fire behaviour at different scales. Dynamic fire behaviour cannot be captured using spatial implementations of empirical fire-spread models predicated on the assumption of an equilibrium, or quasi-steady rate of spread. In the present study, a coupled atmosphere–fire physics-based model is used to model the dynamic propagation of junction fires – i.e. when two fire lines merge at an oblique angle.

2.2.1 Physics-Based Models

Physics-based fire spread models based upon conservation laws that use radiation (the dominant heat transfer mechanism) and convection (representing the effect of wind and slope) lead to reaction-diffusion systems of partial differential equations and join computational fluid dynamics models with a wildland fire component, allowing the fire to feed back on the atmosphere. These models include Los Alamos National Laboratory's FIRETEC [18], the wildland–urban interface Fire Dynamics Simulator (WFDS) developed in 2007 [19] and FIRESTAR3D [3].

The cost of added physical complexity is a corresponding increase in computational cost, so much so that a full three-dimensional explicit treatment of combustion in wildland fuels by direct numerical simulation (DNS) at scales relevant for atmospheric modelling does not exist and is beyond current supercomputers' ability. These small-scale models create difficulties when interacting with a weather model; the fluid motion models use a computational fluid dynamics (CFD) model confined in a box much smaller than a typical wildfire [20].

2.2.2 Coupled Fire–Atmosphere Models

Another class of wildfire models are the coupled atmosphere–fire models. Such models couple a physics-based model of the atmosphere with a fire-spread model that is usually (quasi-)empirical, and employ interface tracking methods to model the evolving fire front. Wind is one of the principal atmospheric conditions provided to the fire-spread component, which in turn supplies heat and moisture fluxes to the atmospheric model. Such coupled models have a significant computational advantage over fully physics-based models because physical phenomena are explicitly modelled only down to scales

of the order of hundreds or perhaps tens of metres; smaller-scale atmospheric processes and fire-spread phenomena are parameterised [14]. Coupled fire–atmosphere models also have a conceptual (involving wider phenomena) advantage over uncoupled models because of the feedback from the fire-spread model to the atmospheric component; they have the potential to capture the pyro-convective atmosphere–fire interactions that appear to be the source of much dynamic fire behaviour and of many of the emergent features of fire spread, such as fire line geometry [21]. Despite their advantages, coupled fire–atmosphere models are still computationally expensive and it is only recently that they have evolved to a form that may be suitable for operational use.

The fire-atmosphere interaction includes how the fire and its plume react to the prevailing winds as well as how the atmosphere reacts to the fire's buoyant plume. In addition, the interaction between the fire and the atmosphere can change the direction and geometry of the fire plume, affecting the distribution and intensity of the net heat flow to the solid fuel and the downwind transport of firebrands and smoke. The interaction of the fire plume with the atmosphere can lead to macroscopic (on the scale of the fire front) atmospheric phenomena such as pyrocumulus generation at broader geographical and temporal scales. On even grander scales, the behaviour of the fire and its smoke plume may be influenced by diurnal cycles in temperature and humidity as well as synoptic weather patterns [19].

2.3 Environmental Factors

It is crucial to understand how a wildfire behaves in order to control and manage it. A variety of factors can influence how a wildfire burns, how quickly it spreads and how

difficult it is to suppress. Weather, topography and fuels are the three sides of the main fire behaviour triangle represented in Figure 2.1.

Wind, cloudiness, temperature, moisture and air pressure are all factors in the weather. Low humidity and high temperatures lead plants to dry out, causing flames to spread quickly. Wind not only propels flames over terrain but also provides oxygen for combustion, allowing flames to spread quickly. In addition, the wind can carry embers for kilometres, starting fresh spot fires. Storms can cause fire activity to increase or become entirely unpredictable, while rain and high humidity can suppress or extinguish flames. The physical characteristics of a place, such as slope and aspect (the direction it faces), are referred to as the topography. Vegetation is the source of energy; its thermo-physical properties and flammability have a significant impact on the behaviour of wildfires. For dynamic contiguous fire fronts, the intersection angle is a crucial parameter: it affects the behaviour and the degree of interaction between fire lines. Wind and slope effects are discussed hereafter.

FIRESTAR3D includes the interaction of wildfire with the surrounding atmosphere by means of changing the fire environment via humidity, temperature, and wind speed and direction and wildfire can impact the atmosphere directly via its heat and moisture fluxes or smoke.

2.3.1 Wind Speed

The greatest dynamic factor affecting how fire behaves is wind. Wind speed varies with height above the ground and experiences large short-term fluctuations. It is crucial to indicate the height at which wind is recorded and the length of measurement when relating

wind speed to fire spread [22]. The wind delivers oxygen to the fire in a much greater proportion than would normally be available without wind and moves smoke more quickly, accelerating the spread of the fire.

The following findings are adopted from Cheney et al. [23]. The relationship between wind speed and the rate of forward spread of heading fires is shown in Figure 2.2.

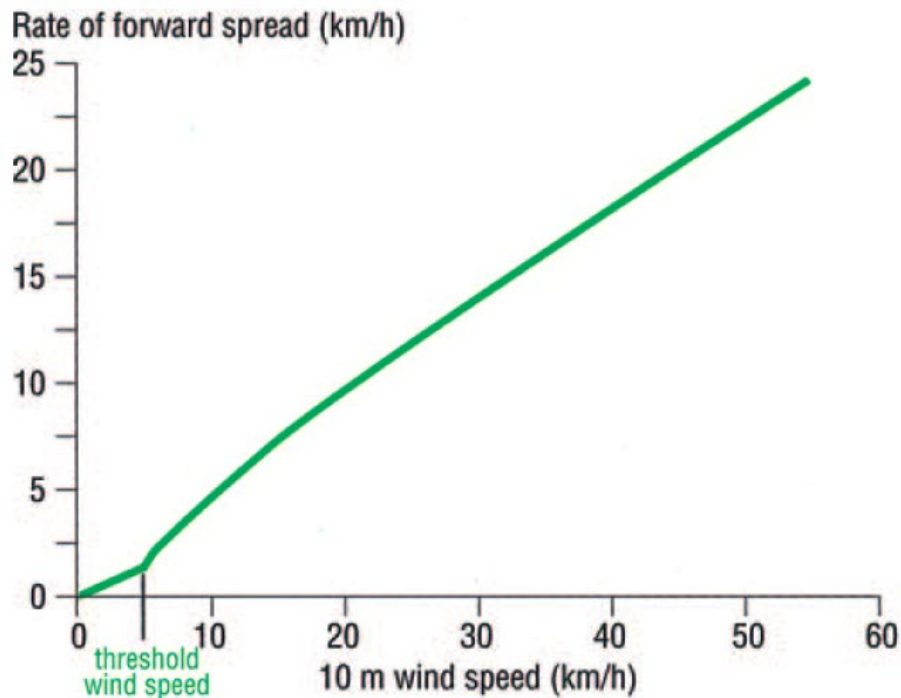


Figure 2.2: Relationship between average wind speed at a height of 10 m and rate of forward spread. The threshold wind speed is the speed at which the fire spreads as a continuously heading fire. Above this speed, the relationship is slightly curvilinear; increase in rate of spread lessens slowly with increasing wind speed [22, 23].

Below a threshold value (around 5 km/h), a linear function between the wind speed and the ROS is proposed; beyond that the function is curvilinear. However, it is still not completely understood how ROS changes with wind speed for complex fire phenomena like junction fires.

2.3.2 Slope

The slope of the terrain can have a significant impact on wildland fire behaviour. One can see this impact on any fire burning in a hilly area. As shown in Figure 2.3, a fire burning up a slope of 10° may burn two times faster than a similar fire on level ground according to McArthur's slope correction [24], and fire propagation speed is double when compared between a 10° and a 20° slope. However, Fayad [25] showed that fire propagation speed on a slope of 20° is not the double of fire on 10° sloped terrain. Rather, Fayad found that the increase was only 55%. For higher slopes (up to 30° upslope), ROS becomes less affected by the upslope (increasing but less than double). Note that this correction is based on laboratory experiments and under no-wind conditions.

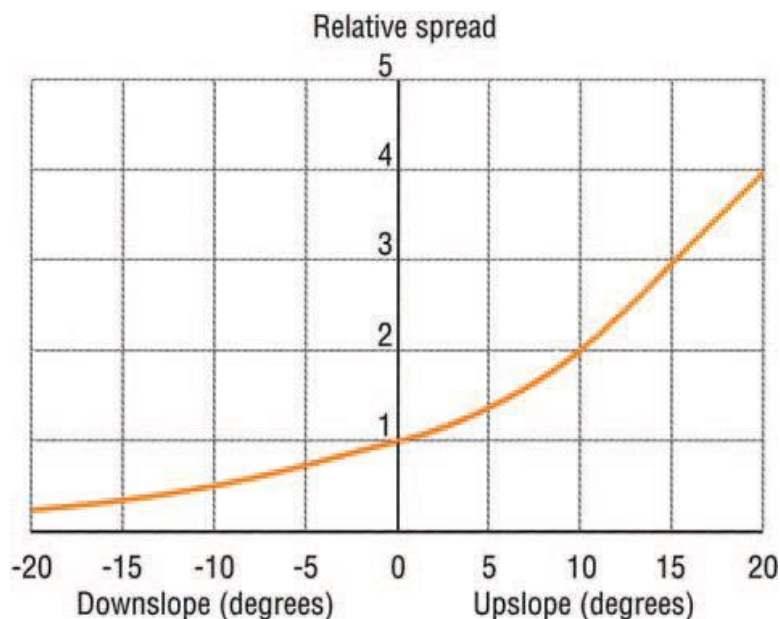


Figure 2.3: The effect of slope on rate of forward spread where 1 represents the relative rate of spread on level ground (the relative rate is referenced to the basic value in the same fuel bed in no-wind and no-slope conditions) [24]

There is less certainty about the values of the multipliers when fires are travelling downslope. If there is streamwise flow and the wind is blowing parallel to the downslope

surface, the ROS may be similar to spread on level ground. The direction of the prevailing wind is the dominant factor determining the direction of a fire, and strong wind will drive a fire across steep slopes [26, 22].

Fayad [25] conducted simulations with not aligned junction symmetry axis and slope direction. The junction point propagation direction shifted toward one of the fire lines and its ROS decreased as of the effect of flow perturbation due to the rotation and decrease of interaction between fire lines.

2.4 Fire Regimes

The key points in understanding the behaviour of wildland fires concern the action of the two forces on the flame and the plume, i.e. buoyancy due to the difference of temperature between the plume and the ambient air acting vertically (P_f), and inertia due to the wind acting horizontally (P_w). Hence, the trajectory and the angle of the flame affect the dominant heat transfer mechanism between the flame and vegetation.

These two forces impact the flame trajectory along different directions (horizontally for wind and vertically for buoyancy); hence, they are in competition. The magnitude of their ratio can be express by Byram's convective number, N_c , defined as the ratio between the power developed by these two forces [27]:

$$N_c = \frac{P_f}{P_w} = \frac{2gI_f}{\rho C_p T_0 (U - ROS)^3} \quad (2.1)$$

where g represents the acceleration due to gravity; I_f and ROS the fireline intensity and rate of spread of the fire; U the wind speed (generally defined as the 10-m open wind

velocity in a zone not affected by the fire front); and ρ , C_p , T_0 the density, the specific heat and the temperature of the ambient air.

In the wind-driven mode, the updraft from the fire plume (buoyant flow) is of less importance than the wind flow. The flame is inclined towards the ground and confined to a boundary layer structure, as shown in Figure 2.4(a). In this mode, a significant convective heat flow downwind of the fire front is anticipated since the fire plume is confined to a boundary layer. As seen in Figure 2.4(b), the flame rises more vertically in the buoyancy-driven mode, where the updraft from the plume overcomes the shearing forces of the driving wind. As a result, it is expected that a large radiative flux will be seen downstream of the fire front. Nelson et al. [28] proposed some criteria based on Byram's convective number: >10 for buoyancy-driven mode and <2 for wind-driven mode. At intermediate N_c values, the fire is neither buoyancy-driven nor wind-driven.

Pagni and Peterson [29] introduced a dimensional analysis using the Froude number, F_r :

$$F_r = \frac{U}{(g L_f)^{\frac{1}{2}}} \quad (2.2)$$

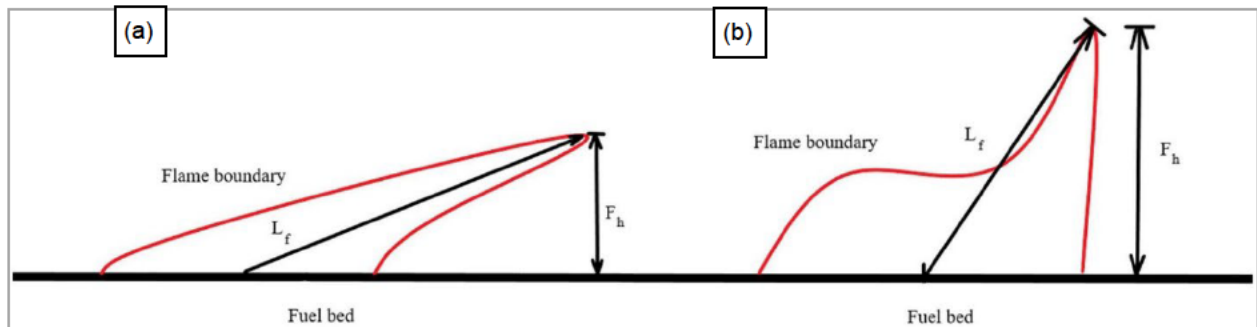


Figure 2.4: Cartoon showing a sketch of the flame geometries expected from the two fire propagation modes taken from Khan et al. [30]: (a) wind-driven flame, (b) buoyancy-driven flame. L_f and F_h represent the flame length and flame height respectively.

where L_f is the flame length. It represents the ratio between these two forces, where above a critical value (nearly equal to 0.5), the heat transfer between the flame and the vegetation is dominated by convection, whereas for smaller values of this parameter, radiation is the dominant mode of heat transfer [29].

2.5 Relevant Previous Studies

Junction fires have been studied experimentally, typically at the laboratory scale [9, 4, 10, 11]. Field experiments were conducted by Raposo et al. [9] and Filkov et al. [12]. In laboratory and field experiments, researchers investigated the relevant parameters' effects by changing the angle between two fire fronts [9, 4, 12], the slope of the fuel bed [9, 10], the fuel type [9, 10] and the wind conditions [11, 12]. Viegas et al. [4, 10] and Raposo et al. [9] demonstrated that there are two phases to the evolution of a junction fire: an acceleration phase at the commencement of the fire where the junction point's speed increases, and a deceleration phase at which the junction point propagation slows and the fire extinguishes.

The first research work on junction fires was conducted by Viegas et al. [4]; the extremely large values of junction point propagation speed or ROS that were found triggered the interest in this phenomenon. The study was limited to the junction angles 10°, 20°, 30° and 45° with a single type of fuel (dead needles of *Pinus pinaster*) and a horizontal fuel bed; this provided the first insights into this phenomenon. The discernible acceleration phase in such conditions followed by a subsequent deceleration phase appeared similar to counter-eruptive fire behaviour. Note that eruptive fire is accelerating all the time, while in counter-eruptive fire, the acceleration is followed by a deceleration phase [4].

The research was extended to encompass the effect of slope angle and fuel bed vegetation [10]. The maximum values of ROS that were reached were possibly the highest values that have been measured in laboratory experiments for corresponding fuel bed and slope test conditions. However, ROS evolution and distance to maximum propagation speed do not vary much as the fuel bed properties change.

Thomas et al. [13] conducted some field-scale numerical simulations of junction fire using a coupled fire–atmosphere model, taking advantage of the inclusion of atmospheric dynamics, fire progression and fire–atmosphere interactions using WRF-FIRE [31]. The simulations reproduced all qualitative features, although no quantitative agreement was found with experiments. The discrepancies were attributed to the differences in scale between the experiments and simulations. The relationship between the dynamic behaviour of junction fire and the fire convective flow induced by the geometry of the fire lines was investigated using the modelled pyro-convective processes in WRF-FIRE. The mechanism for rapid fire spread includes the formation of counter-rotating pairs of vertical vortices lying on or ahead of the fire line. There is clearly a relationship between fire line geometry and ROS in the WRF-FIRE model output; however, a relationship between local fire line curvature and instantaneous local ROS was not found.

The underlying empirical models of fire spread used by Thomas et al. [13] may contribute to some of the discrepancies observed. Scale is also likely an issue, as larger-scale fires seem to exhibit greater instabilities than observed in smaller-scale experiments and simulations. Additionally, the absence of the radiation component in WRF-FIRE is also grounds for arguable findings.

Raposo et al. [9] demonstrated that there are two phases to the evolution of a junction fire: an acceleration phase at the beginning of the fire and a deceleration phase at which the junction point propagation speed decreases and the fire extinguishes. These phases change with slope angle. The scale of the fire and type of vegetation do not have any effect on the fire behaviour. Radiation was found to be the primary mechanism only during deceleration.

Sullivan et al. [11] conducted small-scale experiments (maximum fire line length 1.5 m) including wind as a variable within a wind tunnel. The fire moved forwards into the V shape, with weak short-lived interactions between fronts in the no-wind cases. The asymmetry in the pattern of spread of the fires outside the V shape in the no-wind cases suggests that there is enough interaction between the two arms to affect fire spread outside the V shape. However, there was no enhanced ROS over what was expected from geometric considerations. Sullivan found an increase in the ROS for wind-driven conditions, considerably greater than explained by geometry alone. The relatively small fire size and course of propagation, and the fuel load and type (dense eucalyptus litter) were all cited as potential reasons for result discrepancies across various studies.

Filkov et al. [12] conducted field-scale experiments and developed a method to track fire front propagation using emerging technologies for various fire cases including some types of merging fire. They found almost constant propagation with acceleration in the last phase, in contrast to Viegas et al. [4, 10] and Raposo et al. [9]. They assumed that the asymmetry due to inconstant wind direction and speeds could affect the ROS. Igniting multiple fires concurrently might have caused a certain level of interaction between the flames; hence, the propagation of fires could be changed. In terms of propagation

behaviour, the results of the experiments in wind-driven conditions agreed with the results of Sullivan et al. [11].

2.6 Research Gap

Junction fires have been the focus of many researchers. However, most research has been limited to experimental studies. Although many features have been identified in the experimental investigations, further investigation of junction fire needs to be done for a wider range of slope and junction angles. The behaviour for higher junction angles and various wind speeds has still not been sufficiently studied. As experiments can be quite expensive, properly validated physics-based simulation tools can offer an alternative approach to study junction fire behaviour.

There have been many attempts to determine the main heat transfer mode and its relationship with different propagation phases. A correlation between the radiation and the deceleration phase has been found [9]. The heat released during fires and modes of heat transfer can be ideally assessed using simulation tools once junction fire behaviour is correctly replicated using them.

Chapter 3 : The Mathematical and Numerical Model

3.1 Introduction

FIRESTAR3D belongs to a multi-phase class of models that are based on very detailed modelling of the physicochemical phenomena involved in a fire, from the thermal degradation of the vegetation to the development of the turbulent flame inside and above the vegetation layer. This approach solves two sets of governing equations, one for the vegetation and one for the surrounding gas, which are coupled together through additional terms in the balance equations (mass, momentum and energy) governing the physical system. Owing to the complexity of the geometry (fractal in nature), it does not permit an easy description of the interface between the solid and gaseous phases, which is not introduced in the model. The model takes into account the vegetation degradation processes (drying, pyrolysis and combustion), the interaction between the atmospheric boundary layer and vegetation (aerodynamic drag, heat transfer by convection and radiation and mass transfer), and transport in the gaseous phase (convection, turbulence and combustion). The equations are averaged in a representative elementary volume including the two phases. This preliminary operation is responsible for the introduction of additional source terms in the average balance equations (gas production due to pyrolysis, drag force, convection and radiation heat exchange with the solid phase). This kind of model includes a high level of detail in representing a propagating fire front and its use is limited to describing the behaviour of a fire at a relatively local scale, which is compatible with the study of the interaction between a wildfire and a house or a building.

The details of the model have been widely presented in different publications; we invite the reader to consult references [32, 33, 34, 35, 36] for more information.

3.2 Mathematical Model

The mathematical model in FIRESTAR3D consists of two main parts, coupled through interaction terms: the first part is devoted to the evolution of the state of the vegetation subjected to the intense heat flux coming from the flaming zone, and the second part is devoted to the calculation of the turbulent reactive gas flow resulting from the mixture of pyrolysis and combustion products with the ambient air.

FIRESTAR3D includes most of the integrated features of the 2D version; moreover, new features have been added such as the process of charcoal combustion and the evaluation of the heat transfer coefficient between the solid and the gaseous phase. These new features are presented in Table 3.1 in a comparison with all other physics-based models.

*Table 3.1: Summary of main characteristics of four fully physical fire models.
(1) Work in progress. (2) The radiation heat transfer was increased empirically. (3) Pyrolysis and combustion take place at the same location without transport into the gaseous phase. (4) With the limitation introduced by the 2D assumption*

	FIRESTAR2D	FIRESTAR3D	WFDS	FIRETECH	FIREFOAM
Solver	2D-Implicit	3D-Implicit	3D-Explicit	3D-Explicit	3D-Implicit
Low Mach model	Yes	Yes	Yes	No	Yes ⁽¹⁾
Turbulence	TRANS	TRANS/LES	LES	LES	LES
TRI model	Yes	No	Yes ⁽²⁾	Yes ⁽²⁾	No
Combustion model	Yes	Yes	Yes	No ⁽³⁾	Yes
Multi-fuel model	Yes	Yes	Yes	Yes	No
Small scale	Yes	Yes	Yes	No	Yes
Large scale	Yes ⁽⁴⁾	Yes	Yes	Yes	Yes

3.2.1 Solid-Fuel Model

The heterogeneous character of the vegetation is accounted for using two possible shape families of solid fuel particles: cylindrical particles to represent branches, twigs and needles, and discs representing flat leaves. At all steps of the decomposition process, each solid fuel family m (the number of solid fuel families depends on the level of description of the fuel; it is represented using either a single characteristic element, or more by separating different fuel elements like twigs and leaves) is characterised using a set of physical variables:

- Volume fraction of solid fuel in the surrounding gaseous phase: α_s
- Dry material density: ρ_{Dry}
- Moisture content: m_f
- Surface area-to-volume ratio of solid fuel particles: σ_s
- Solid fuel temperature: T_s
- Evolution of the composition of fuel particles in terms of mass fraction of char, water and dry fuel.

Small fuel particles ($\sigma_s > 600 \text{ m}^{-1}$ corresponding to a diameter $D < 6 \text{ mm}$ for cylindrical particles) can contribute actively to dynamic fire, with study showing that 90% of thin fuel particles are consumed in the flaming zone [37]. At a high heating rate, such as the intense heat flux coming from the flaming zone, the results seem to be affected by parameters such as σ_s and m_f more than by the chemical decomposition of fuel particles. The decomposition of each vegetation particle can be summarised in three main steps: dehydration, pyrolysis (in only one step) and surface oxidation. During thermal decomposition, the local composition of the vegetation consists of water, dry material,

char and ash; these components are represented by their mass fractions Y_{H_2O} , Y_{Dry} , Y_{Char} and Y_{Ash} respectively, resulting in a local density ρ_S of the solid fuel, where the solid fuel model consists of decomposing the fuel bed zone into homogeneous solid fuel elements of effective density $\rho_S^e = \alpha_S \rho_S$. It is assumed that the pyrolysis process would be activated only if dehydration was entirely complete, and that surface oxidation would begin only if the pyrolysis process came to an end.

Dehydration phase

In this process, the evapotranspiration process is reduced to simple vaporisation, during which the temperature of the solid fuel element T_S remains constant at 373 K. The rate of heat transfer \dot{Q}_S received by that fuel element from the flaming zone only serves to produce water vapour at the mass rate:

$$\dot{w}_{vap} = \dot{M}_{H_2O} = \frac{\dot{Q}_S}{\Delta h_{vap}} \quad (3.1)$$

where $\Delta h_{vap} = 2.25 \times 10^3$ kJ/kg is the heat of vaporisation. The term $\bar{\omega}_\alpha$ is the rate of production or destruction of the chemical species α resulting from combustion in the gaseous phase detailed in the Combustion Modelling section (Section 3.2.4).

Pyrolysis phase

The gaseous products of the decomposition of dry fuel by pyrolysis are CO, CO₂ and charcoal. The decomposition of 1 kg of dry fuel is assumed to produce a mass fraction $\nu_{Char} = 0.338$ kg of carbon ($\nu_{Soot} = 0.05$ kg and 0.288 kg of charcoal), $\nu_{CO_2} = 0.2$ kg of CO₂ and $\nu_{CO} = 0.462$ kg. The hot fuel pyrolysis products (CO and soot) ignite homogeneously in the gaseous phase by contact with the oxygen contained in the ambient air.

The pyrolysis equation is written for 1 kg of dry fuel:



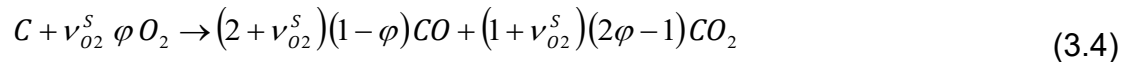
The pyrolysis process is assumed to take place when the solid fuel element T_S is between 400 K and 500 K [35, 38, 39] at the mass rate:

$$\dot{w}_{Pyr} = \frac{\dot{Q}_S}{\Delta h_{Pyr}} \times \frac{T_S - 400}{500 - 400} \quad (3.3)$$

where Δh_{Pyr} is the heat of pyrolysis, which depends on the vegetation species. According to this equation, a portion of the heat received by the fuel element contributes to the pyrolysis process, while the remaining portion continues to increase the solid fuel temperature T_S . Note that T_S cannot exceed 500 K as long as the pyrolysis process has not ended.

Surface oxidation

The provision representing the surface oxidation of charcoal has been modified to account for possible incomplete combustion producing both CO and CO₂ [40]. The balance equation for 1 kg of charcoal is given by:



where $v_{O_2}^S = 8/3$ and $v_{O_2}^S \varphi$ is the mass stoichiometric coefficient, which depends on the molar ratio of CO to CO₂ gases produced from charcoal combustion and is given by:

$$\varphi = \frac{2 + \frac{CO}{CO_2}}{2\frac{CO}{CO_2} + 2} \quad (3.5)$$

The molar ratio of CO to CO₂ gases depends on the surface temperature T_S according to the relationship [40]:

$$\frac{CO}{CO_2} = 2500 \exp\left(-\frac{6240}{T_S}\right) \quad (3.6)$$

At low temperatures, $\varphi \rightarrow 1$ and only CO₂ is produced, while at high temperatures, $\varphi \rightarrow 0.5$ and practically only CO is produced. The reaction rate of charcoal combustion is approximated by the Arrhenius law as follows:

$$\dot{\omega}_{Char} = k_{Char} P_{O_2} \exp\left(-\frac{E_{Char}}{R_0 T_S}\right) \alpha_s \sigma_s \quad (3.7)$$

where P_{O_2} is the partial pressure of O₂ at the solid fuel particle surface. The frequency factors $k_{Char} = 254.2 \text{ kg}/(\text{m}^2 \cdot \text{s} \cdot \text{atm})$ and activation energy $E_{Char}/R_0 = 9000 \text{ K}$ are evaluated experimentally from a thermo-gravimetric analysis (TGA) performed for wood charcoal samples [40].

Heat released during charcoal combustion taking place at the surface of a solid-fuel particle is assumed to be absorbed both by the solid-fuel element and by the gaseous phase. The rate of heat absorption by the solid fuel element is:

$$\dot{Q}_{S,Char} = \alpha_{SG} \Delta h_{Char} \dot{\omega}_{Char} \quad (3.8)$$

where Δh_{Char} is the charcoal combustion heat in Equation (3.4), given by:

$$\Delta h_{char} = (2 + \nu_{O_2}^S)(1 - \varphi) \Delta h_{CO} + (1 + \nu_{O_2}^S)(2\varphi - 1) \Delta h_{CO_2} \quad (3.9)$$

with $\Delta h_{CO} = 9$ MJ/kg and $\Delta h_{CO_2} = 30$ MJ/kg the reaction heats of incomplete and complete combustion of carbon, which can be obtained from Equation (3.4) by setting φ at 0.5 and 1 respectively. We assume in this study that heat released during charcoal combustion is equally shared by the gaseous phase and by the solid fuel element, i.e. $\alpha_{SG} = 0.5$.

The time evolution of the composition and the temperature of a family m of solid-fuel particles in the fuel bed are controlled by the following set of six equations [34, 35, 36]:

$$\frac{d}{dt}(\alpha_S^m \rho_S^m Y_{H_2O}^m) = -\dot{\omega}_{Vap}^m \quad (3.10)$$

$$\frac{d}{dt}(\alpha_S^m \rho_S^m Y_{Dry}^m) = -\dot{\omega}_{Pyr}^m \quad (3.11)$$

$$\frac{d}{dt}(\alpha_S^m \rho_S^m Y_{Char}^m) = (\nu_{Char} - \nu_{Soot}) \dot{\omega}_{Pyr}^m - \left(1 + \frac{\nu_{Ash}}{\nu_{Char}}\right) \dot{\omega}_{Char}^m \quad (3.12)$$

$$\frac{d}{dt}(\alpha_S^m \rho_S^m) = -\dot{\omega}_{Vap}^m - (1 - \nu_{Char} + \nu_{Soot}) \dot{\omega}_{Pyr}^m - \dot{\omega}_{Char}^m \quad (3.13)$$

$$\frac{d}{dt}(\alpha_S^m) = -\frac{1}{\rho_S^m} \dot{\omega}_{Char}^m \quad (3.14)$$

$$\alpha_S^m \rho_S^m C_S^m \frac{dT_S^m}{dt} = \dot{Q}_S^m - \dot{\omega}_{Vap}^m \Delta h_{Vap} - \dot{\omega}_{Pyr}^m \Delta h_{Pyr} + \alpha_{SG} \Delta h_{Char} \dot{\omega}_{Char}^m \quad (3.15)$$

where C_S^m is the heat capacity of the solid fuel element of family m .

The solid fuel element receives heat by convection and radiation; the rate of this heat transfer between the hot gases and the solid fuel element is given by [34, 35, 36]:

$$\dot{Q}_s = h_s \alpha_s \sigma_s (T - T_s) + \frac{\alpha_s \sigma_s}{4} (J - 4\sigma T_s^4) \quad (3.16)$$

- T is the temperature of the gas mixture around the solid fuel element
- $\sigma = 5.67 \times 10^{-8} \text{ W/m}^2 \cdot \text{K}^4$ is the Stephan–Boltzmann constant
- J is the total irradiance calculated by integrating the radiation intensity in all directions defined in the Radiation Heat Transfer section below (Section 3.2.5).
- h_s is the convection heat transfer coefficient, which depends on the shape of the solid fuel particles. It is obtained from correlations. For example, for a cylindrical particle, h_s is obtained from:

$$Nu = \frac{h_s D}{\lambda}; \quad Nu = (Nu_{FC}^2 + Nu_{NC}^2)^{1/2} \quad (3.17)$$

where Nu is the Nusselt number based on the diameter D of a cylindrical solid particle, λ is the thermal conductivity of the gas mixture, and Nu_{FC} and Nu_{NC} are respectively the forced convection and natural convection Nusselt numbers. Nu_{FC} and Nu_{NC} are correlated to the Prandtl number of the gas mixture and to the Reynolds and Rayleigh numbers based on the diameter D of a cylindrical solid particle.

3.2.2 Gas-Fuel Model

The thermal degradation of the vegetation and the combustion reactions cause the gaseous phase state evolution (composition, velocity, temperature...). This evolution is governed by a set of equations of mass, momentum and energy. Since the flow regime is unsteady and fully turbulent in various regions of the computation domain, the equations are filtered using a mass-weighted average formulation [41]. Hence, the filtered

variables are governed by the following set of transport equations solved in the low Mach number approximation [42, 43]:

$$\frac{D\bar{\rho}}{Dt} = \sum_m \sum_{\alpha} \dot{M}_{\alpha}^m \quad (3.18)$$

$$\frac{D(\bar{\rho}\tilde{u}_i)}{Dt} = -\frac{\partial\bar{P}}{\partial x_i} + \frac{\partial}{\partial x_j} \left[\bar{\mu} \left(\frac{\partial\tilde{u}_i}{\partial x_j} + \frac{\partial\tilde{u}_j}{\partial x_i} - \frac{2}{3} \frac{\partial\tilde{u}_l}{\partial x_l} \delta_{ij} \right) \right] - \frac{\partial}{\partial x_j} (\overline{\rho u'_i u'_j}) + (\bar{\rho} - \bar{\rho}_0) g_i - \sum_m F_{Di}^m \quad (3.19)$$

$$\begin{aligned} \frac{D(\bar{\rho}\tilde{h})}{Dt} &= \frac{\partial}{\partial x_j} \left(\frac{\bar{\mu}}{Pr} \frac{\partial\tilde{T}}{\partial x_j} \right) - \frac{\partial}{\partial x_j} (\overline{\rho u'_j h'}) + \frac{d\bar{P}_{th}}{dt} + (1 - \alpha_{SG}) \Delta h_{Char} \sum_m \dot{\omega}_{Char}^m \\ &\quad + \sum_m \sum_{\alpha} \dot{M}_{\alpha}^m \bar{h}_{\alpha}^m - \sum_m \dot{Q}_{S,Conv}^m + \alpha_G \sigma_G (J - 4\sigma\tilde{T}^4) \end{aligned} \quad (3.20)$$

$$\frac{D(\bar{\rho}\tilde{Y}_{\alpha})}{Dt} = \frac{\partial}{\partial x_j} \left(\frac{\bar{\mu}}{Sc} \frac{\partial\tilde{Y}_{\alpha}}{\partial x_j} \right) - \frac{\partial}{\partial x_j} (\overline{\rho u'_j Y'_{\alpha}}) + \bar{\omega}_{\alpha} + \sum_m \dot{M}_{\alpha}^m \quad (3.21)$$

In these equations, all transport variables ϕ (density ρ , velocity components u_i , enthalpy h , and mass fractions Y_{α} of chemical species α : CO, O₂, CO₂, H₂O and N₂) are decomposed as a sum of two contributions (Reynolds average + fluctuation: $\phi = \bar{\phi} + \phi'$).

On the other hand, the Favre average is defined by: $\tilde{\phi} = \overline{\rho\phi}/\bar{\rho}$. The differential operator D/Dt is defined as:

$$\frac{D\phi}{Dt} = \frac{\partial\phi}{\partial t} + \frac{\partial(\tilde{u}_j\phi)}{\partial x_j} \quad (3.22)$$

The gas-phase density $\rho = \alpha_G \rho_G$, where ρ_G is the density of the gas mixture and α_G is the volume fraction of the gas species given by:

$$\alpha_G = 1 - \sum_m \alpha_S^m \quad (3.23)$$

where

- α_S^m is the volume fraction of family m of solid-fuel particles in the fuel bed,
- ρ_0 is the initial gas-phase density that is stratified owing to gravity,
- g_i is the gravity component in the x_i direction.

In the low Mach number approximation [42, 43], acoustic filtering results in the splitting of the gas-mixture pressure into three contributions: the gas dynamic pressure P_G acting to balance inertia and time-varying external forces, the gas thermodynamic pressure P_{thG} , which is spatially homogeneous, and the gas hydrostatic pressure P_{hsG} , which is time-independent and balances the initial density stratification. The gas-phase pressure parts are obtained from:

$$P = \alpha_G P_G, P_{th} = \alpha_G P_{thG}, \text{ and } P_{hs} = \alpha_G P_{hsG}. \quad (3.24)$$

In addition to the previous equations, the gas mixture is assumed to behave as an ideal gas. Hence, in the low Mach number approximation, the gas-phase density is obtained from:

$$\bar{P}_{th} + \bar{P}_{hs} = \bar{\rho} \left(\sum_{\alpha} R_{\alpha} \tilde{Y}_{\alpha} \right) \tilde{T} \quad (3.25)$$

where R_{α} (J/kg.K) is the perfect gas constant of chemical species α . The thermodynamic pressure P_{th} can be updated from the total mass conservation for closed fluid systems, while for open ones, its value is prescribed.

The gaseous phase is assumed also to behave as a Newtonian fluid with a viscosity $\mu = \alpha_G \mu_G$, where μ_G is the dynamic viscosity of the gas mixture obtained from a mass fraction-weighted linear combination of the dynamic viscosities μ_{α} of the chemical species

α . On the other hand, the dependence of μ_α on temperature is governed by Sutherland's law:

$$\bar{\mu}_\alpha = \mu_\alpha^{ref} \left(\frac{\tilde{T}}{T_{ref}} \right)^{1.5} \left(\frac{T_{ref} + S}{\tilde{T} + S} \right) \quad (3.26)$$

where

- $T_{ref} = 273 \text{ K}$
- $S = 110.4 \text{ K}$
- μ_α^{ref} is the dynamic viscosity of the chemical species α at temperature T_{ref}
- the Prandtl and Schmidt numbers are both set to 0.71.

The term F_{Di}^m denotes the i^{th} component of the drag force resulting from the dynamic interaction between the gas flow and the vegetation family m ; it is given by:

$$F_{Di} = \bar{\rho} |\tilde{u}| \tilde{u}_i C_D a_L \quad (3.27)$$

where

- $a_L = \alpha_S \sigma_S / 2$ is the leaf area density (LAD),
- C_D is the drag coefficient obtained from correlations depending on the particle shape of vegetation family m .

The enthalpy h of the gas mixture is obtained from a mass fraction-weighted linear combination of the enthalpies h_α of the chemical species (CO, O₂, CO₂, H₂O and N₂). For each chemical species, the enthalpy temperature dependence is treated using the CHEMKIN thermodynamic data base [44]:

$$\tilde{h}_\alpha = \beta_{\alpha,0} + \sum_{n=1}^5 \frac{1}{n} \beta_{\alpha,n} \tilde{T}^n \quad (3.28)$$

Where β and n are CHEMKIN coefficients.

The term $\dot{Q}_{S,Conv}^m$ is the rate of heat exchange by convection between the gas mixture and the solid fuel particles of vegetation family m ; it is given by Equation (3.16). σ_G is the radiation extinction coefficient of the gas–soot mixture (including absorption due to the presence of CO, CO₂, H₂O and soot particles in the flame and along the plumes [45]).

During the thermal decomposition of each vegetation family m , O₂ gas is consumed, CO, CO₂ and H₂O gases, and charcoal soot particles are produced at the following mass rates:

$$\dot{M}_{O_2} = -v_{O_2}^S \varphi \dot{\omega}_{Char} \quad (3.29)$$

$$\dot{M}_{CO} = (1 - v_{Char} - v_{CO_2}) \dot{\omega}_{Pyr} + (2 + v_{O_2}^S)(1 - \varphi) \dot{\omega}_{Char} \quad (3.30)$$

$$\dot{M}_{CO_2} = v_{CO_2} \dot{\omega}_{Pyr} + (1 + v_{O_2}^S)(2\varphi - 1) \dot{\omega}_{Char} \quad (3.31)$$

$$\dot{M}_{H_2O} = \dot{\omega}_{Vap} \quad (3.32)$$

$$\dot{M}_{Soot} = v_{Soot} \dot{\omega}_{Pyr} \quad (3.33)$$

These rates contribute to the source terms of the conservation equations of mass, energy and chemical species. Finally, $\bar{\omega}_\alpha$ is the rate of production or destruction of the chemical species α resulting from combustion in the gaseous phase detailed in the Combustion Modelling section (Section 3.2.4).

3.2.3 Turbulence Modelling: Large Eddy Simulation Approach

Large eddy simulation (LES) is a mathematical model for turbulence used in computational fluid dynamics. In this section, we provide some theoretical information about the LES approach available in FIRESTAR3D.

The action of fluctuations on the average transport equations is represented by double correlations. These correlations are computed using the eddy viscosity concept [46] and the generalised gradient diffusion of the scalar quantities ϕ as follows:

$$-\overline{\rho u'_i u'_j} = \mu_T \left(\frac{\partial \tilde{u}_i}{\partial x_j} + \frac{\partial \tilde{u}_j}{\partial x_i} \right) - \frac{2}{3} \left(\mu_T \frac{\partial \tilde{u}_l}{\partial x_l} + \bar{\rho} k \right) \delta_{ij} \quad (3.34)$$

$$-\overline{\rho u'_i \phi'} = \mu_T \alpha_\phi \frac{\partial \tilde{\phi}}{\partial x_i} \quad (3.35)$$

The turbulent viscosity μ_T , which is also called sub-grid viscosity, is evaluated from the turbulent kinetic energy k , as

$$\mu_T = \rho C'_{SGS} L_{SGS} \sqrt{k_{SGS}} \quad (3.36)$$

where L_{SGS} is the cut-off width, which is computed from the volume of the computational cell,

$$L_{SGS} = (\Delta X \cdot \Delta Y \cdot \Delta Z)^{1/3} \quad (3.37)$$

The field of the turbulent sub-grid kinetic energy k_{SGS} is calculated from the following transport equation:

$$\frac{D(\bar{\rho} k_{SGS})}{Dt} = \frac{\partial}{\partial x_j} \left(\mu_T \alpha_T \left(\frac{\partial k_{SGS}}{\partial x_j} \right) \right) + P_K + W_K - \bar{\rho} C_\epsilon \frac{k_{SGS}^{3/2}}{L_{SGS}} \quad (3.38)$$

$$+ \frac{1}{2} \bar{\rho} |\bar{u}| \sum_m C_d^m \alpha_S^m \sigma_S^m (C_{Pw} |\bar{u}|^2 - C_{\epsilon w} k_{SGS})$$

From k_{SGS} , one can obtain the dissipation rate, ϵ_{SGS} as follows:

$$\epsilon_{SGS} = C_\epsilon \frac{k_{SGS}^{3/2}}{L_{SGS}} \quad (3.39)$$

In the equations above, the values of the model constants C'_{SGS} and C_ϵ are 0.07 and 0.93 respectively. On the other hand, P_K and W_K are the terms contributing to the production of turbulence, due to shear and buoyancy effects respectively, [46], and are given by

$$P_K = -\overline{\rho u_i' u_j'} \frac{\partial u_i}{\partial u_j} \quad \text{and} \quad W_K = \frac{\mu_T}{\rho} \alpha_T \frac{\partial \bar{\rho}}{\partial x_j} g_j \quad (3.40)$$

The inverse of the effective turbulent Prandtl number α_T as well as α_ϕ in the transport equation of a generic variable ϕ (temperature or chemical species mass fraction) are computed directly from the value of the sub-grid Prandtl number Pr_{SGS} , which is equal to 0.85, as

$$\alpha_\phi = \alpha_T = \frac{1}{Pr_{SGS}} \quad (3.41)$$

The terms including the drag coefficient, C_D , represent the contribution of the drag force to the turbulent kinetic energy balance. They include both production and dissipation terms [47]

$$C_{pw} = 0.80 \text{ and } C_{\epsilon w} = 4 \quad (3.42)$$

3.2.4 Combustion Modelling

Near the fire front and owing to the presence of hot spots (hot gases, burning particles, etc.), CO gas and soot particles resulting from the decomposition of the vegetation react

with ambient air to produce CO₂ gas according to the following equations, written for 1 kg of the fuel.



where $\nu_{O_2}^G = 4/7$ and $\nu_{O_2}^{Soot} = 8/3$ are the mass stoichiometric coefficients.

The combustion rate of CO gas is limited both by chemical kinetics and by the time required for effective mixing between the CO gas and ambient air. The rate of reaction determined from Arrhenius' kinetics law is evaluated as [48, 49, 50]:

$$\bar{\omega}_{CO}^{Ar} = \bar{\rho}^2 \tilde{Y}_{CO} \tilde{Y}_{O_2} K_{CO} \exp\left(-\frac{E_{CO}}{R_0 \tilde{T}}\right) \quad (3.45)$$

where the pre-exponential factor $K_{CO} = 7 \times 10^4 \text{ m}^3/\text{kg.s}$ and the activation energy $E_{CO}/R_0 = 8000 \text{ K}$. Mixing between the CO gas and the ambient air is mainly assured by the turbulent structures (eddies) located in the flaming zone. If the conditions are fully turbulent, the reaction rate can be written as a function of the local mass of reagents available for burning divided by the integral turbulent time scale (eddy dissipation combustion concept EDC) [48]:

$$\bar{\omega}_{CO}^{EDC} = \frac{C_A \bar{\rho}}{\tau_{mix}} \text{Min}\left(\tilde{Y}_{CO}, \frac{\tilde{Y}_{O_2}}{\nu_{O_2}^G}\right) \quad (3.46)$$

Constant C_A depends on the turbulent Reynolds number and is given by [48]:

$$C_A = -\frac{23.6}{Re_T^{1/4}} \frac{\chi}{(1 - \chi\gamma)} \quad (3.47)$$

where γ is the volume fraction of the small-scale turbulent structures and χ is the fraction occupied by the reaction zone inside these small structures, defined as follows:

$$\gamma = \frac{9.7}{Re_T^{3/4}} \quad \chi = \frac{Re_T^{3/4}}{2.13} \frac{\tilde{Y}_{CO_2} / (1 + \nu_{O_2}^G)}{\tilde{Y}_{CO} + \tilde{Y}_{CO_2} / (1 + \nu_{O_2}^G)} \quad (3.48)$$

The turbulent time scale τ_{mix} is the maximum between the integral turbulence time scale (k/ε) and $6\tau_\eta$, where $\tau_\eta = (\bar{\mu}/\bar{\rho}\varepsilon)^{1/2}$ is Kolmogorov time scale.

The rate of combustion of CO gas is finally obtained from:

$$\bar{\omega}_{CO} = -\text{Min}(\bar{\omega}_{CO}^{Ar}, \bar{\omega}_{CO}^{EDC}) \quad (3.49)$$

Consequently, the rates of destruction of O₂ and formation of CO₂ resulting from the combustion of CO gas are, according to Equation (3.43): $\bar{\omega}_{O_2}^G = \nu_{O_2}^G \bar{\omega}_{CO}$ and $\bar{\omega}_{CO_2}^G = -(1 + \nu_{O_2}^G) \bar{\omega}_{CO}$. Note, finally, that the rate of combustion of CO gas is also limited numerically by the available quantities of CO and O₂ gases in the fluid control volume considered during the time step considered. Because of the lack of information on soot production in a natural fire, the production rate of soot is limited to that resulting from the pyrolysis process [32] given by Equation (3.33). Assuming that the soot particles can be represented as carbon spheres of diameter $d_{Soot} = 1 \mu\text{m}$ and density $\rho_{Soot} = 1800 \text{ kg/m}^3$, the soot volume fraction field \tilde{f}_v can be evaluated from the following transport equation [49, 51]:

$$\frac{D(\bar{\rho}\tilde{f}_v)}{Dt} = -\frac{\partial}{\partial x_j}(\bar{\rho}\tilde{u}_j^{th}\tilde{f}_v) - \frac{\partial}{\partial x_j}(\overline{\rho u'_j f'_v}) + \frac{\bar{\rho}}{\rho_{Soot}} \left(\sum_m \dot{M}_{Soot}^m - \bar{\dot{\omega}}_{Soot} \right) \quad (3.50)$$

Note that the transport of the soot particles by convection is increased by the temperature gradient (thermophoretic velocity \tilde{u}_j^{th}) defined by:

$$\tilde{u}_j^{th} = -0.54 \frac{\bar{\mu}}{\bar{\rho}} \frac{\partial(\ln \tilde{T})}{\partial x_j} \quad (3.51)$$

The term $\bar{\dot{\omega}}_{Soot}$ results from soot oxidation and is evaluated from the rate for oxidation of pyrolytic graphite by O₂ as follows [49]:

$$\bar{\dot{\omega}}_{Soot} = 12 \tilde{f}_v \sigma_{Soot} \left[\frac{k_A \bar{P}_{O_2}}{1 + k_z \bar{P}_{O_2}} \zeta + k_B \bar{P}_{O_2} (1 - \zeta) \right] \quad \text{with} \quad \zeta = \left(1 + \frac{k_T}{k_B \bar{P}_{O_2}} \right)^{-1} \quad (3.52)$$

where $\sigma_{Soot} = 6/d_{Soot}$ is the surface area-to-volume ratio of soot particles, P_{O_2} is the partial pressure of oxygen, and the various reaction rates k_A , k_B , k_T and k_z depend on temperature as follows [49]:

$$\begin{aligned} k_A &= 200 \exp(-30000/R_0 \tilde{T}) \quad \text{kg/m}^2 \cdot \text{s} \cdot \text{atm} \\ k_B &= 4.46 \times 10^{-2} \exp(-15200/R_0 \tilde{T}) \quad \text{kg/m}^2 \cdot \text{s} \cdot \text{atm} \\ k_T &= 1.51 \times 10^6 \exp(-97000/R_0 \tilde{T}) \quad \text{kg/m}^2 \cdot \text{s} \\ k_z &= 21.3 \exp(4100/R_0 \tilde{T}) \quad \text{atm}^{-1} \end{aligned} \quad (3.53)$$

Having $\bar{\omega}_{soot}$, the rates of destruction of O₂ and of formation of CO₂ resulting from soot oxidation are found according to Equation (3.44): $\bar{\omega}_{O_2}^{soot} = -\nu_{O_2}^{soot} \bar{\omega}_{soot}$ and $\bar{\omega}_{CO_2}^{soot} = (1 + \nu_{O_2}^{soot}) \bar{\omega}_{soot}$.

3.2.5 Radiation Heat Transfer

Radiation is one of the most important heat transfer mechanisms contributing to the propagation of fire. It usually contributes at least 30% of the energy received by the vegetation located ahead of the fire front [37]. Total irradiance is given by:

$$J = \int_0^{4\pi} I d\Omega \quad I \text{ is the radiation density} \quad (3.54)$$

Radiation mainly results from soot particles produced in the flame and from embers located behind the fire front. Accounting for these two contributions, the variation of the radiative intensity I along an optical path s follows the radiation transfer equation (RTE) below, where σ_G is the absorption coefficient of the gas–soot mixture.

$$\frac{d(\alpha_G I)}{ds} = \alpha_G \sigma_G \left(\frac{\sigma \tilde{T}^4}{\pi} - 1 \right) + \sum_m \frac{\alpha_s^m \sigma_s^m}{4} \left(\frac{\sigma (T_s^m)^4}{\pi} - 1 \right) \quad (3.55)$$

where

$$\overline{\sigma_a T^4} \approx \overline{\sigma_a T^4} \left(1 + 6 \frac{\overline{T'^2}}{T^2} + 4 \frac{\overline{\sigma_a T'}}{\sigma_a T} \right) = \overline{\sigma_a T^4} \left(1 + 6 \frac{\overline{T'^2}}{T^2} + 4 \frac{\overline{T'^2}}{\sigma_a T} \frac{\partial \sigma_a}{\partial T} \right) \quad (3.56)$$

$$\frac{\partial \sigma_a}{\partial T} = 1862 \times \overline{f_{soot}}$$

Equation (3.55) accounts for turbulence–radiation interaction, where the temperature fluctuation variance $\overline{T'^2}$ is obtained from a transport equation (Equation (3.57)) that

assumes the simplest level corresponding to the isotropic eddy diffusivity model (also known as the simple gradient diffusion hypothesis), mentioned in [52].

$$\frac{D(\overline{\rho T'^2})}{Dt} = \nabla \left(\frac{\mu_T}{Pr_t} \nabla \overline{T'^2} \right) + 2P_t - 2\rho\epsilon_t \quad (3.57)$$

where

$$P_t = -\rho \overline{T' u'_j} \frac{\partial T}{\partial x_j} = \frac{\mu_T}{Pr_t} \frac{\partial T}{\partial x_j} \frac{\partial T}{\partial x_j} = \frac{\mu_T}{Pr_t} \left[\left(\frac{\partial T}{\partial x} \right)^2 + \left(\frac{\partial T}{\partial y} \right)^2 + \left(\frac{\partial T}{\partial z} \right)^2 \right]$$

Instead of using a transport equation for the rate of dissipation of temperature fluctuations, ϵ_t is obtained by assuming a constant ratio of time scales, usually equal to 0.5, between the dissipation of temperature fluctuation and the dissipation of turbulent kinetic energy [52]. This is also more consistent with the LES model where no transport equation is used for the dissipation rate of turbulent kinetic energy. Thus, we have:

$$R = \frac{T_t}{T} = \frac{1}{2} \quad T = \frac{k}{\epsilon} \quad T_t = \frac{\overline{T'^2}}{2\epsilon_t}$$

Consequently,

$$\epsilon_t = \frac{\epsilon}{k} \overline{T'^2}$$

The final equation for $\overline{T'^2}$ takes the form

$$\frac{D(\overline{\rho T'^2})}{Dt} = \nabla \left(\frac{\mu_T}{Pr_t} \nabla \overline{T'^2} \right) + 2P_t - 2\rho \frac{\epsilon}{k} \overline{T'^2} \quad (3.58)$$

By definition, the temperature fluctuation variance $\overline{T'^2}$ is

$$\overline{T'^2} = \frac{1}{P} \int_t^{t+P} (T - \bar{T})^2 dt \quad (3.59)$$

where P is the averaging time period. Since $T_0 < T < T_{adiab}$, $\overline{T'^2}$ is bound from above as:

$$\overline{T'^2} \leq \text{Min}[(T_{adiab} - \overline{T})^2, (\overline{T} - T_0)^2] \quad (3.60)$$

given that T_0 is the reference or ambient temperature and T_{adiab} is the adiabatic flame temperature. Taking into consideration the temperature fluctuations in RTE results in increasing the source term $\overline{\sigma_a T^4}$ by a factor of $(1 + F + G)$ where

$$F = 6 \frac{\overline{T'^2}}{\overline{T}^2} \quad \text{and} \quad G = 4 \frac{\overline{T'^2}}{\overline{\sigma_a T^4}} \times 1862 \times \overline{f_{soot}} \quad (3.61)$$

This will substantially increase the radiation intensity in radiation-dominated fires and ensure fire propagation in situations with no wind.

3.3 Numerical Method

The analysis used to describe the numerical method is based on the standard finite volume method and the velocity–pressure coupling algorithm that are reported in [53]. In this section, we draw the outlines of the method, emphasising the numerical improvements brought to earlier 2D work [34]: the space and time schemes, turbulence model wall treatment, linear systems solvers and performance of the solver.

3.3.1 Fluid Phase and Solid-Phase Meshes

Using a fully implicit finite volume method, fluid-phase transport Equations (3.18) to (3.21), (3.46) and (3.38) are solved in Cartesian coordinates in a rectangular domain by a fully-implicit finite volume method using a segregated formulation [54] on a structured and non-uniform staggered-mesh. The computational domain is subdivided into a number of cells using a wall-refined mesh, as shown in Figure 3.1. If we consider direction y for example, the positions of the cell's interfaces measured from a wall located at $y = 0$ would be:

$$y(j) = L \left(\frac{j-1}{N} \right)^q \quad \text{for } j = 1, 2, \dots, N + 1 \quad (3.62)$$

where L is the position of interface $N + 1$ and $q \geq 1$ defines the degree of mesh refinement ($q = 1$ results in a uniform mesh). The size of the fluid-phase mesh ($\Delta_x, \Delta_y, \Delta_z$) is chosen to accurately describe the coherent structures observed in a fire; moreover, it helps to avoid fire extinction within the solid fuel bed for radiation-dominated fire propagation, so that the mesh size cannot exceed a maximum value given by [33]:

$$\text{Max}(\Delta_x, \Delta_y, \Delta_z) < \frac{4}{\sum_m \alpha_s^m \sigma_s^m} \quad (3.63)$$

Where the term $\alpha_s^m \sigma_s^m / 4$ is the coefficient of extinction within the solid fuel bed corresponding to vegetation family m .

The cell size adjacent to the wall is chosen where its centre P falls within the fully turbulent region or the log-law region of a turbulent boundary layer [53] where the rate of turbulence production equals the rate of dissipation (equilibrium turbulence). So, the dimensionless distance y^+ is given by:

$$y^+ = \frac{\bar{\rho}_p C_\mu^{1/4} k_p^{1/2} y_p}{\bar{\mu}_p} \quad (3.64)$$

such that $11.63 \leq y^+ \leq 500$, where y_p is the distance of node P to the wall (closest cell center to the wall). In the fluid phase model, the variables are either scalar, stored at the centre of the cells, or vectorial with components defined at the midpoint of the cell face.

The solid phase domain, which is embedded in the fluid domain, is also subdivided into a number of cells using a rectangular uniform mesh, which defines the solid fuel elements. The size of the solid-phase mesh ($\Delta_x^S, \Delta_y^S, \Delta_z^S$) is also chosen according to Equation (3.63), and Equations (3.10) to (3.15) are solved for each vegetation family m and for each solid-fuel element separately.

Finally, the interaction between the fluid phase and the solid phase often requires estimating the variables of one phase at the grid points of the other; this is simply done by linear interpolation.

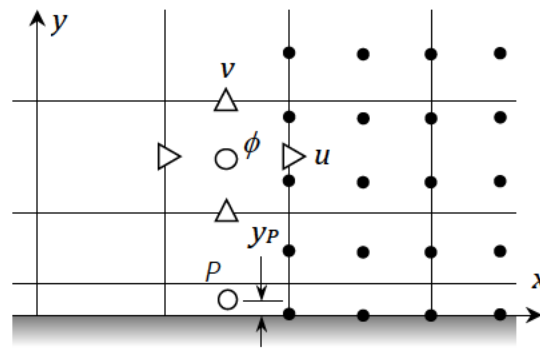


Figure 3.1: Structures of the fluid-phase mesh (—) and of the solid-phase mesh (•) in the x - y plane, and staggered locations of the fluid-phase variables (scalar variables ϕ and velocity field components u and v).

3.3.2 Solving Procedure and Solver Performance

At $t = 0$, the boundary conditions are applied and the fluid phase and solid phase are initialised. Given the variables fields at time t_{n-1} , the solution at time $t_n = t_{n-1} + dt_n$ is found after several iterations of the following resolution sequence:

1. Solving Equation (3.21) for the mass fractions of chemical species CO, O₂, CO₂ and H₂O; then, the mass fraction of N₂ is deduced. CO gas at a temperature of

1600 K is injected through the bottom of the computational domain, which initialises the sequence to solve the transport equations.

2. The soot fraction transport Equation (3.50) is solved.
3. The radiative transport Equation (3.55) is solved using a Discrete Ordinate Method (DOM), consisting of the decomposition of the radiation intensity in a finite number of directions. This set of discrete contributions is integrated using a numerical Gaussian quadrature rule (the S8⁷ method is often used) for calculation of the total irradiance [55] and the interpolation of the radiation intensity is done using Step, Diamond, or Non-Standard schemes.
4. The set of ordinary differential Equations (3.10) to (3.15) describing the evolution of solid fuel are solved using a fourth-order Runge–Kutta method (RK4). For each vegetation family m and for each solid-fuel element separately, the four consecutive steps of RK4 are applied to a six-variable vector consisting of: $\alpha_S^m \rho_S^m Y_{H2O}^m$, $\alpha_S^m \rho_S^m Y_{Dry}^m$, $\alpha_S^m \rho_S^m Y_{Char}^m$, $\alpha_S^m \rho_S^m$, α_S^m and T_S^m .
5. After solving the enthalpy Equation (3.20), we can deduce the temperature from the enthalpy temperature dependence (Equation 3.28) using the CHEMKIN data base, and then we can update the physical properties: density, heat capacity, dynamic viscosity and thermal conductivity.
6. The fields of turbulent kinetic energy k and its dissipation rate ε are obtained from Equations (3.38) and (3.39).

⁷ The discrete ordinate S8 method refers to the number of directions (8 x (8 + 2)) along which the radiation equation is solved

7. Solving the Navier–Stokes Equations (3.18) and (3.19), we can find the flow fields (velocity components and dynamic pressure). Using the PISO algorithm in which the mass conservation constraint is satisfied by turning the continuity equation into a pressure equation, we can treat the velocity–pressure coupling. The PISO algorithm determines the pressure field using a pressure equation and requires no pressure correction, which introduces instability into the convergence process of unsteady solutions.

At the end of each iteration, the residuals of all transport equations are computed both in normalised or non-normalised forms. Global convergence is assumed to be achieved at the end of the iteration if the residuals of all transport equations reach a preset stopping value, 10^{-5} for normalised forms and 10^{-4} for the non-normalised form. On the other hand, a time step t_n is repeated with a time increment $dt_n/2$ in the following cases:

- The normalised and non-normalised stopping criteria are not met after a preset number of iterations (typically 30 iterations).
- An increase by a factor of 10 of the largest L_2 -norm [53] during two consecutive iterations.
- A temperature increase exceeding the present maximum value (usually 200 K) at any node of the fluid phase.

3.3.3 Time Scheme Transport Equations

In general, and for a generic variable ϕ , where \vec{V} is the velocity factor, Γ_ϕ is the diffusion coefficient and S_ϕ is a source term, the convection-diffusion term can be written as follow:

$$\frac{\partial \bar{\rho} \tilde{\phi}}{\partial t} + \bar{\nabla} \cdot (\bar{\rho} \tilde{V} \tilde{\phi}) = \bar{\nabla} \cdot (\Gamma_{\phi} \bar{\nabla} \tilde{\phi}) + S_{\phi} \quad (3.65)$$

The time scheme is fully implicit, providing the method non-conditional stability as far as the time step is concerned. The unsteady term in Equation (3.65) is approached by a third-order Euler time-scheme; hence, its time discretisation at time t_n is written as:

$$C_0 (\bar{\rho} \tilde{\phi})^n + C_1 (\bar{\rho} \tilde{\phi})^{n-1} + C_2 (\bar{\rho} \tilde{\phi})^{n-2} + C_3 (\bar{\rho} \tilde{\phi})^{n-3} + \bar{\nabla} \cdot (\bar{\rho} \tilde{V} \tilde{\phi})^n = \bar{\nabla} \cdot (\Gamma_{\phi} \bar{\nabla} \tilde{\phi})^n + S_{\phi}^n \quad (3.66)$$

where the coefficients $C_0 = \frac{11}{6dt}$, $C_1 = -\frac{3}{dt}$, $C_2 = \frac{3}{2dt}$, $C_3 = -\frac{1}{3dt}$ if dt is a constant time

increment, while for variable ones, they are given by:

$$\begin{aligned} C_0 &= \frac{dt_{n-1}^2 + dt_{n-1} dt_{n-2} + 4 dt_n dt_{n-1} + 2 dt_n dt_{n-2} + 3 dt_n^2}{dt_n (dt_{n-1}^2 + dt_{n-1} dt_{n-2} + 2 dt_n dt_{n-1} + dt_n dt_{n-2} + dt_n^2)} \\ C_1 &= -\frac{dt_{n-1}^2 + dt_{n-1} dt_{n-2} + 2 dt_n dt_{n-1} + dt_n dt_{n-2} + dt_n^2}{dt_n dt_{n-1} (dt_{n-1} + dt_{n-2})} \\ C_2 &= \frac{dt_n (dt_n + dt_{n-1} + dt_{n-2})}{dt_{n-1} dt_{n-2} (dt_n + dt_{n-1})} \\ C_3 &= -\frac{dt_n (dt_n + dt_{n-1})}{dt_{n-2} (dt_{n-2}^2 + dt_n dt_{n-2} + dt_{n-1}^2 + dt_n dt_{n-1} + 2 dt_{n-1} dt_{n-2})} \end{aligned} \quad (3.67)$$

An adaptive time stepping algorithm based on the estimation of the truncation error associated with the time integrated scheme [41] is used to obtain the increment steps $dt_i = t_i - t_{i-1}$. At the beginning of time step t_n , a predicted solution of Equation (3.65) is obtained using a computationally inexpensive explicit third-order Euler method and used as an initial condition for the time step, and the correction is computed using the non-linear iterations associated with the implicit algorithm. $E(t_n)$ at time t_n is the norm of the difference between the predicted and corrected solutions in normalised form. The time

increment dt_{n+1} is then adjusted by comparing the truncation error with the desired level of accuracy E_d (typically between 10^{-4} and 10^{-2}) as follows [41]:

$$\frac{dt_{n+1}}{dt_n} = \left(\frac{E_d}{E(t_n)} \right)^{\frac{1}{TO+1}} = SFAC \quad (3.68)$$

where TO is the time-scheme order ($TO = 3$ in this case). If the time step change factor $SFAC > 1$, the next time increment is increased by $SFAC$, and if $SFAC < 1$, it is decreased by $SFAC$. However, $SFAC$ is limited between 0.5 and 1.2 to avoid an overshoot of the solution at t_{n+1} , and the time increment itself is also limited between the preset minimum and maximum values.

3.3.4 Convection Scheme

The third-order QUICK scheme [56] is used to approach the convection term of Equation (3.65) in order to avoid numerical diffusion. Referring to Figure 3.2, for a positive convective flux at face w (i.e. $u_w > 0$), the value ϕ_w of a scalar variable ϕ at face w is obtained from:

$$\phi_w = \frac{B_1}{B} \phi_W + \frac{B_2}{B} \phi_P + \frac{B_3}{B} \phi_{WW} \quad (3.69)$$

where $B_1 = \delta x_2 \delta x_3 (\delta x_2 + \delta x_3)$, $B_2 = \delta x_1 \delta x_3 (\delta x_3 - \delta x_1)$, $B_3 = -\delta x_1 \delta x_2 (\delta x_1 + \delta x_2)$, and $B = B_1 + B_2 + B_3$. Note that for a uniform mesh, the well-known coefficients are recovered:

$$\frac{B_1}{B} = \frac{6}{8}; \frac{B_2}{B} = \frac{3}{8}; \text{ and } \frac{B_3}{B} = -\frac{1}{8}$$

For a negative flux at face w (i.e. $u_w < 0$), a similar expression involving ϕ_w , ϕ_P and ϕ_E is used. Numerical instability may result in this classical form of the QUICK scheme, owing to the appearance of negative main coefficients of the discretised transport equation. By placing troublesome negative coefficients of the discretised equation in the source term according to the formulation of Hayase et al. [57], we can avoid the stability problem. Finally, the numerical wiggles often associated with the use of the QUICK scheme are avoided by opting for the first-order upwind scheme in regions exhibiting a wiggling solution. This is done by computing the ratio of upwind-side gradient to downwind-side gradient; for a positive flux at face w (i.e. $u_w > 0$), this ratio is given by:

$$r_w = \frac{\phi_P - \phi_W}{\phi_E - \phi_P} \quad (3.70)$$

For a positive ratio (the solution is monotonic), the QUICK scheme is used and ϕ_w is given by Equation (3.69), while for a negative ratio (the solution exhibits a gradient sign change), the upwind scheme is used (i.e. $\phi_w = \phi_W$) to reduce the risk of numerical wiggles.

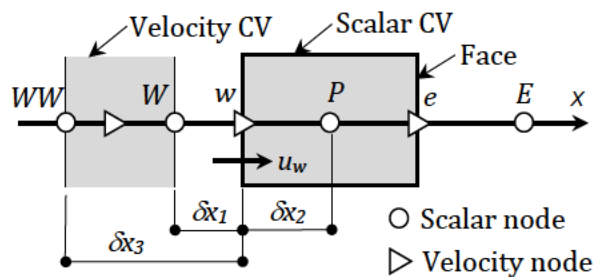


Figure 3.2: Fluid-phase mesh structure and notations in one direction

Chapter 4 : Junction Fire Configuration Setup

4.1 Physical Problem

The idealisation of a junction fire consists of a formulation in which two linear fire fronts that intersect, making an angle θ between them, spreading on a uniform fuel bed making an angle α with the horizontal reference plane, spread in such a form that the junction point advances tending to form single straight line resulting from the two original ones [4, 10, 9]. In Figure 4.1, a general idea about the geometry of a junction fire and the fundamental parameters considered in this study is represented. The junction fires studied here include the case of fires with a single wind component U that is parallel to the longitudinal (X) axis. A homogeneous distribution of a single type of fuel (Erica shrub) is used with a very low packing ratio (0.00784) and a thickness of 15 cm. The ignition starts along two 5-m-long lines (red line in Figure 4.1) making an angle θ between them.

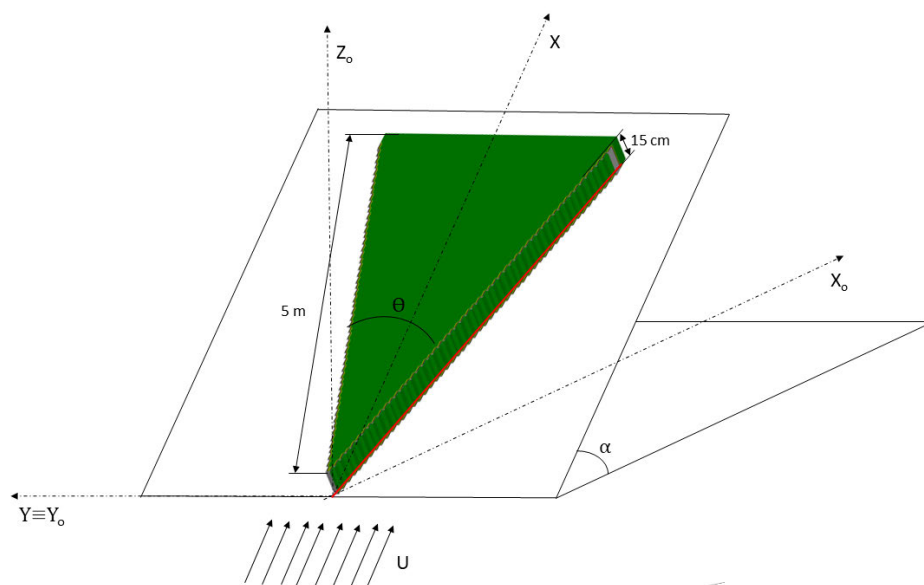


Figure 4.1: Schematic representation of junction fire on a slope with a single component of wind

According to Raposo et al. [9], at the start of the merging process, the ROS of the junction point increases very rapidly, given the very high values of ROS that it can reach, this is considered the acceleration phase. Even on a horizontal fuel bed, the ROS can reach very high values. The fire behaviour can be represented as a fast jump of the junction point, which is followed by a steady decrease in ROS over time, referred to as the deceleration phase. Radiation was found to be the primary mechanism only during deceleration. This process is intensified by the reduction of the initial angle between the two fire lines or by the presence of an aligned slope or wind [9].

Once the two fire fronts merge at the junction point, a very complex and dynamic set of processes starts to develop in which the geometrical and physical properties of the fire fronts change continuously. A characteristic feature of this type of fire is the rapid propagation of the junction point that causes the V-shaped fuel bed to burn and flames to jump. The rapid acceleration of the fire front near the flame induced by the fire is similar to the jump fire behaviour described by Viegas et al. [4].

4.2 Experiments Against which Model Validation was Conducted

The junction fire experiments used for model validation were conducted at the Forest Fire Research Laboratory (LEIF) of the University of Coimbra, in Lousã, using the Canyon Table DE4 [4], which has a useful area of $6 \times 8 \text{ m}^2$ with a slope that can be changed in the range of 0 to 40° (Figure 4.2).



Figure 4.2: Photo of the canyon table DE4 [58].

The fuels used in the experiments were dead pine needles of *Pinus pinaster*, shrubs containing a mixture of *Erica* and *Avena sativa* straw. The fuel load was kept constant (0.6 kg/m^2). In each test, the fuel moisture content m_f was measured.

The ignition of the two fire lines was made by two people to assure that the fire lines started burning simultaneously. For this purpose, two wool threads soaked in a mixture of petrol and diesel oil were used along the border of the fuel bed. The lines were quickly set on fire by the operators (see Figure 4.3). The simultaneous ignition of such large fire lines is a delicate process, particularly in tests with high values of slope angle.

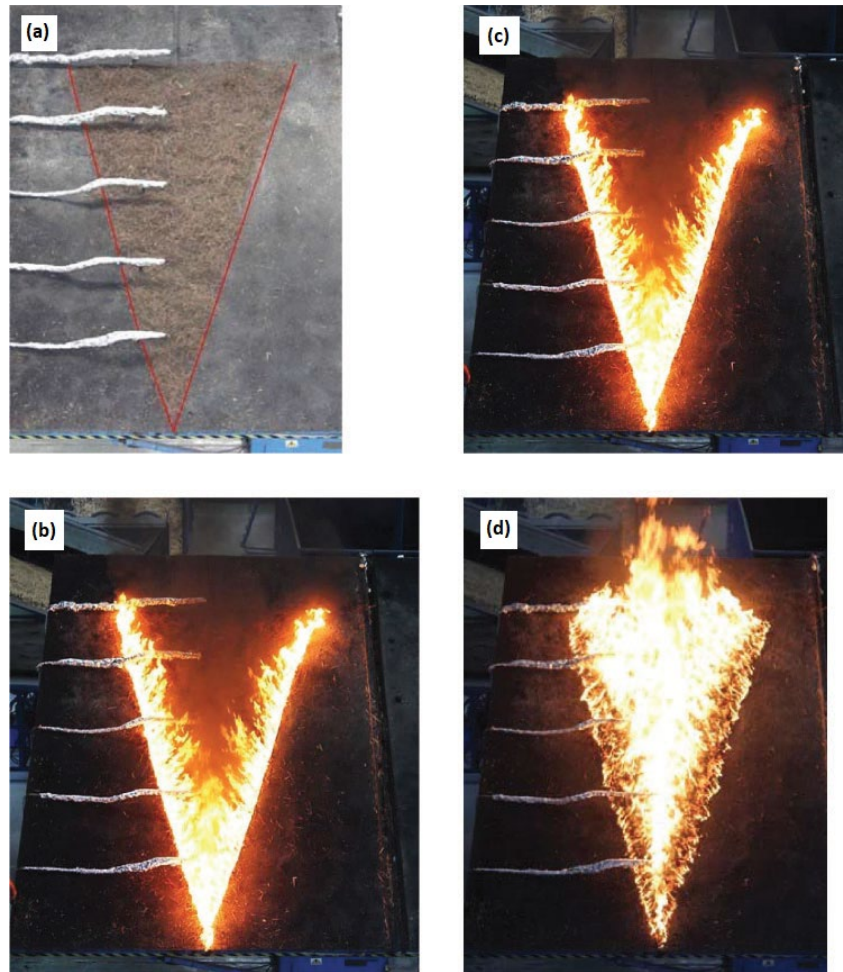


Figure 4.3: General view of combustion table DE4 during preparation and tests: (a) reference image before the test. The Pitot tubes can be seen on the left side of the table. At ignition: (b) time $t = 0$ s; (c) $t = 2$ s; (d) $t = 18$ s [9].

The results of ROS evaluation using thermocouple data and IR images were compared and it was found that both methodologies were equivalent [10], but as the image analysis allowed better temporal and spatial resolution of the processes, it was the one adopted (see Figure 4.4). From the thermocouple data and the time interval required for the fire to travel from one position to the next, the ROS of the fire along the X axis was estimated as well. The presence of the fire front was assumed for values of temperature above 350°C , which was considered a sign of the existence of flame at the place and time of measurement.

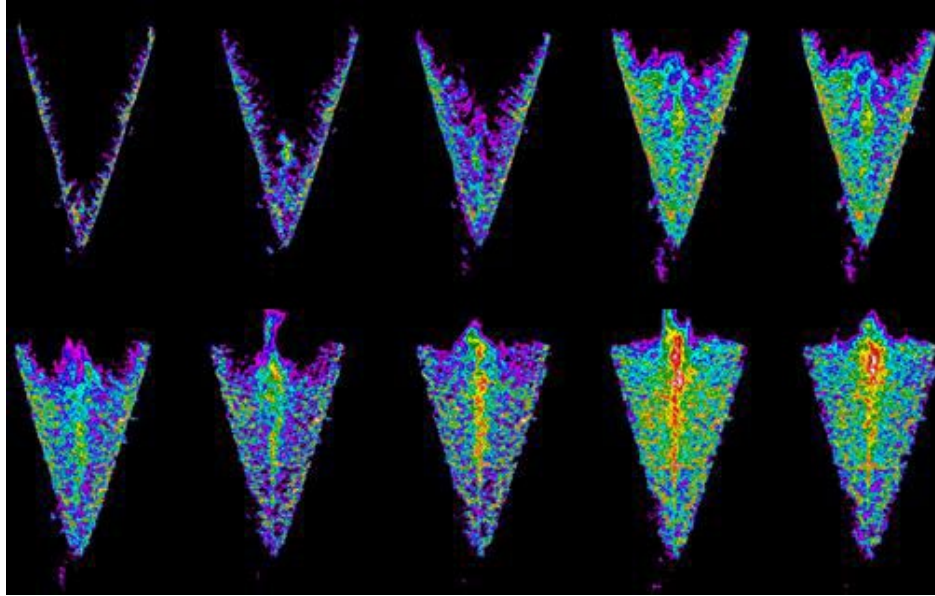


Figure 4.4: Infrared frames from a junction fire test. The time between frames is 4 s [9].

The experiments were designed to measure the fire spread rate with fuel bed slopes ranging from 0 to 40°, as measured from the horizontal plane. Four different junction angles θ (20, 30, 40 and 45°) were used with three different fuel types, resulting in 28 different experimental tests. Only five duly-chosen experiments with shrubs as vegetative fuel were selected for our study.

4.3 Shrub Junction Fire Numerical Configuration

The first objective of this study is to show that the model is able to predict numerically the spread of a junction fire through shrubland. The experiments reported in Raposo et al. [9] provide many experimental measurements that could be used to validate the present simulation results. The ROS is the quintessential parameter to quantify the dynamic behaviour and main output of the experimental measurements, along with fire perimeter evolution, junction angle evolution, flow velocity and radiative heat flux. The ROS estimation is obtained from the time derivative of the position of the junction point. The

following configuration was used for the validation part and a similar one is adopted for the parametric study.

Numerical simulations using FIRESTAR3D were carried out using V-shaped vegetation immersed inside a larger computational domain (29 m long, 29 m wide and 12 m high), as shown in Figure 4.5. Open boundary conditions [59] are imposed on all computational domain sides except its bottom where a solid-wall condition is applied. The homogeneous fuel bed, of height $\delta = 0.15$ m, is located 12 m away from the inlet boundary and lateral boundaries. The fire fronts are both 5 m long. The fuel used in this study was a shrub composed of a mixture of the genus *Erica*, often called heather. The fuel load was kept constant at 0.6 kg/m^2 , used experimentally. The ambient temperature and humidity ratio were 15°C and 50%, respectively.

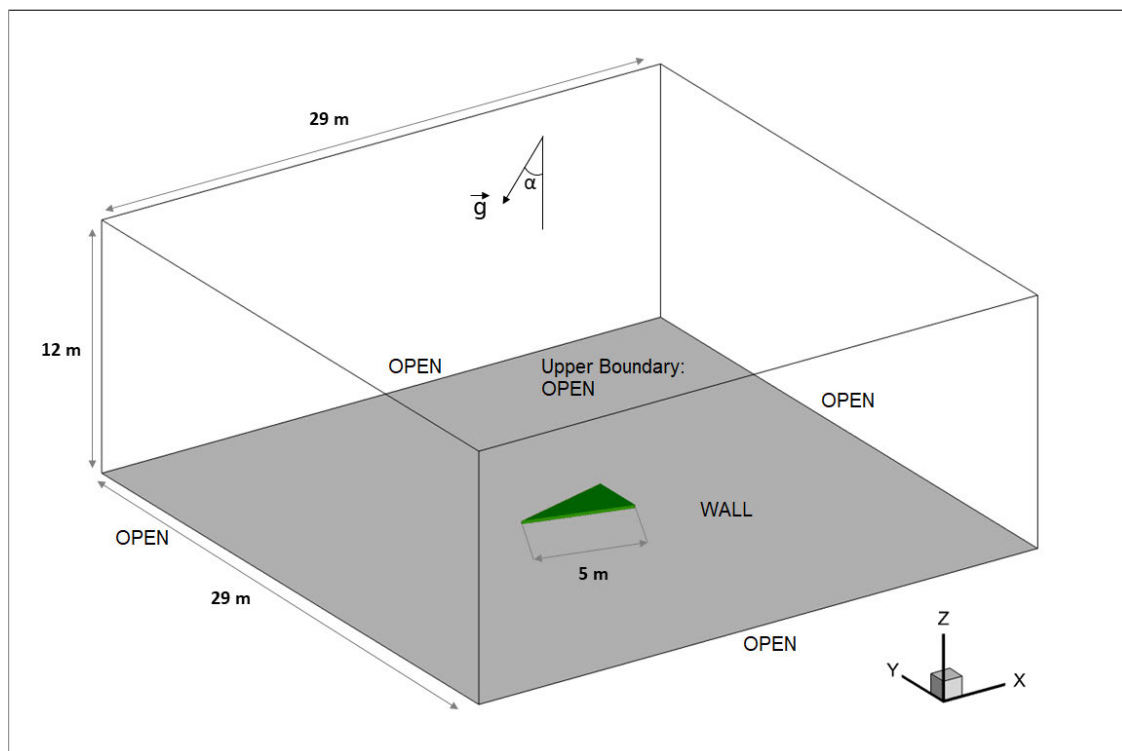


Figure 4.5: Perspective view showing the computational domain and the vegetation cover used in a V-shape.

The homogeneous fuel layer has the following main properties: fuel volume fraction $\alpha_S = 0.00784$, surface-to-volume ratio $\sigma_S = 6900 \text{ m}^{-1}$, dry material density $\rho_S = 500 \text{ kg/m}^3$, soot mass fraction $f = 0.05$. Solid-fuel particles are assumed to have a cylindrical shape and to behave as a black body with a drag coefficient $C_D = 0.42$ [60]. A uniform mesh with $(\Delta x, \Delta y, \Delta z) = (0.025 \text{ m}, 0.025 \text{ m}, 0.0125 \text{ m})$ is used for the solid phase, while a non-uniform grid of $160 \times 160 \times 160$ cells is used for the fluid phase to cover the whole computational domain. Within the vegetation zone, the fluid-phase grid is uniform with $(\Delta x, \Delta y, \Delta z) = (0.05 \text{ m}, 0.05 \text{ m}, 0.025 \text{ m})$, and then it is coarsened gradually toward the open boundaries according to a geometric progression coefficient. Both the solid-phase and the fluid-phase grids are characterised by cells sizes below the extinction length scale [33] within the vegetation given by $\frac{4}{\alpha_S \sigma_S}$, which equals 0.073 m in our case. To avoid false fire extinction, this value should not be exceeded, especially in the case of radiation-dominated fire propagation (i.e. when the wind speed is low to moderate). The domain inclination angle to the earth horizontal, α , is specified through the angle of gravitational acceleration to the z coordinate of the computation domain. In such a specified computation domain, gravitational acceleration has two non-zero components: $g_x = -g \sin(\alpha)$ and $g_z = -g \cos(\alpha)$, where $g = 9.81 \text{ m/s}^2$ is the acceleration due to gravity.

As mentioned above, open boundaries are applied on the computational domain sides (except the bottom), which allows the fire to create its own air flow. The main physical parameters used in all the configurations are tabulated in Table 4.1.

Table 4.1: Geometric and physical properties of the shrubland vegetation [9, 60].

Vegetation height δ	Solid-fuel volume fraction α_S	Surface/volume ratio σ_S	Dry material density ρ_S	Drag coefficient C_D	Thermal emissivity	Vegetation family shape
(m)		(m^{-1})	(kg/m^3)			
0.15	0.00784	6900	500	0.42	1	Cylindrical

To account for turbulence, the unsteady LES approach (constant Smagorinsky with $C_{SGS} = 0.07$) is used in the resolution of the conservation equations of mass, momentum, energy and chemical species. The minimum and maximum time-step values for the adaptive time-stepping strategy are set at 10^{-3} and 10^{-2} s, respectively, to obtain a truncation error less than 10^{-3} . Finally, global convergence is obtained (at each time step) when the L_2 -norms of all transport equations residuals reach 10^{-4} in non-normalised form.

The fire lines are ignited in the model by activating a burner. A 10-cm wide burner is activated instantaneously along both ignition lines by injecting CO gas at 1600 K from the bottom of the computational domain for 5 s. Ignition is activated after reaching a statistically steady profile of the turbulent boundary layer inside and above the fuel bed [61], which required 30 s in the case of the simulation with wind.

In FIRESTAR3D, tracking the fire front (in the case of junction fire, tracking the position of the junction point) can be done numerically using many methods. Experimentally, the fire front was located from the change in vegetation temperature, captured by IR cameras. Usually, a threshold value of 400°C is adopted. Numerically, this method is similarly used in some physics-based fire models, namely WFDS [62].

In junction fire, dynamic propagation is manifested by a very high propagation speed at the top of the vegetation and accompanied by flame jumps. Sometimes in small-scale simulations (likewise laboratory-scale experiments), fire ignition occurs in an unexpected location in the vegetation zone, making numerical tracking of the junction point harder.

To mitigate this problem and avoid false estimation of ROS, two ways of tracking the fronts were used in FIRESTAR3D. Those methods are based on examination of the amount of dry vegetation inside the vegetation zone and determine what is the so-called pyrolysis front. The amount of dry vegetation is given by α_{spS} in kg/m^3 and the edge where this quantity is zero is considered the flame edge, as represented in Figure 4.6. The junction point is assumed to be coincident with the midplane of the V-shaped vegetation.

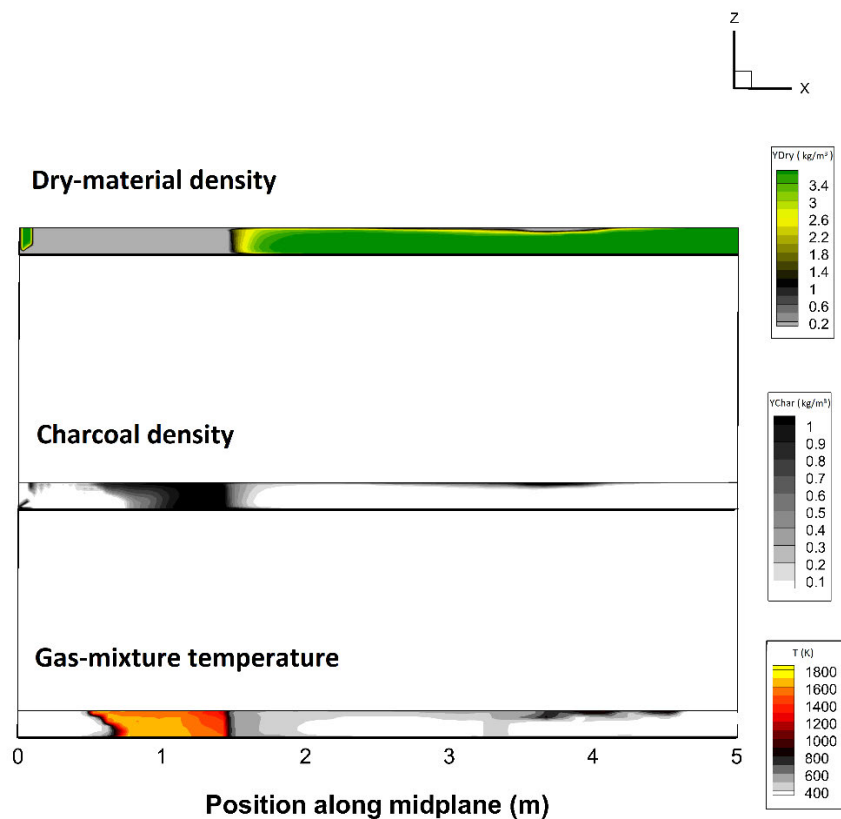


Figure 4.6: Solid-phase dry-material density (kg/m^3), charcoal density (kg/m^3) and gas-mixture temperature (K) within vegetation thickness in the midplane of V-shaped vegetation.

This junction point position could be defined:

- As the averaged fire front position in the midplane of the vegetation zone,
- Inside the vegetation (at 5 cm elevation).

The average method in the midplane takes into account every parcel of vegetation inside the midplane and the junction point position is determined according to the following formula:

Junction point position = vegetation length – (vegetation percentage × vegetation length)

In the second method (inside the vegetation) used to compensate for fire dynamics effects and accurately track the junction point, the edge is positioned inside the vegetation at an elevation of four cells (5 cm).

Additionally, two major outputs of FIRESTAR3D simulations are the heat generated (either convective or radiative) and the heat release rate (HRR). In fact, convective and radiative heat transfers play complementary roles in how quickly a fire spreads; therefore, it is important to comprehend how energy is released.

The modes of heat transfer (Q_{Rad} and Q_{conv}) are represented using power density, which is the net amount of energy received or emitted by the total vegetation. In the case of positive power density, the fuel receives more energy than emits and in the opposite case, the fuel emits more than receives. This energy could be either radiative or convective energy, calculated according to Equation (3.16).

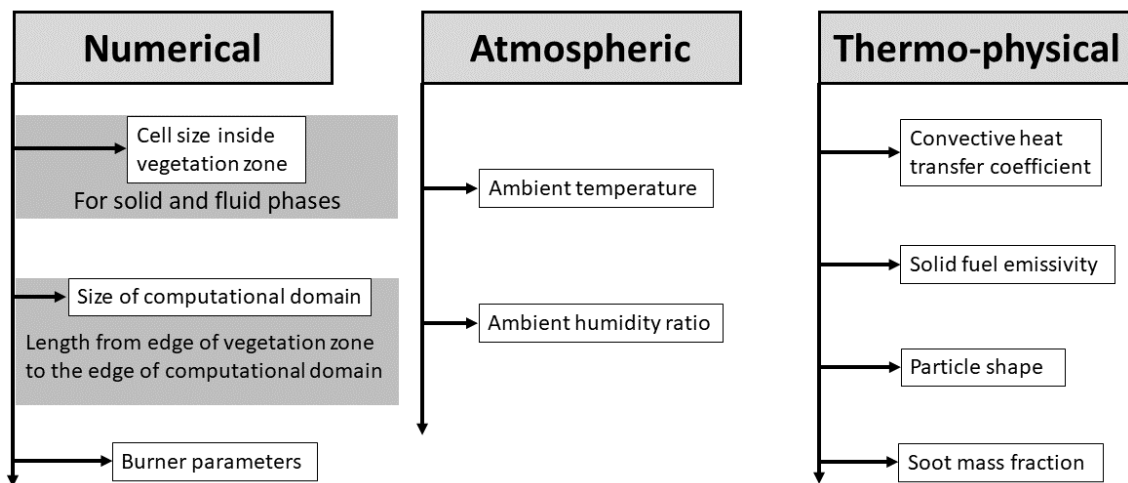
The heat release rate (HRR) of a fire is an indicator of the size of that fire. It is the energy released from the vegetation during the fire per unit time, or the rate at which the

combustion reactions produce heat. The HRR has units of watts (or kW, MW, etc.). Byram [63] defined it as the product of the weight of fuel consumed per unit area (kg/m^2), the heat yield of the fuel (average value assumed to be $18\,000\text{ kJ/kg}^1$ for most vegetative fuel) and the rate of spread (m/s), but this relationship is only suitable for the ideal case of a linear fire front spreading under quasi-steady conditions. This parameter is extensively used in forest fire research because it aids in determining prescribed burn limits, evaluating the effects of fuel treatment on fire behaviour and determining the consequences of fire on ecosystems. Additionally, it serves as a quantitative basis for fire suppression operations as well as an indicator for risk classification.

Chapter 5 : Sensitivity Study

This chapter is dedicated to quantifying the sensitivity of simulation and numerical results to a set of thermo-physical, atmospheric and numerical parameters. These parameters appear to be questionable especially for new numerical configurations and with incompletely characterised vegetative fuels like shrubs. Some testing into the role of the parameters was carried out with very limited ranges, including testing aiming to cope with numerical problems like divergence and numerical instability or slight overestimations in the validation study. The set of parameters tested in the following study is summarised in Table 5.1.

Table 5.1: Parameters tested in the sensitivity analysis



This sensitivity study aims to check the effects of some parameters in the numerical simulation of fire that try to cope with a few numerical instability problems and slight ROS overestimation; however, none of the following changes and attributed results were used in the validation or parametric study of junction fire. The aim was just to superficially examine the sensitivity of the numerical model and how results can be affected by them.

5.1 Soot Fraction

FIRESTAR3D includes a turbulent combustion model in the gaseous phase, and a multiphase model to represent the radiation heat transfer coming both from the gas species (H_2O , CO , CO_2 , etc.) and the soot. Good descriptions of some physical aspects such as turbulent combustion, radiation heat transfer, soot production and transport are among the major advantages of FIRESTAR3D over other physics-based models.

The development of a practical mathematical model for soot formation in turbulent flames is dependent upon finding the exact mass fraction for the vegetative fuel considered. According to Bankston et al. [64], the value of the soot fraction for Douglas fir ranges from less than 0.01 to 0.025 under flaming conditions. For a lucerne mixture, the mass of soot is very low, 0.001. The value 0.05 kg/kg was used in the present study and the sensitivity of this parameter was studied for a lower value of 0.005 kg/kg.

The result in Figure 5.1 indicates that the long-term ROS and the soot mass fraction (about 20 cm/s ROS in both cases) are unrelated. However, the ignition phase does change. This can be attributed to the increasing radiative heat fluxes, which are the driving mechanism for spread in the very early stages of the fire.

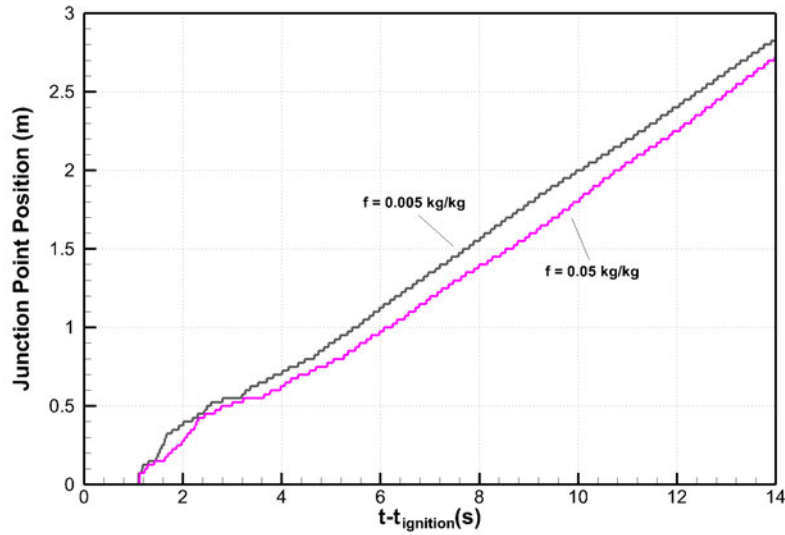


Figure 5.1: Junction point position for $\alpha = 20^\circ$, $\theta = 30^\circ$ with two values of soot mass fraction.

To assess the significance of the soot fraction factor, results are expressed in terms of measurable parameters in Figures 5.2 and 5.3. The local soot volume fraction \tilde{f}_v computed with Equation (3.50) is shown in Figure 5.2 for the two values of soot mass fraction. A decrease in the local distribution, which is a proxy for mass fraction, is proved.

Another interesting feature in FIRESTAR3D is the calculation of averaged parameters in both solid and fluid phases. Figure 5.3 represents the total volume flow rate of soot produced from fuel pyrolysis in the fluid phase for two different soot mass fraction. The average rate increased approximately 12 times (about $0.001 \text{ m}^3/\text{s}$ for $f = 0.005 \text{ kg/kg}$ and $0.012 \text{ m}^3/\text{s}$ for $f = 0.05 \text{ kg/kg}$) when f increased 10 times.

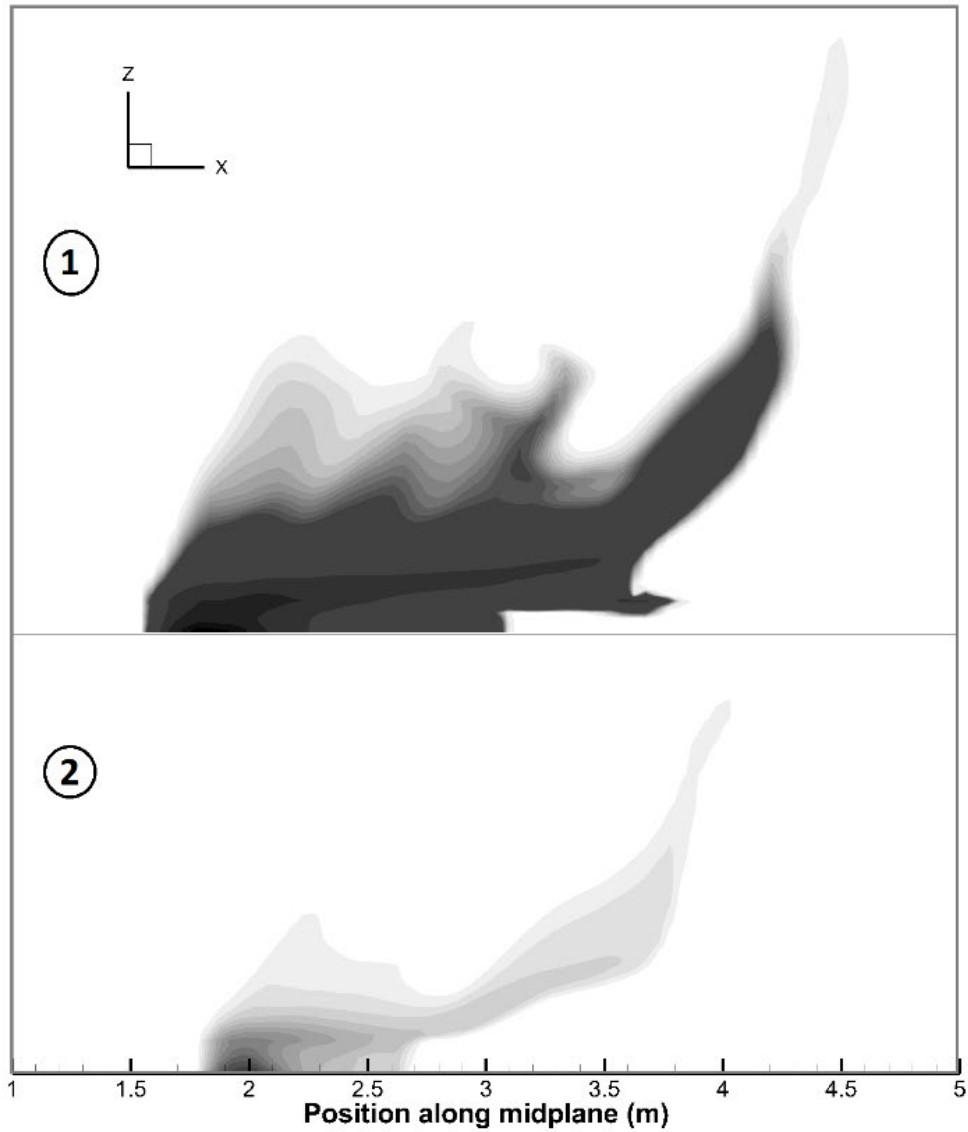


Figure 5.2: Local soot volume fraction for two value of soot mass fraction (above for 0.05 kg/kg, below for 0.005 kg/kg) in the midplane of the V-shape at $t - t_{\text{ignition}} = 9$ s for $\alpha = 20^\circ$, $\theta = 30^\circ$.

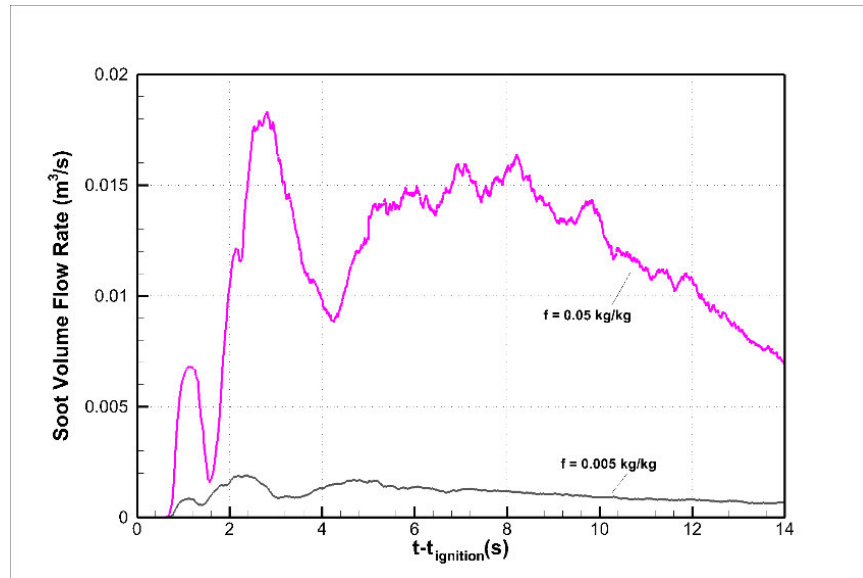


Figure 5.3: Total volume flow rate of soot for two values of soot mass fraction in case with $\alpha = 20^\circ$, $\theta = 30^\circ$.

A remarkable result is the reduction of the propagation speed at the top of the vegetation (no flame jump), as can be seen in Figure 5.4.

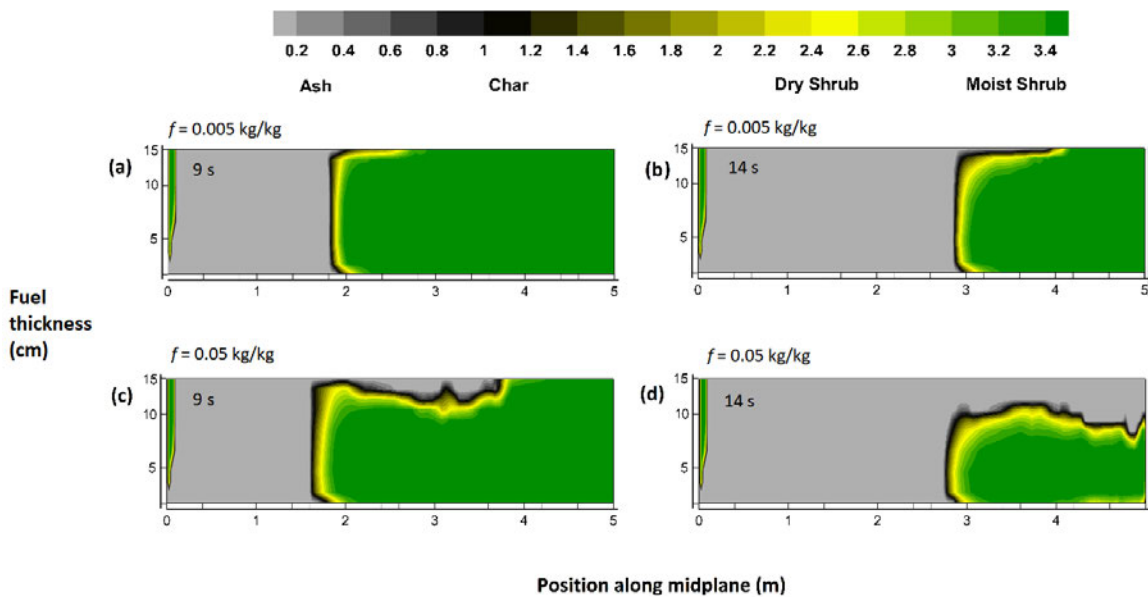


Figure 5.4: Cross-sectional views of the vegetation layer in the midplane of V-shaped vegetation showing the mass of dry material (α_{sp} in kg/m^3) at different simulation times: (a) and (c) at $t - t_{\text{ignition}} = 9$ s; (b) and (d) at $t - t_{\text{ignition}} = 14$ s, for two values of soot mass fraction: (a) and (b) for $f = 0.005$ kg/kg; (c) and (d) for $f = 0.05$ kg/kg for $\alpha = 20^\circ$, $\theta = 30^\circ$.

The fast propagation that is evident in most numerical simulations appears to be related to the mass fraction of soot particles in the fluid around the vegetation, which is a proxy for radiation coming from the flaming zone to the vegetation, especially the upper layers. Despite that, the ROS values are not influenced by the irregular propagation, as the junction point is tracked inside the vegetation (at 5 cm elevation); this feature in the numerical simulation is interesting and important for future investigations. A soot mass fraction of 0.05 kg/kg was used in all simulations in the validation and parametric studies.

5.2 Convective Heat Transfer Coefficient

The convective heat flux on the surface of a fuel particle is determined using a convective heat transfer coefficient, h_s , for a vertical cylinder. Experimentally, forced and buoyancy-induced convection in porous media have been studied extensively. However, most studies in this category have been restricted to packed beds and granular materials. There are relatively few investigations of transport phenomena in very high porosity media (more than 90%) such as vegetation models.

The correlation used for a cylinder or bunch of tubes may sometimes overestimate the amount of convective heat transfer for high-porosity medium. Calmidi et al. [65] conducted a detailed study of forced convection in high-porosity metal foams to quantify thermal dispersion and thermal non-equilibrium effects. The transport-enhancing effect of thermal dispersion is extremely low owing to the relatively high conductivity of the solid matrix. The Nusselt number was found to be reduced by half under such conditions (an empirical constant estimate of 0.57 represents the empiricism introduced in the Nusselt expression). Ghosh [66] analysed forced convection in high-porosity metal foam

analytically using a simplified cubic structure model. The microstructure-based heat transfer model takes into account heat conduction through filaments of the foam in conjunction with convective heat flow over the foam struts. The model shows significant heat transfer increase due to cross-connections in the foam filaments. Khan et al. [67] developed a heat transfer correlation assuming a simple cubic model of high-porosity open cell foam deduced from correlations using banks of tubes.

These studies may not be applicable in the case of high-porosity vegetative fuel, as the conductivity ultimately differs and other factors, such as the Reynolds number, should be taken into account. It is nonetheless interesting to adopt similar models for fire. In this section, sensitivity to the heat transfer coefficient was tested using a fifth of the calculated value.

The result of the simulations shows that the effect of this parameter on ROS is negligible in the case of a horizontal fuel bed, as seen in Figure 5.5. The ROS values were approximately equal (20 cm/s). However, a significant increase in ROS was found for the sloped fuel bed. Figure 5.6 shows that the propagation speed was the same for $t - t_{\text{ignition}} < 8$ s; then the profile for $h_s/5$ exhibited an acceleration with a ROS = 31 cm/s, compared with 20 cm/s for the profile with h_s . The total irradiance is shown in Figure 5.7 for the horizontal fuel bed. Apparently, irradiance increases when the convective heat transfer decreases. The heat transfer coefficient was not changed in the simulations in the validation and parametric studies.

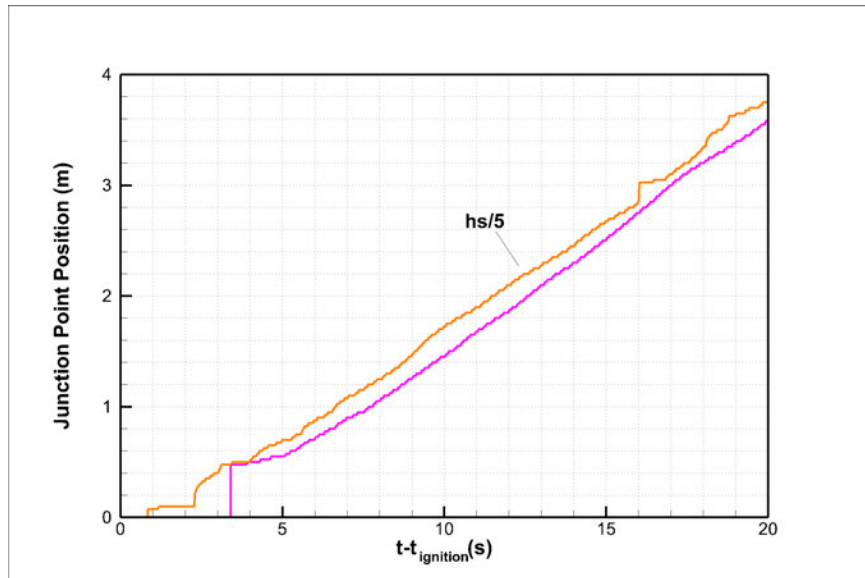


Figure 5.5: Junction point position with a fifth of the value of the heat transfer coefficient for $\alpha = 0^\circ$, $\theta = 30^\circ$.

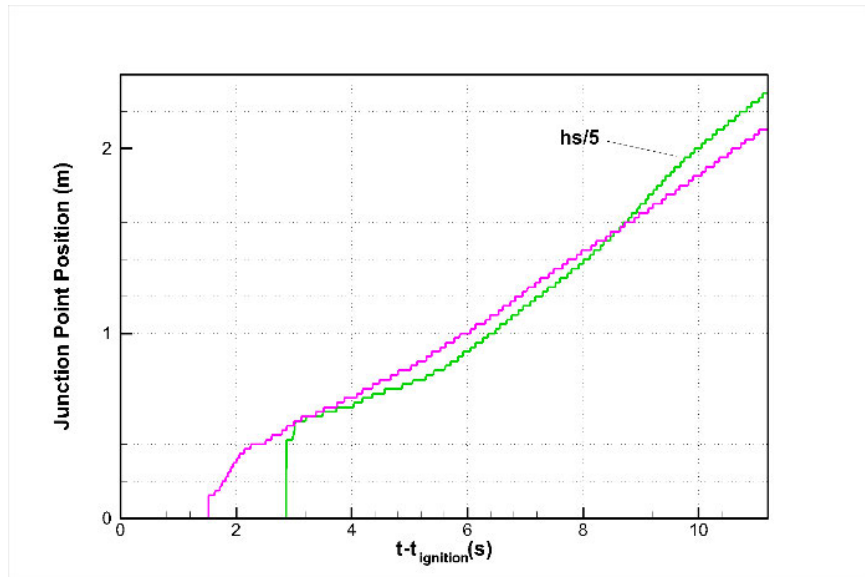


Figure 5.6: Junction point position with a fifth of heat transfer coefficient value for $\alpha = 20^\circ$, $\theta = 30^\circ$.

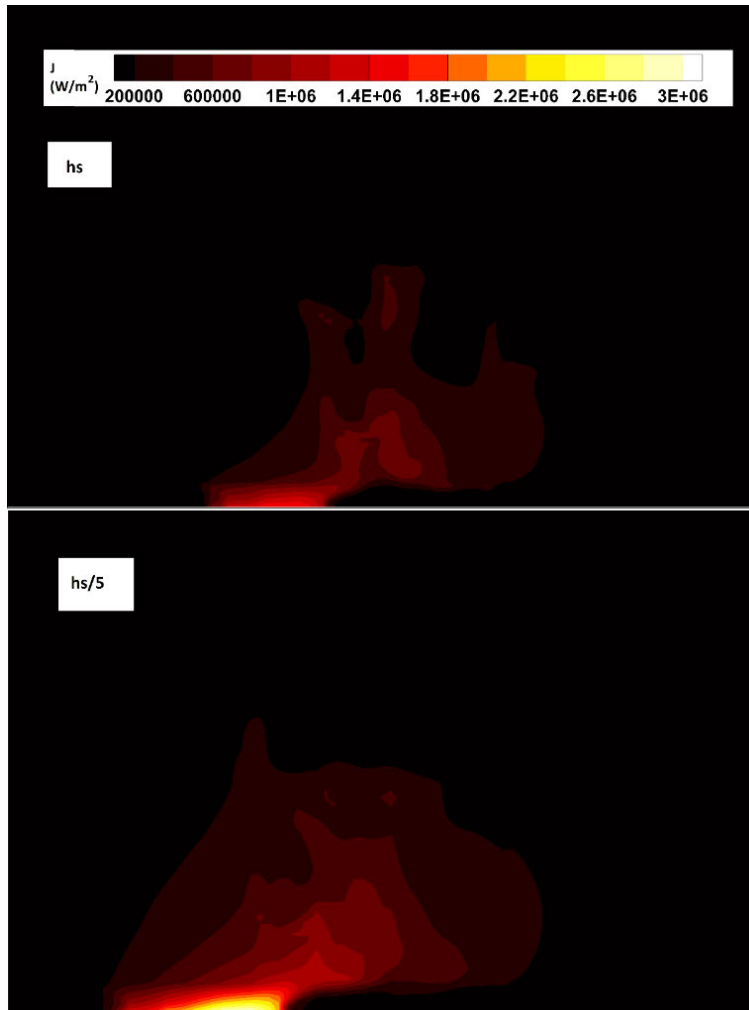


Figure 5.7: Total irradiance (W/m^2) at $t - t_{ignition} = 15$ s in the midplane of V-shaped vegetation for a horizontal fuel bed ($\alpha = 0^\circ$, $\theta = 30^\circ$) with different convective heat transfer coefficients.

5.3 Thermal Emissivity

The rate of heat transfer received by a solid-fuel element resulting from radiative heat exchange with the hot gases is represented by Equation (3.16) assuming the fuel particles behave as black bodies (the radiative behaviour of the vegetation can be approximated to that of a black body).

The radiative fraction is usually assumed in other physical models (i.e. FDS [19]) as a specified fraction of the fire's energy that is assumed to be emitted as thermal radiation,

as opposed to the heat that is drawn into the smoke plume (usually assumed to be 0.35 for grass).

Although this parameter has not been used in FIRESTAR3D and the radiative heat is computed according to relevant equations, a simulation using vegetation emissivity 0.5 was done. On the whole, emissivity did not affect junction point propagation (Figure 5.8). The figure shows almost matching curves, demonstrating no significant influence: the same ROS was found for both cases. The fuel was assumed to behave as a black body in the validation and parametric studies.

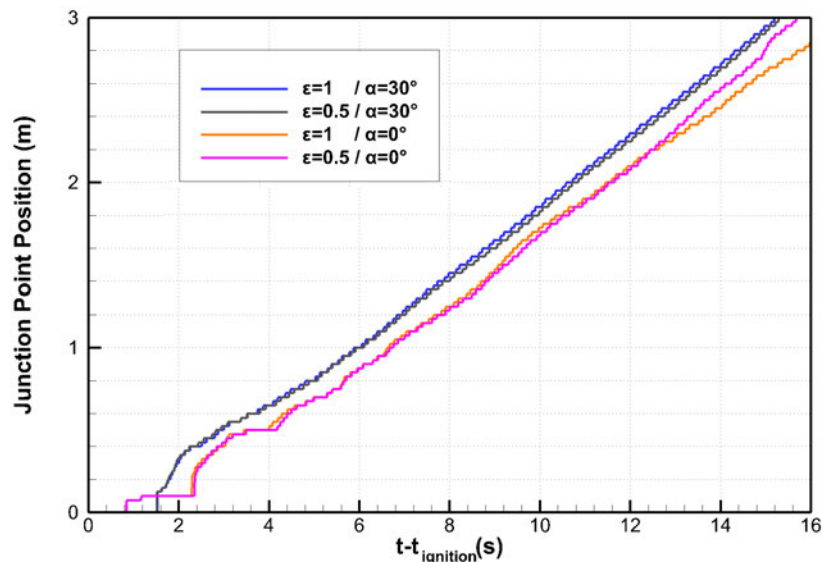


Figure 5.8: Junction point position for two vegetation emissivity values for the case $\alpha = 0^\circ, \theta = 30^\circ$.

5.4 Particle Shape

The heterogeneous character of the vegetation is taken into account using two possible shape families of solid fuel particles: cylindrical particles (usually used to represent branches, twigs and needles) and discs (usually used to represent flat leaves). The shape of the fuel particles is used for the description of their regression law and for the estimation

of the heat transfer coefficient. The convection heat transfer coefficient, h_s , depends on the shape of the fuel particles. The drag coefficient, C_D , is obtained from correlations that depend on the particle shape of vegetation family m .

For similar vegetation (e.g. various grasses, different eucalyptus species), a cylindrical solid fuel shape is usually adopted. A simulation using disc-shaped vegetation of 15 cm length was conducted, with no significant effect on the ROS (Figure 5.9). The fuel is represented using cylindrical elements in the validation and parametric studies.

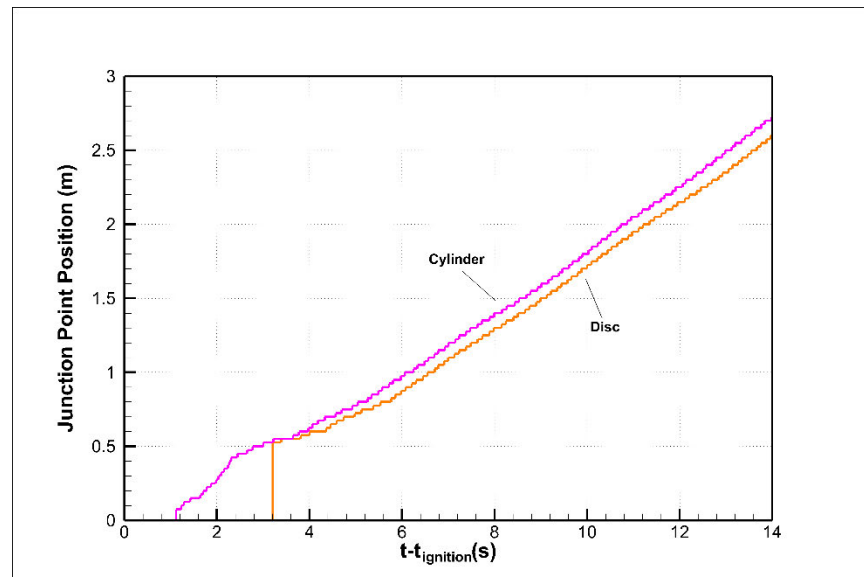


Figure 5.9: Junction point position for the case $\alpha = 20^\circ$, $\theta = 30^\circ$.

5.5 Ambient Humidity and Temperature

The coupled models include the interaction of wildfire with the surrounding atmosphere, which changes the fire environment via humidity, temperature, and wind speed and direction. They are all recognised as producing significant effects on fire. Temperature together with humidity and recent weather conditions (lack of rain, etc.) can be grouped together under the classification of heat conditions.

5.5.1 Humidity

Relative humidity (RH) is a measure of how much moisture is in the air. Expressed as a percentage, it describes the amount of water vapour in the air compared with the amount needed for the air to be saturated (i.e. 100% RH).

Humidity varies with temperature – as temperature increases, humidity decreases (and vice versa). Humidity is important because it affects fuel moisture content and therefore its flammability. For example, in dry conditions, moisture from fuels is transferred to the atmosphere and the fuels become increasingly flammable. Moreover, RH quantifies the mass fraction of O₂ in the surrounding air.

The relative humidity of air is considered to have a significant effect on ROS. Moinuddin et al. [68] demonstrated a relationship between RH (fuel moisture content) and ROS using a physical fire model.

5.5.2 Temperature

Ambient temperature (T_a) affects fire behaviour indirectly through its influence on fuel moisture content and local wind formation. Hence, as air temperature increases, fuel moisture content tends to decrease, and vice versa. Dew can form, which can cause fire to slow or even be extinguished. Also, the higher the temperature of the fuel, the more easily it will reach ignition temperature. In physical models, temperature affects the amount of energy required to heat vegetation before pyrolysis. Convective heat transfer is also a function of ambient temperature.

Although ambient temperature and relative humidity can be proxy for measured fuel moisture, this dependency was not used in FIRESTAR3D as the shrub moisture content

was fixed to the experimentally measured value. The combinations in Table 5.2 were used to quantify the effect of these parameters.

Table 5.2: Values of ambient temperature and humidity ratio used in the sensitivity study.

Test no.	C1	C2	C3	C4
T_a (°C)	15	15	25	25
RH (%)	50	10	50	0

Assessments of the impact of each parameter were done by changing only one parameter. For combination C1 and C2 ($T_a = 15^\circ\text{C}$, RH = 50 and 10%), the ROS decreased by 0.5 cm/s (see the junction point position in Figure 5.10). Similarly, for combination C3 and C4 ($T_a = 25^\circ\text{C}$, RH = 50 and 0%), the ROS increased by 1 cm/s.

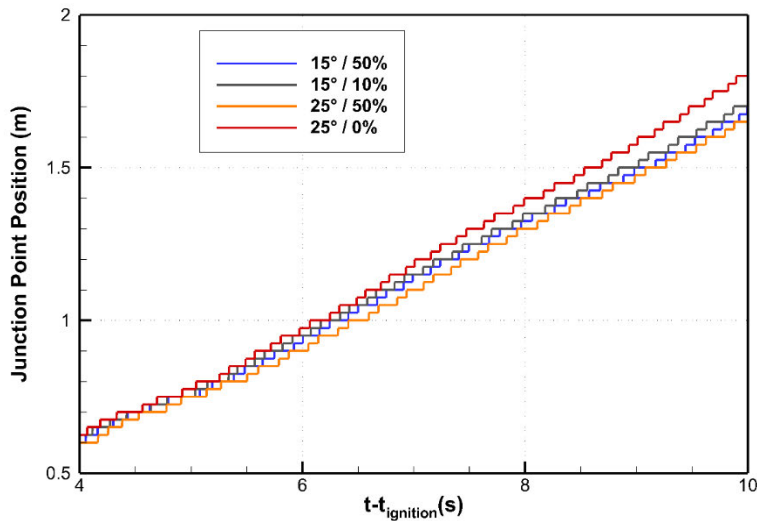


Figure 5.10: Junction point position for the four combinations of ambient temperature and humidity ratio.

The effect of ambient temperature is demonstrated by comparing the results of combinations C1 and C3 (RH = 50% and $T_a = 15$ and 25°C). A 10°C increase in the ambient temperature increases the ROS slightly. In the validation and parametric studies,

a temperature of 15°C and 50% humidity were used, similarly to the experimental conditions.

5.6 Burner Parameters

The numerical version of the burner includes some parameters that need to be carefully chosen to avoid numerical issues like excessive energy implementation or abrupt stop of energy input; however, it can affect the properties of fire if it is not suitably selected in regards to the size and scale of the fire. The fire lines are set in the model by activating the burner only in the zone determined by mathematical equations, taking into account the geometric parameters of the configuration as well as the junction angle variation between the fire lines. A 10-cm wide burner is activated instantaneously along both ignition lines by injecting CO gas at 1600 K from the bottom of the computational domain for a duration of 5 s.

At time $t = 2$ s, the average velocity V_{inj} of CO was maximum (equal to 0.01 m/s), and then it was decreased linearly with the mass of solid fuel consumed according to Equation (5.1). This procedure avoided destabilising the flame front by abruptly ceasing the CO injection and avoided any excessive external energy input.

$$V_{inj} = \left(1 - \frac{m_b}{m_{b0}}\right) \times (0.01 \text{ m/s}) \quad (5.1)$$

In Equation (5.1), m_b and m_{b0} represent the mass of dry material above the burner area and initially available above the burner area (i.e. the mass of dry material contained in the volume $V_{b0} = 5 \times 0.1 \times \delta \text{ m}^3$). Equation (5.1) was used between $t = 2$ and 7 s (during 5 s) as long as V_{inj} remained positive, and CO injection ceased if V_{inj} reached zero in this time interval.

However, experimentally, the ignition of the two fire lines was carried out by two operators using two wool threads soaked in fuel. We tried to replicate the experimental procedures and verify that the burner parameters did not affect the initial acceleration phase of the fire.

The two parameters that may affect the dynamics of the fire, especially in the acceleration phase, are the width of the burner and injection velocity. These parameters were tested for the values listed in Table 5.3 (specifically to quantify the effect on the initial value of ROS), for two slope conditions ($\alpha = 0$ and 30°).

Table 5.3: Set of values for burner width and CO injection velocity used in the sensitivity study.

Test no.	05	06	09	01
Burner width (cm)	25	1	1	10
V_{inj} (cm/s)	0.5	0.01	0.1	0.01

According to Figure 5.11, and taking into account Tests 06 and 09 (1 cm width and $V_{inj} = 0.01$ and 0.1 cm/s), the injection velocity change did not significantly affect propagation. Similarly, comparing Test 06 with Test 01 (10 cm and 0.01 cm/s), the increase in burner width did not change the ROS value significantly between 3 and 9 s while only a jump in junction point position (in the period before propagation start) occurred.

The ROS increased from 18 to 24 cm/s when the width increased from 10 to 25 cm and the injection velocity from 0.01 to 0.5 cm/s. Those appeared to be extreme values for such a scale. Because the cell size in all directions was 5 cm in the simulation (see Section 5.7), parameters in Test 01 were chosen (burning inside two cells).

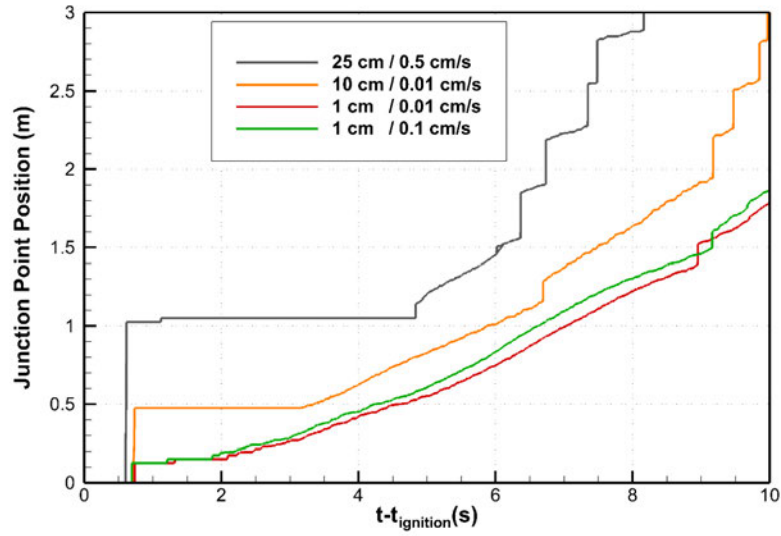


Figure 5.11: Junction point position in four simulations testing burner parameters (width and injection velocity) for $\alpha = 20^\circ$, $\theta = 30^\circ$

In the case of a horizontal fuel bed, the burner with parameters in Test 06 did not ignite the vegetation (red line in Figure 5.12).

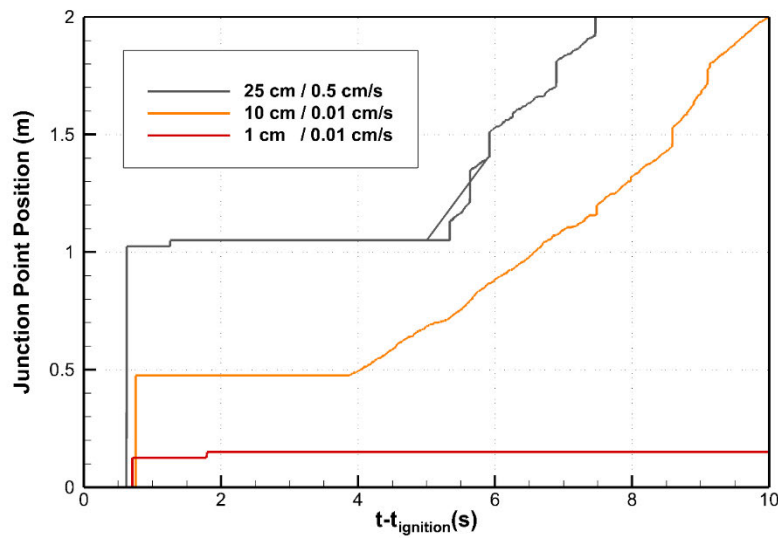


Figure 5.12: Junction point position in three simulations testing burner parameters (width and injection velocity) for slope angle $\alpha = 0^\circ$.

5.7 Domain Size and Mesh

Although a grid resolution is chosen below the extinction length, Ramirez et al. [69] recommended using a grid cell size three times less than the extinction length. Mesh and domain size sensitivity tests were carried out by increasing and decreasing the cell size by 30%. To that end, several simulations were carried out using cells of the following sizes: 3.5, 5 and 6.5 cm. Moreover, three sizes of computational domain with distances from the vegetation region to the open boundaries of 10, 12 and 15 m were considered, as detailed in Tables 5.4 and 5.5.

Table 5.4: Mesh parameters for the mesh sensitivity test (for a computational domain size of $29 \times 29 \times 12 \text{ m}^3$).

Minimum cell size in the xy plane	3.5 cm	5 cm	6.5 cm
Mesh size of the solid phase	$284 \times 284 \times 18$	$200 \times 200 \times 12$	$152 \times 152 \times 8$
Mesh size of the fluid phase	$202 \times 202 \times 163$	$160 \times 160 \times 160$	$136 \times 136 \times 158$

Table 5.5: Domain size for the sensitivity tests

Size no.	1	2	3
Domain size (m^3)	$25 \times 25 \times 10$	$29 \times 29 \times 12$	$35 \times 35 \times 15$
Mesh size of the fluid phase	$150 \times 150 \times 134$	$160 \times 160 \times 160$	$176 \times 176 \times 199$

Figure 5.13 shows the simulation results of the junction point position as a function of time for the cases listed in Tables 5.4 and 5.5. A minimal effect of grid resolution and domain size on junction point propagation is observed (except prior to 5 s). Consequently, the domain size and mesh considered (size 2 – mesh 5 cm) allow a solution that is quasi-

independent of these parameters as far as global fire behaviour is concerned (ROS, fire intensity, etc) to be obtained.

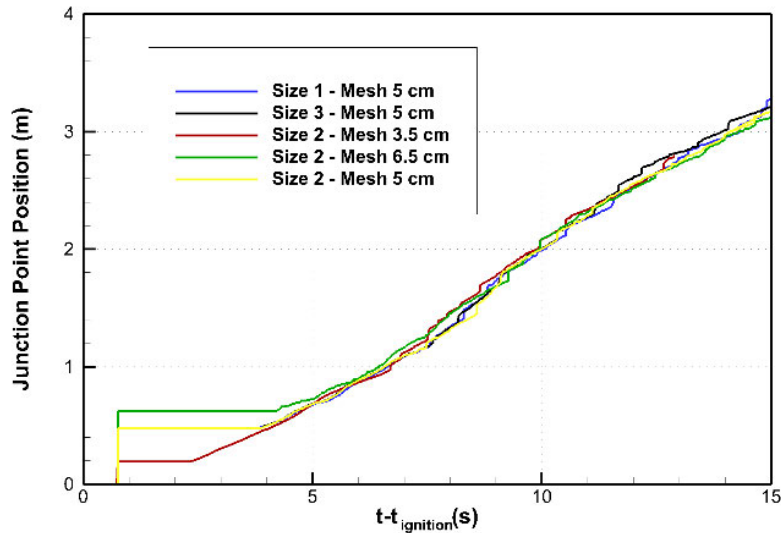


Figure 5.13: Junction point position in four sensitivity tests for $\alpha = 0^\circ$, $\theta = 30^\circ$.

5.8 Fuel Description

The fuels used in this study were a mixture of shrubs of the genus *Erica*, often called heather. The fuel load was kept constant at a value of 0.6 kg/m^2 , as used in the laboratory fires. Importantly, the physical properties of the shrub vegetation mentioned in Table 4.1 are characteristic properties [70]. Realistic simulations should take into account the heterogeneity of fuel in terms of the distribution of twigs and leaves and their percentages, as well as their specific surface-to-volume ratio. Most of the physical properties of shrubs used by Raposo et al. [9] can be found in the literature [71] and a complex method of describing shrubs (a combination of leaves and twigs) is presented in Table 5.6. A simulation was carried out using multiple fuels (Table 5.6) to observe any differences of fire behaviour compared with the use of single fuel-element representation (Table 4.1).

Table 5.6: Geometric and physical properties of leaves and twigs of shrub vegetation.

	Surface/volume ratio, σ_s (m^{-1})	Dry material density, ρ_s (kg/m^3)	Solid-fuel volume fraction, α_s
Leaves ($D < 2.5$ mm)	7200	253	0.0108 (70%)
Twigs ($2.5 < D < 6$ mm)	920	970	0.001212 (30%)

The shrub was described using two methods. In both cases, the total initial volume fraction and mass were kept the same and are identical to those reported in reference [9]. A more realistic description of the vegetation (accounting for different sizes of solid fuel particles) can better reproduce fire dynamics, especially the mass loss process. For both descriptions, the same fuel moisture content was considered (same as the experimental value) and two dry material densities for the same genus of shrubs (*Erica*) that Raposo et al. [9] used in the experiment.

Regarding ROS, a good similarity of the front propagation for the single type of fuel and the combination of two fuels was observed (see Figure 5.14). The propagation is slightly quicker in the two-fuel case, which we attributed to the low percentage of large-diameter particles and very small surface-to-volume ratio (diameter) of small particles compared with the characteristic value adopted first (6900 m^{-1}). Besides that, limited information about the moisture content of the leaves and twigs can account for the slight overestimation. Overall, the use of multiple description levels manages to estimate ROS to a similar order of magnitude.

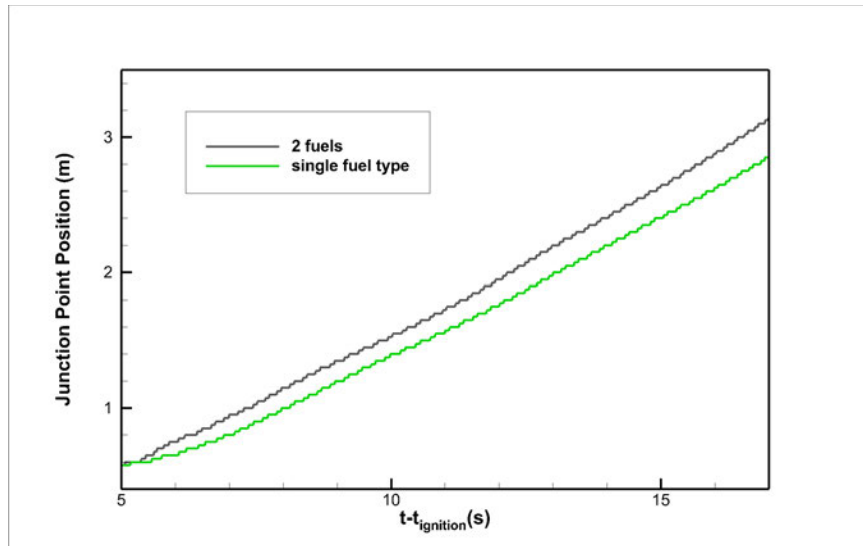


Figure 5.14: Junction point position for the different fuel combinations

5.9 Discussion

Each new numerical configuration requires conducting some sensitivity analyses that aim to test how the model results vary with variations of some important parameters. In the case of shrub fire, a set of parameters was tested to ensure that the numerical model, FIRESTAR3D, well describes the shrub particles (particle shape, soot fraction and the level of fuel description) exposed to fire. It appears that a single cylindrical element was sufficient to do the represents the fuel in the experiment. Soot fraction can have multiple effects on fire behaviour, so the soot mass fraction was kept to the average value used for similar vegetation. Some heat transfer parameters were tested just to examine the influence of these parameters and in other cases to avoid over-estimating them numerically in the case of high porosity medium. Overall, no changes were done as it requires further investigations in regards to the whole fire properties. The convective heat transfer coefficient was kept to the default value calculated for cylindrical element correlation. Similarly, the emissivity of the fuel element is kept as an ideal emitter. We

have also tested how with the variation of two ambient parameters (relative humidity and air temperature), the model outcomes change. The ROS is marginally sensitive to these parameters as they are not related to the vegetation moisture content. We adopt $T = 15$ °C and $RH = 50\%$. Finally, and as a part of every CFD simulation, the numerical parameters must be tested to ensure that the results are independent of any numerical selections. The size of the grid and of the computational domain was selected in a way conserving the balance between that goal and having adequate simulation time. A computational domain of distances from the vegetation to open boundary condition 12 m (no. 2) and cell size of the fluid domain in the vegetation zone of 5 cm are used.

The most important parameters, deduced from this limited sensitivity study, are those related to the heat transfer mechanism. Any change can not only affect the ROS but also ultimately change the amount of heat flux during the fire. The convective heat transfer coefficient should be further investigated in cases of low porosity medium. However, the ambient parameters especially the relative humidity are with minimal effect on fire propagation and behaviour. The results were not much sensitive to grid sizes as acceptable extinction length ($\frac{4}{\alpha\sigma}$) was used for all selected grids.

Chapter 6 : Validation Study

Validation of the fire numerical model FIRESTAR3D was carried out by comparing numerical results with the experimental measurements provided by Raposo et al. [9] for junction fire. The main parameter used to compare the behaviour was the ROS of the junction point. In order to capture the effects of this parameter and to consistently compare flame properties, quasi-steady regions of acceleration and deceleration were identified. These regions were duly identified for all selected simulations, similarly to the experimental work that proved a pattern of behaviour was directly related to the selected parameters.

Five duly-chosen configurations (see Table 6.1) were simulated using FIRESTAR3D. The comparison between the simulations and the experiments is based on the measurement of the junction point ROS, assumed to lie in the mid-plane of the computational domain. Simulation number Sxxyy-Mzz is used to represent a simulation with xx junction angle, yy slope and zz% fuel moisture content.

Table 6.1: Physical parameters of the junction fires cases considered in the validation study.

Simulation number	ID in Raposo et al. work [9]	Fuel moisture content, m_f (%)	Junction angle, θ ($^\circ$)	Slope angle, α ($^\circ$)
S4530-M24	10-L48	23.91	45	30
S3000-M24	11-L49	23.91	30	0
S3030-M22	12-L50	21.65	30	30
S3020-M19	13-L51	18.76	30	20
S3030-M14	17-L56	13.63	30	30

3D views of the flame obtained for simulation S3030-M14 are represented in Figure 6.1. These results show clearly the potential of FIRESTAR3D in reproducing numerically a junction fire in shrubland.

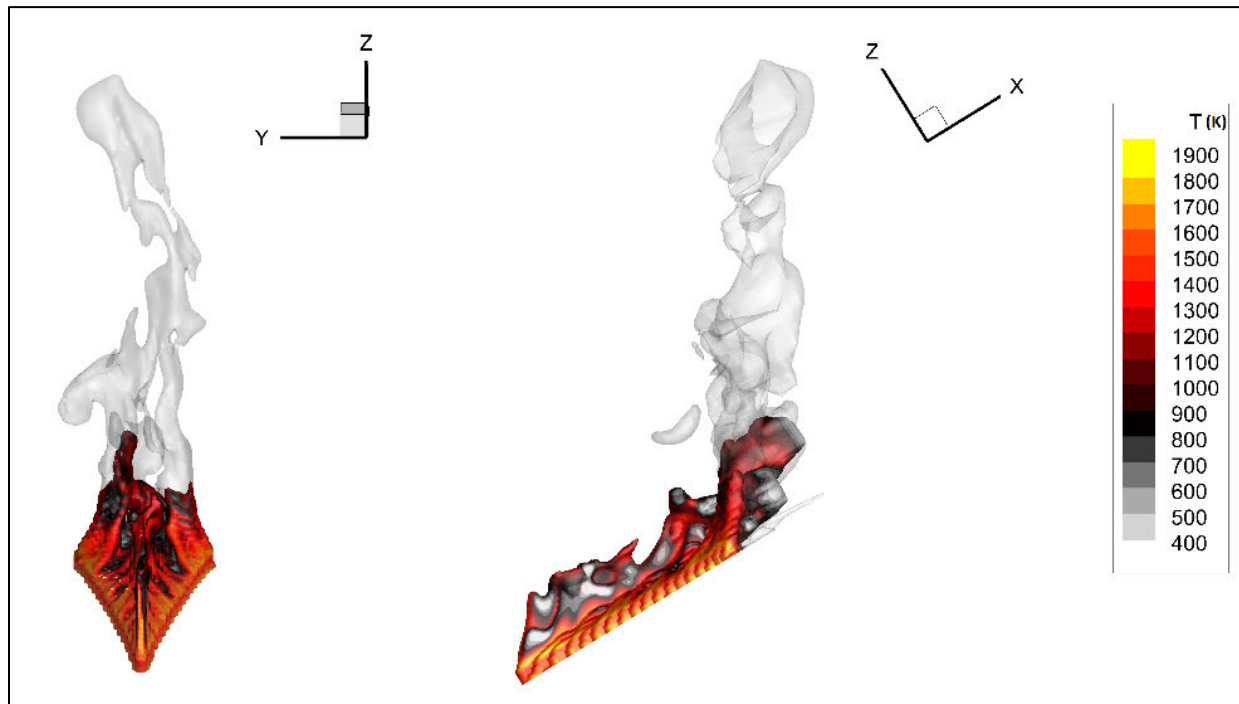


Figure 6.1: 3D front view (left) and side view (right) of an isovalue surface of the soot volume fraction (1.6×10^{-7}) coloured by gas temperature and an isovalue surface of the water mass fraction (9×10^{-3}) (in grey with 50% transparency) obtained for simulation S3030-M14, at $t - t_{\text{ignition}} = 10\text{s}$.

Figure 6.2 shows the evolution of fire perimeters. It can be seen that the junction fire angle is not fixed during propagation. Instead, it increases (on average) continuously; normally, studies characterise junction fire behaviour by the initial junction angle.

The process of merging these fires is not by the closure of the space between the fire lines by a reduction of their respective angle, similarly to closing scissors. On the contrary, it is the junction point that advances, tending to form a single straight fire line resulting from the two original fires.

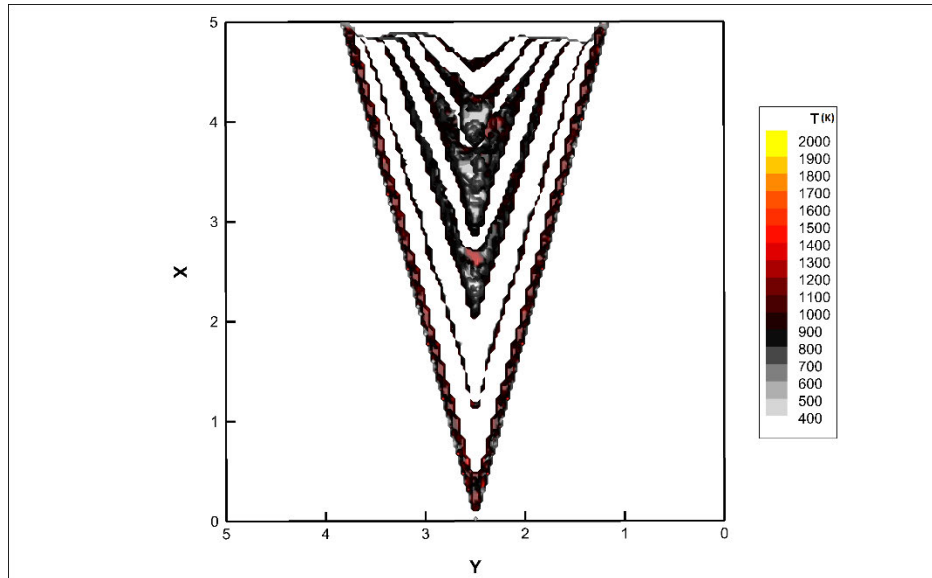


Figure 6.2: Evolution of fire perimeter according to pyrolysis edge (dry material $\alpha_{ps} = 0.001 \text{ kg/m}^3$) for S3000-M24. The first perimeter (outer) is at $t - t_{\text{ignition}} = 5 \text{ s}$ and the time difference between each perimeter is 5 s.

6.1 Effect of Slope Angle

Simulations S3000-M24, S3030-M22 and S3020-M19 have the same junction angle ($\theta = 30^\circ$) and close fuel moisture content values ($21.35 \pm 2.55\%$), while the slope angle varies ($\alpha = 0, 30^\circ$ and 20° respectively). Figure 6.3 shows the simulation and experimental ROS results for these three simulations.

First and foremost, the behaviour under the change of slope angle is clear in the simulated ROS results. Considering the maximum ROS, the value increases with the increase of slope angle (see Table 6.2). Experiment 13 (ID in Table 6.1) does not seem to be reflecting this effect as the maximum value (12.5 cm/s) is close to the maximum value for experiment 11 (12 cm/s) and way from 20 cm/s, the maximum value for experiment 12. This could be attributed to fluctuations that occurred during the experiments (probably due to the ignition procedure) or IR camera measurement inaccuracy.

Table 6.2: Maximum ROS values deduced numerically.

Simulation number	ROS _{max} (cm/s)
S4530-M24	20
S3000-M24	17
S3030-M22	24
S3020-M19	23.5
S3030-M14	25.5

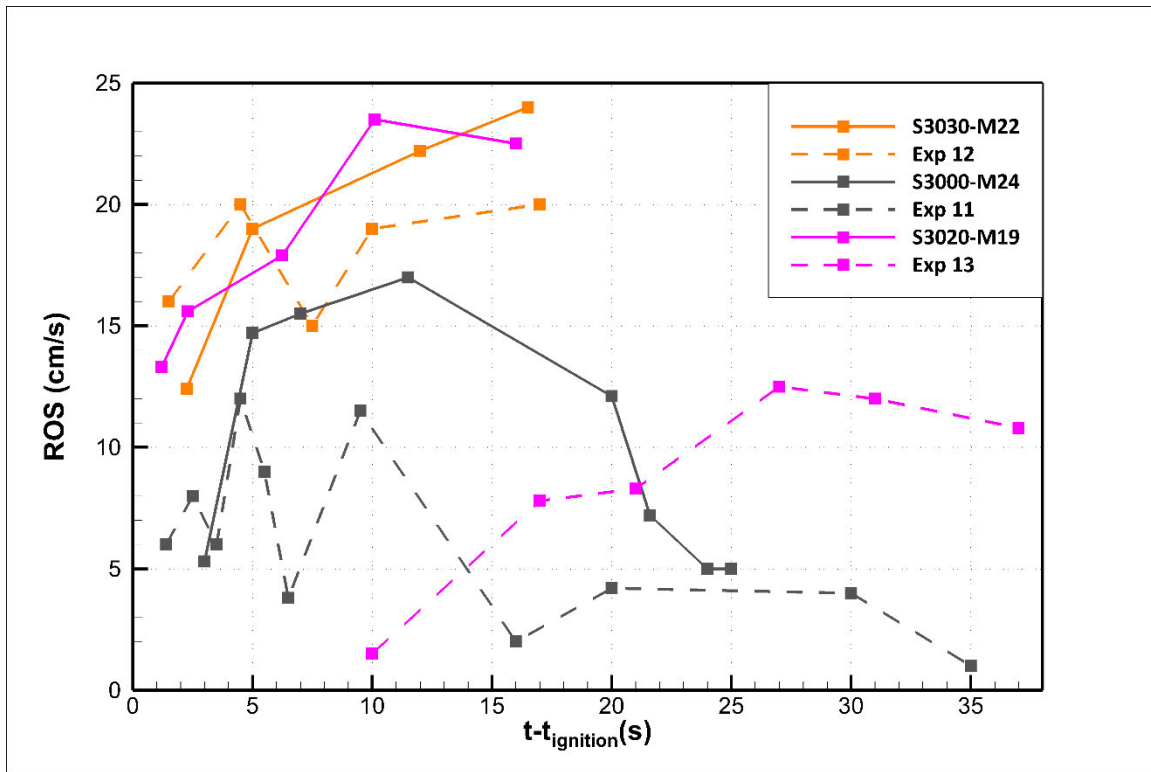


Figure 6.3: Evolution of the value of ROS for three different slope values (α) as a function of time.

The increase of slope angle from 20 to 30° affects ROS slightly, unlike in the experimental measurement, where the ROS for a slope angle of 20° seems to be underestimated.

The existence of acceleration and deceleration propagation phases has been observed in simulations as well as in experiments. The deceleration phase was significant in simulation S3000-M24 ($\alpha = 30^\circ$), slight in simulation S3020-M19 ($\alpha = 20^\circ$), and absent in

simulation S3030-M22 ($\alpha = 0^\circ$). Both propagation phases can be seen from the perimeter evolution in the non-slope case in Figure 6.2, where the distances between consecutive junction points increase, then progressively decrease.

6.2 Effect of Junction Angle

In simulations S4530-M24 and S3030-M22, the slope angle is 30° and the junction angles are 45° and 30° respectively. The fuel moisture content values are close; therefore, the effect of the junction angle can be deduced. The results are depicted in Figure 6.4.

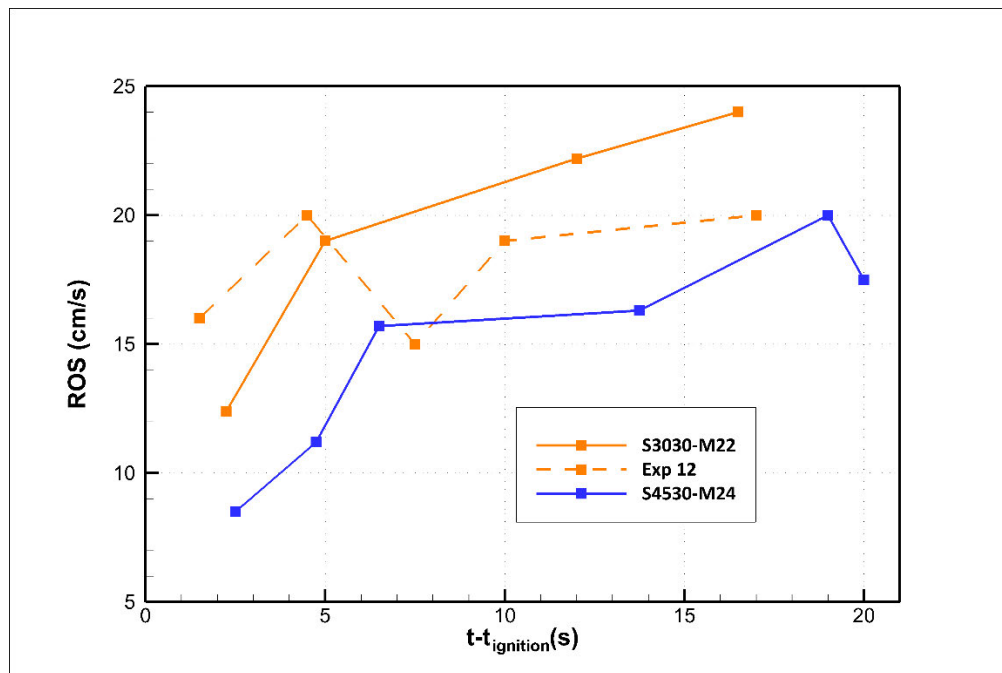


Figure 6.4: Evolution of the value of ROS for two different junction angles θ as a function of time.

It appears that the importance of the junction angle is paramount, consistent with the findings of Viegas et al. [4] for non-slope conditions. In the paper of Raposo et al. [9], the number of experiments with shrubs is small; however, a thorough investigation for a wider range of angles was numerically conducted in this study Chapter 7).

Regarding these simulations, an increase of 15° in junction angle decreased the maximum ROS by 4 cm/s, which correctly reflected the experimental results. Experimental measurements for simulation S4530-M24 were not provided in the publication of Raposo et al. [9], but the anticipated behaviour (deduced from experiments with different vegetative fuels [9]) is proved.

6.3 Effect of Moisture Content

Experiments 12 and 17 were conducted with the same topographical angles but the fuel in experiment 17 was drier (8% fuel moisture content difference). The simulations capture this difference only by a slight increase in the maximum ROS; however, the accelerative behaviour does not change (Figure 6.5).

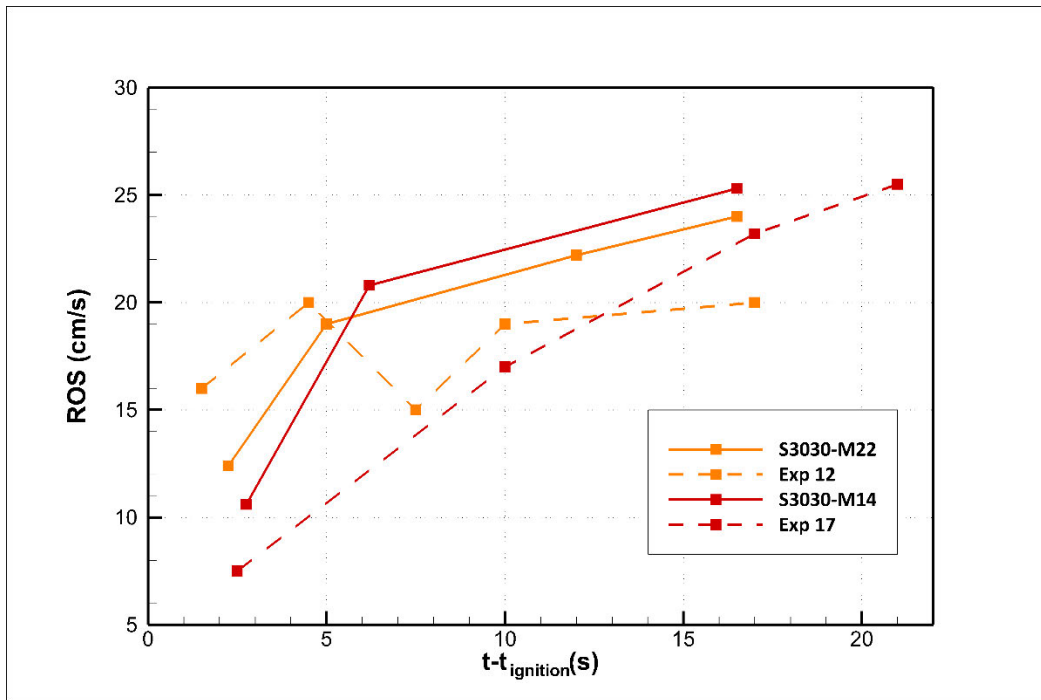


Figure 6.5: Evolution of the value of ROS for two different moisture content values (m_f) as a function of time.

6.4 Discussion

The simulation results showed the typical behaviour seen in all experimental investigations of junction fire: there is a rapid initial acceleration of the fire front in the region where the two fire lines intersect, followed by subsequent slowing, consistent with the behaviour reported by Viegas et al. [4, 10] and Raposo et al. [9].

The behaviour in the simulations with different junction angles is qualitatively similar. For instance, the smaller the junction angle, the more rapid the initial advance of the junction point (see Figure 6.4). This is expected on purely geometric grounds, and has been proved experimentally with different vegetation types. Similarly, good quantitative agreement, confirmed by a set of sensitivity analyses for the most important numerical parameters, was found using FIRESTAR3D, proving the efficacy of physics-based models in replicating junction fires. Overall, the average percentage of agreement for all validation cases (except case S3020-M19) was 74.2%.

For higher slope (20°), it is presumed that there are some experimental incorrect measurements in case Exp 13, but for case Exp 12 and 17, agreement is quite good. For slope 0° (Exp 11), the maximum value might be overestimated. However, at the early stage, the agreement is very good.

The FIRESTAR3D results appear to be promising for looking into the mechanisms associated with dynamic fire behaviour, especially in fire coalescence configurations, and to thoroughly understand the processes behind junction fire behaviour.

Chapter 7 : Parametric Study – Junction Fire without Wind

7.1 Configuration Description and Numerical Parameters

This chapter presents a parametric study of junction fires with a wide range of topographical angles (slope and junction angles) using the validated model FIRESTAR3D. To further examine the relative influence of different factors on final fire spread, we conducted a parametric analysis by varying key parameters one at a time, keeping everything else at the base case levels and examining different numerical findings, and investigated the interactions among parameters.

For the one-way parametric analysis, we varied two parameters one at a time with the values used presented in Table 7.1. The numerical configuration was kept the same, in order to conduct the parametric study in the same experimental environment and conditions (i.e. matching shrub fuel bed, scale, atmospheric conditions, ignition method, etc.). The designation of each simulation is according to both angles. For instance, S3020 is the simulation for junction fire with a junction angle of 30° and slope angle of 20°.

In each case, the length of the fire fronts was fixed at 5 m; as a result, the course of propagation decreased with increase in junction angle; therefore, we limited the study to a maximum junction angle of 90°. The fuel moisture content (m_f) was fixed in the study at 20%. The numerical parameters used in the chapter 6 were kept the same in this part.

Table 7.1: Cases simulated in the parametric study

$\alpha (\theta)$	15°	30°	45°	60°	90°
0°	✓	✓	✓	✓	✓
10°	✓			✓	✓
20°	✓	✓	✓	✓	✓
30°				✓	✓
40°	✓	✓	✓	✓	✓

The size of the refined mesh zone (vegetation zone) was changed according to the junction angle, as represented in Figure 7.1, while the distances around the vegetation were kept the same (12 m in all directions).

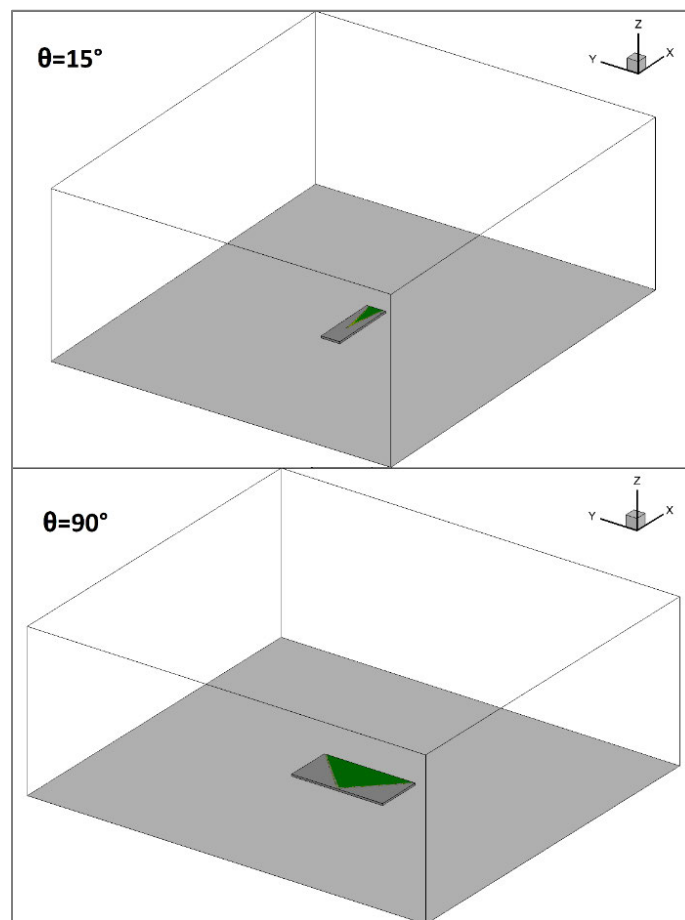


Figure 7.1: Computational domain and vegetation zone for junction angles 15° and 90°.

7.2 Junction Fire Evolution

The overall evolution of the fire front during simulations is addressed using an iso-surface representation of the distribution of dry material for a fixed value of 0.001 kg/m^3 , which is considered representative of the density of material at the fire front (pyrolysis edge). This value is selected to represent the fire edge where the amount of dry material is the smallest, and in direct contact with charcoal. Sample results with all five junction angles are shown in Figure 7.2.

Focusing our attention on the advance of the fire fronts, lateral development can be seen. This is slow compared with the longitudinal progression of the junction point. It is possible to examine the burnt area between two successive fire lines. The overall spread of the fire lines consists of an increase of the angle θ between them. However, the increase in junction angle is not evident in all simulations. With junction angles greater than 45° , simulations exhibit no change in junction angle, especially in the first phase of the simulation, while in the last phase of propagation, the angle generally tends to increase. After all, the irregular propagation of fire fronts and flame jumps at the furthest edge of the vegetation make the estimation of ROS and junction angle difficult. Further explanation of these results is given in the following sections.

In Figure 7.2, the effects of slope and junction angles on the evolution and overall pattern of the fire perimeter can be seen. In order to make best use of the drawn area of the fire perimeter evolution, dimensions are not given in these graphs, so the vertical scale corresponds to the X axis and the horizontal scale to the Y axis in all of them. The units of the values in the scales are always

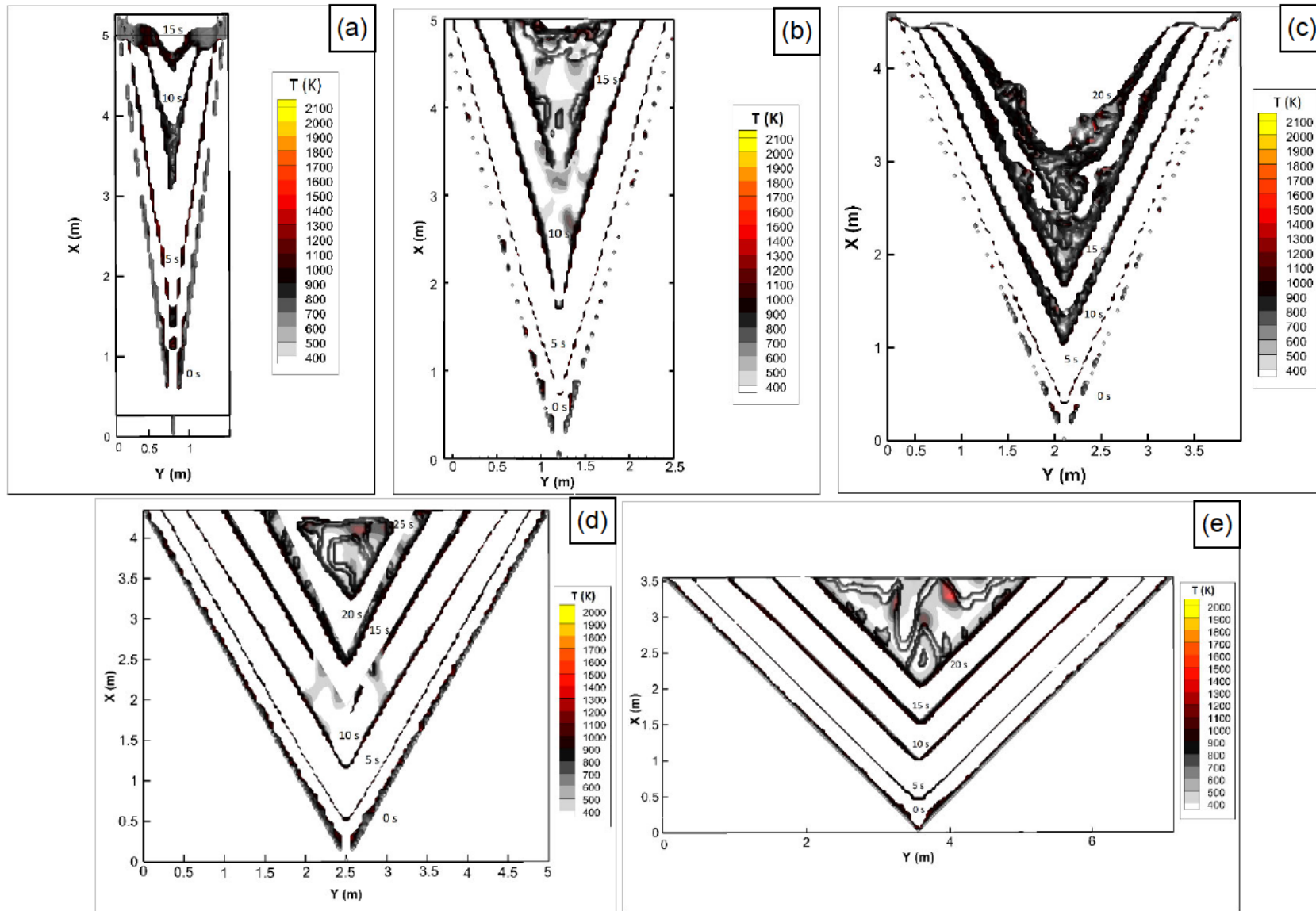


Figure 7.2: Evolution of fire perimeter according to pyrolysis edge (dry material $asps = 0.001 \text{ kg/m}^3$) for cases (a) S1500, (b) S3020, (c) S4500, (d) S6030, and (e) S9040 respectively. The first perimeter (outer) is at $t - t_{\text{ignition}} = 0 \text{ s}$ and the time difference between each perimeter is 5 s (the time corresponding to each perimeter is indicated next to it).

metres. The time corresponding to each perimeter is indicated near of the corresponding line. In the case of the 15° junction angle, strong acceleration is seen (although the slope angle is 0°), along with a significant increase of the junction angle (at $t - t_{\text{ignition}} = 15$ s). However, in the case of the 45° junction angle, a slight deceleration phase is seen for $t - t_{\text{ignition}} > 10$ s. Figures with junction angles of 30° , 60° and 90° and slope angle $>20^\circ$ show only an increase in the front propagation speed. It is also possible to see that the most rapid advance of the fire perimeter occurs progressively for larger distances along the OX axis with increasing value of slope angle. However, for higher junction angles (60° and 90°), propagation appears to be more or less steady.

By analysing the evolution of fire perimeters, it is possible to see that the initial angle between the fire fronts plays an important role, leading to different spread conditions. Keeping the other parameters fixed, it can be seen that for smaller θ angles, fire progresses very rapidly at the intersection zone compared with the lateral spread. As the angle θ increases, the junction point advances less rapidly.

7.3 Fire Front and ROS

The ROS of the junction point is crucial in understanding junction fire behaviour since this is the location where junction fires have their largest effect and the maximum rate of spread is always observed. As mentioned in Chapter 4, the intersection point is tracked inside the vegetation at 5-cm elevation to determine the velocity. In the Appendix, the results using the average method are provided for different simulations with and without wind. In this section, we examine the effect of each parameter separately. Note that some of the junction point position graphs contain vertical parts; these are due to numerical problems in tracking the junction point and they are not included in the calculation of ROS.

7.3.1 Effect of Slope Angle

In order to analyse the role of slope, results for the junction point position and ROS as a function of time t for tests with five values of junction angle θ are shown in Figures 7.3 to 7.7.

Junction Angle 15°

For a junction angle of 15°, the fronts are very close; the maximum distance between them is 1.3 m, as seen in Figure 7.2(a). This could account for the repetitive fire jumps (verticals shown in Figure 7.3(a)). These cases are characterised by very strong interaction between the fire fronts causing this jumping behaviour.

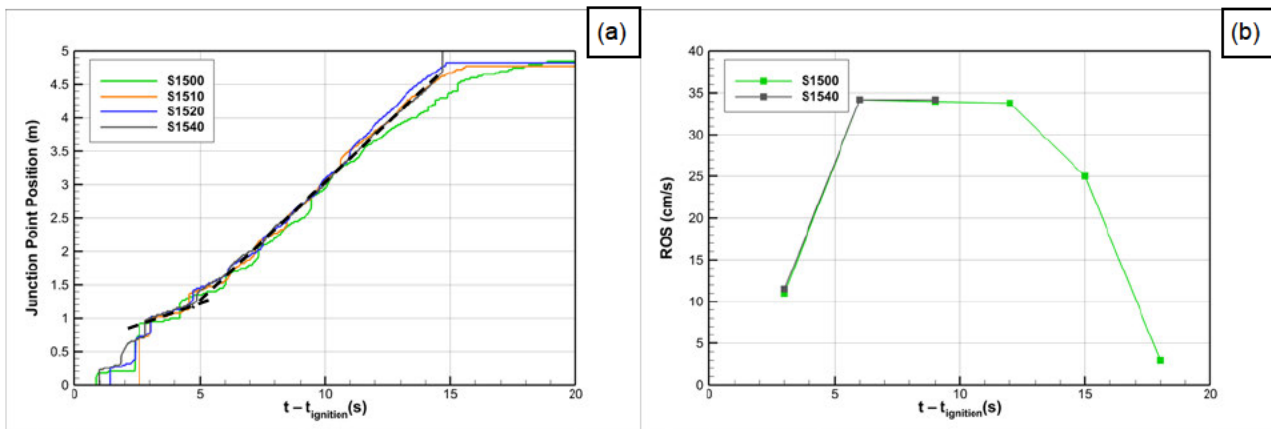


Figure 7.3: (a) Junction point position and (b) evolution of ROS as a function of time for four different slope angles for $\theta = 15^\circ$.

A distinctive characteristic of these is the absence of a fuel-bed slope effect. All curves follow similar patterns and have nearly same slope (they almost merge in Figure 7.3(a)), namely the same ROS. Each curve can be divided in two sections, the first (first interrupted line) with a ROS of 11.5 cm/s, and the second with a ROS of 34.2 cm/s, which is the highest value measured in the entire study.

In the case of slope angle 0° , the junction point shows a deceleration for $t - t_{\text{ignition}} > 12$ s (Figure 7.3(b)). The deceleration in simulation S1500 was large and the minimum ROS_{min} reached 3 cm/s. As seen in Figure 7.2(a), case S1500 exhibits a significant increase in junction angle in the deceleration phase.

Junction angle 30°

Cases with a 30° junction angle were discussed thoroughly in the previous chapter. With this junction angle, simulations were conducted with three slope angles: 0 , 20° and 40° (Figure 7.4). The junction point position demonstrated the same trends for all three slope angles compared with the validation. ROS values were quite close for slopes of 20° and 40° , similarly to previous results; thus, slope angle does not affect results for $\alpha > 20^\circ$. For small slope angles, a large deceleration phase is seen (for $t - t_{\text{ignition}} > 22$ s). It was noted that on a horizontal surface ($\alpha = 0^\circ$), the acceleration phase is short and the deceleration phase is clear. The opposite happens for $\alpha = 30^\circ$, in which the deceleration phase is not evident.

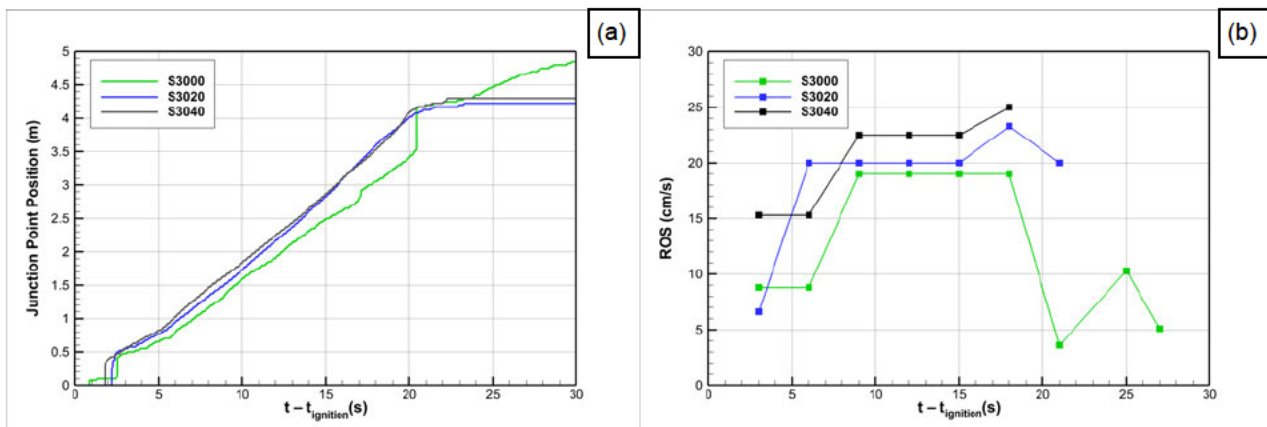


Figure 7.4: (a) Junction point position and (b) evolution of ROS as a function of time for three different slope angles for the case $\theta = 30^\circ$.

Junction angle 45°

This angle appears to be the threshold angle in terms of propagation phases, as the deceleration phase did not appear even in the no-slope case. In this case, the fire propagated steadily for $t - t_{\text{ignition}} > 9$ s. As seen in Figure 7.5, for slope angles 20° and 40°, the ROS appear to be close, consistent with the findings with the lower junction angle.

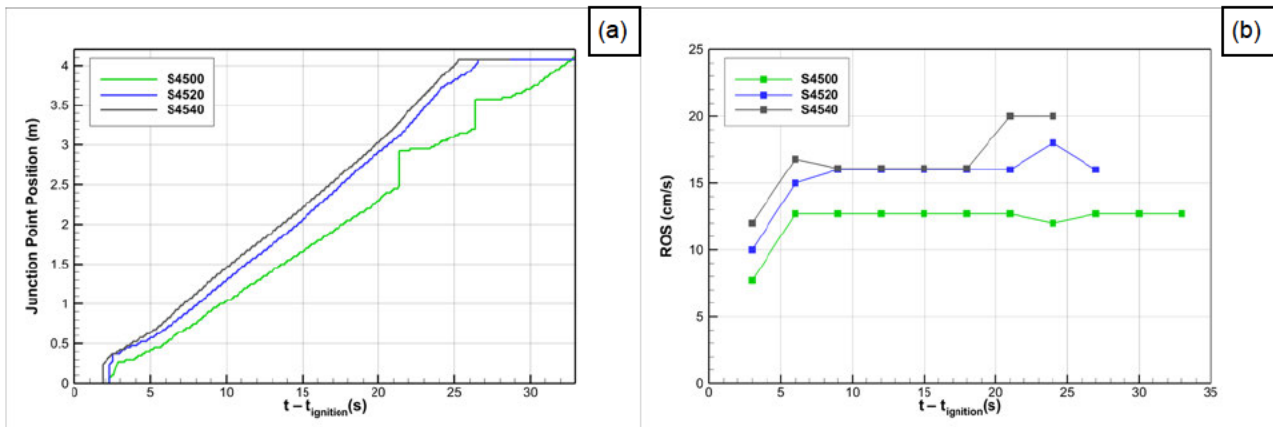


Figure 7.5: (a) Junction point position and (b) evolution of ROS as a function of time for three different slope angles for the case $\theta = 45^\circ$.

Junction angles 60° and 90°

Evolution of the junction point ROS for junction fire with angles of 60° and 90° is given in Figures 7.6 and 7.7. Results show that propagation is systematically influenced by the change of slope angle for these two junction angles. The figures also demonstrate that the propagation only has an acceleration phase. The increase related to the change of slope angle is evident, where with a higher slope angle, the increase in the ROS value is larger. For the lower slope angle, the propagation speed increases, then tends to continue steadily without showing deceleration, unlike for narrower junction angles.

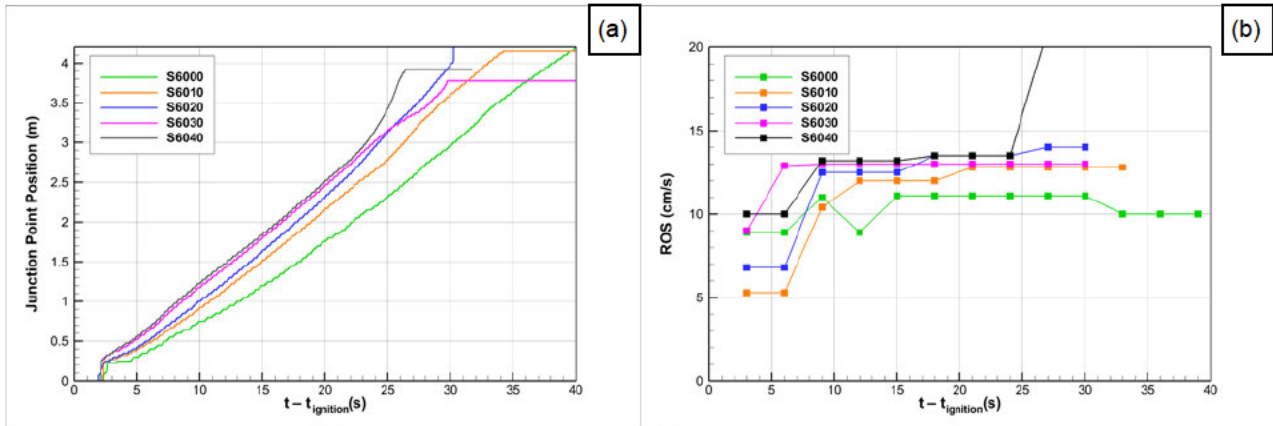


Figure 7.6: (a) Junction point position and (b) evolution of ROS as a function of time for five different slope angles for the case $\theta = 60^\circ$.

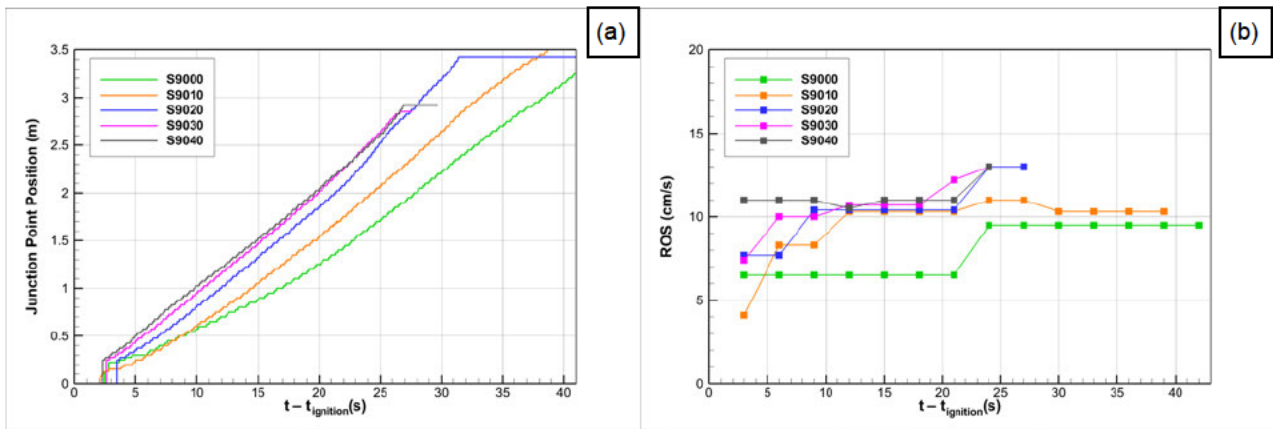


Figure 7.7: (a) Junction point position, and (b) evolution of ROS as a function of time for five different slope angles for the case $\theta = 90^\circ$.

7.3.2 Effect of Junction Angle

The junction angle θ is the main parameter that affects the propagation of junction fire as it controls the level of interaction between the fire lines. ROS generally increases with a lower θ . Throughout, the change of ROS is larger as the junction angle is reduced; for example, in Figure 7.8(c), for a slope of 40° , decreasing θ by 30° , from 90 to 60° , the increase in ROS was about 2 cm/s, while decreasing it from 60° to 30° , the ROS increased about by 7 cm/s. However, an exception to this is observed in Figure 7.8(a) where the deceleration phase for junction angles of 15° and 30° in no-slope conditions are shown. Great similarity was found across all simulations between $\alpha = 20^\circ$ and 40° (Figure 7.8(b))

and (c)). Overall, for junction angles bigger than 45° , junction point propagation was steady.

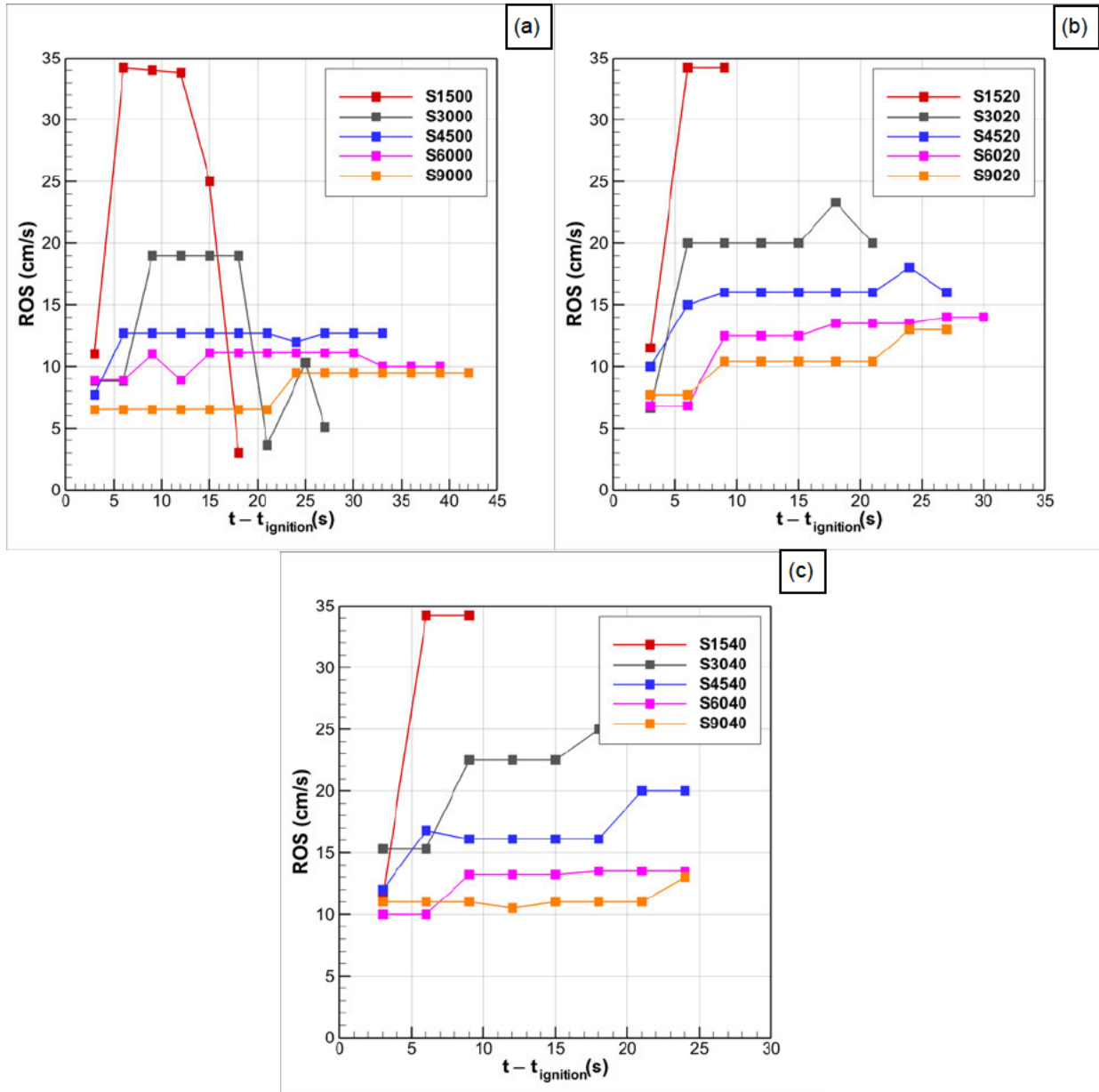


Figure 7.8: Evolution of ROS for four different junction angles and (a) $\alpha = 0$, (b) 20° and (c) 40° as a function of time.

7.4 Heat Transfer Mode

The mode of heat transfer is presented using power density, which is the net amount of energy received or emitted by the total amount of vegetation. In the case of positive power density, the fuel receives more energy than emits (is heated) and in the opposite case, the fuel emits more than receives (it cools). This energy can be either radiative or convective, plays a significant role in the propagation behaviour and is important in understanding the behaviour of junction fire. For convenience, we only examine the extreme cases of $\alpha = 0^\circ$ and 40° .

As seen in Figure 7.9, the vegetation received more energy through convection in the first phase of propagation; however, convective power density decreased over time (green and blue lines except for $\theta = 90^\circ$). Nevertheless, for the horizontal fuel bed, at $t - t_{\text{ignition}} = 8$ s, the fuel lost energy more by convection (green lines except for $\theta = 90^\circ$).

Radiative transfer is more intense for $\alpha = 0^\circ$ (despite strong convection at the beginning, at $t - t_{\text{ignition}} = 8$ s, the fuel lost energy more by convection), while for higher slope angles, the fuel received more by convection for the entire simulations (blue and orange lines).

In Figure 7.9(a), the difference between the radiation densities or convection densities for the two slope angles is small for the entire simulation. In the case of convection, the distance between the blue and green line is approximately constant at around 40 kW/m^3 , while for radiation, it is dropping during the simulation from a difference of 100 kW/m^3 at $t - t_{\text{ignition}} = 6$ s to 60 kW/m^3 at $t - t_{\text{ignition}} = 12$ s. These relatively small differences between the two extreme slope angles could account for the overall close ROS for $\theta = 15^\circ$ (Figure 7.3).

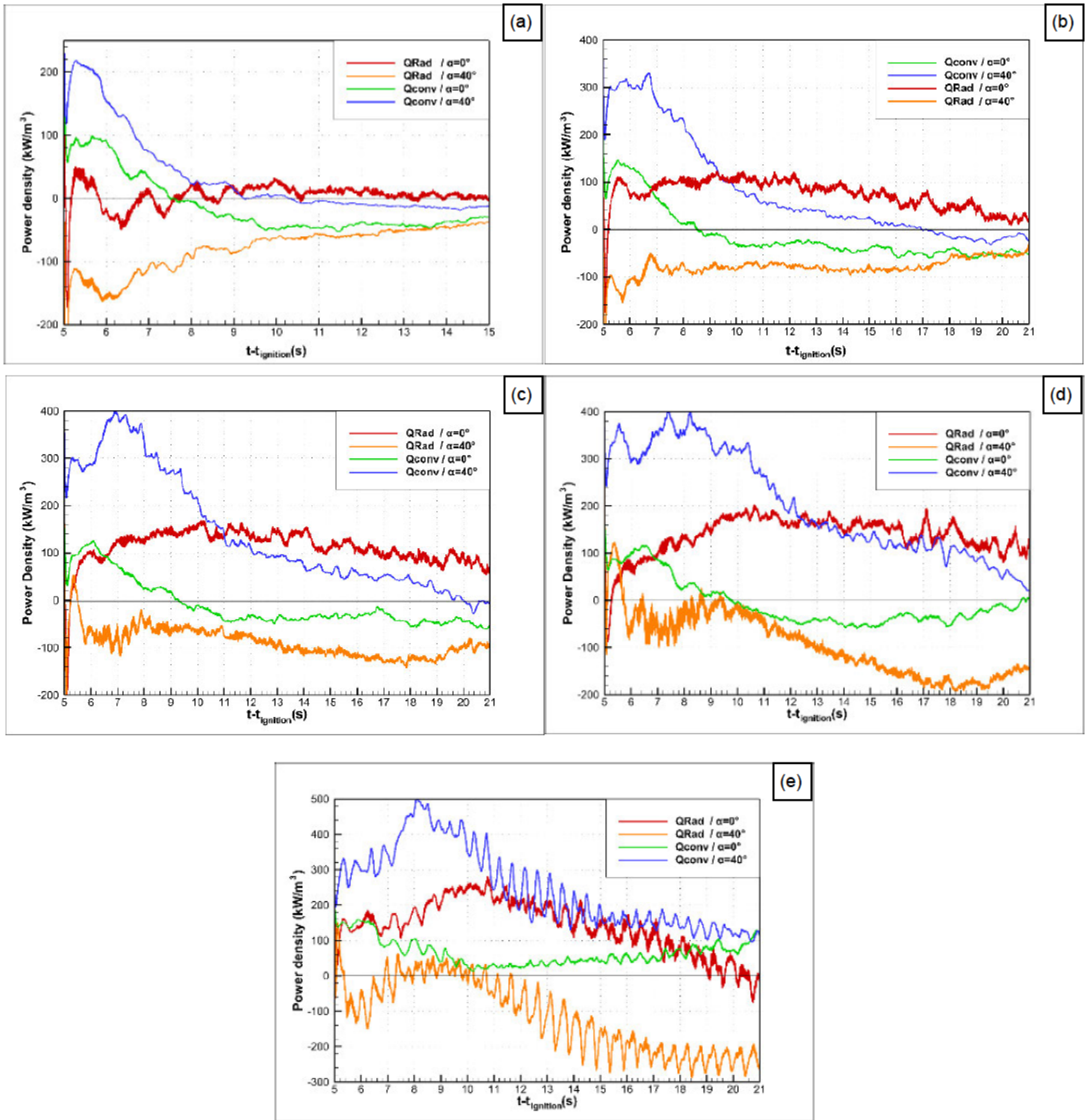


Figure 7.9: Power density received by the solid fuel by convection from the gas mixture and by radiation, in the case of slope angles 0 and 40°, for the five junction angles (a) 15°, (b) 30°, (c) 45°, (d) 60°, and (e) 90°.

7.5 Heat Release Rate

The heat release rate (HRR) of a fire is indicative of the size of that fire. It is the energy released from the vegetation during fire per unit time, or the rate at which the combustion reactions produce heat. The heat release rate is among the most important parameters for understanding fire behaviour [72].

Figure 7.10 represents the HRR for the five studied junction angles. The maximum HRR value for each junction angle usually occurred in the case with the highest slope angle (40°); however, the trend in HRR did not appear to be much influenced by slope angle. It was noted that usually the maximum HRR was higher for a wider junction angle. This may be related to a slower ROS and greater fire residence time. HRR_{max} increases with junction angle increase (see Table 7.2).

Table 7.2: Maximum value of heat release rate (HRR) for different junction angles.

Junction angle (°)	Maximum HRR (MW)
15	2.5
30	3
45	3.3
60	3.5
90	4

For junction angles of 15° and 30° (Figure 7.10(a) and (b)), the HRR reached its maximum value during the first 7 s, then decreased sharply, reflecting the accelerating

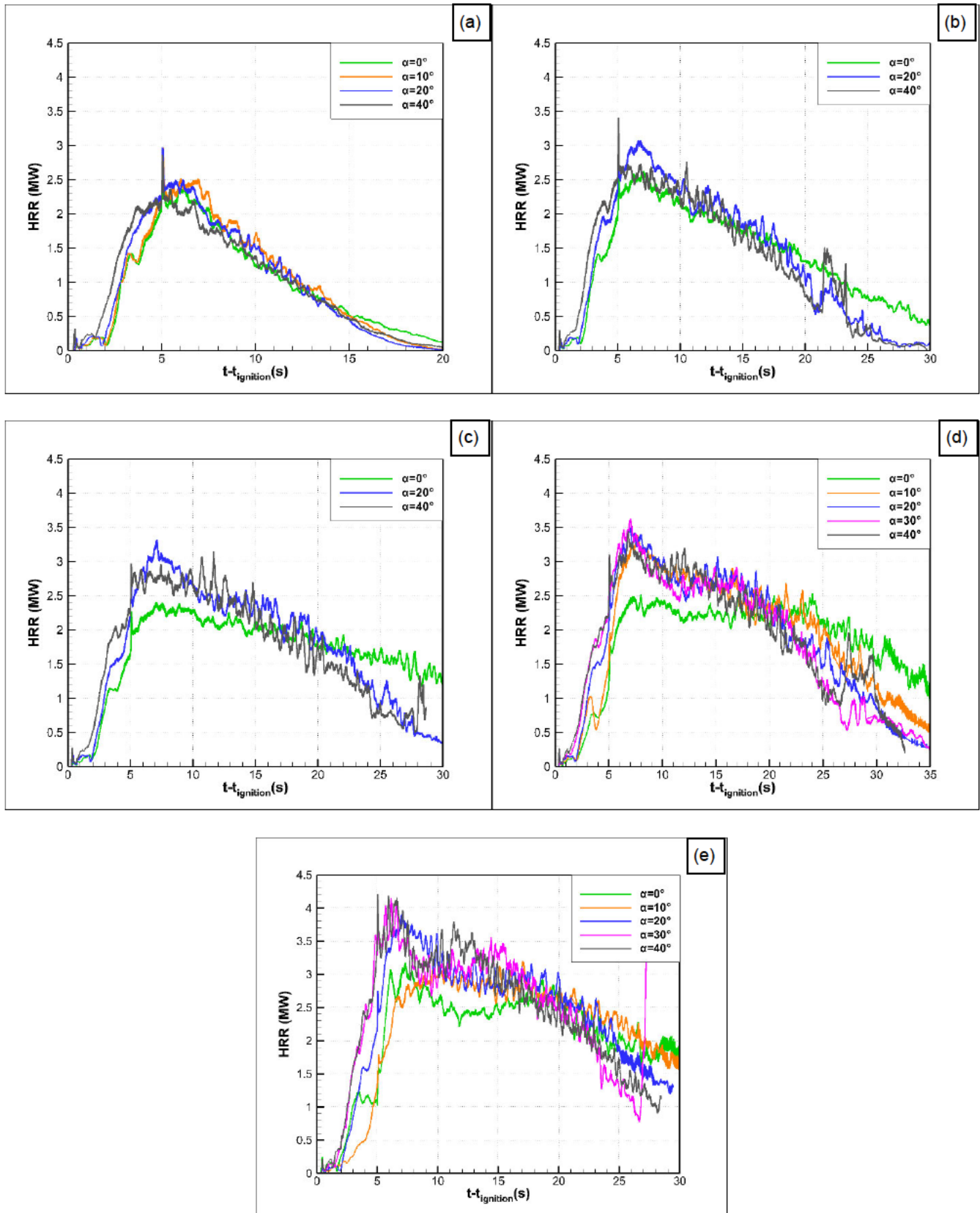


Figure 7.10: Time evolution of the heat release rate (HRR) of the fire obtained from the rate of total mass loss evaluated for the whole solid-fuel layer with different slope angles for cases simulated with junction angles of (a) 15°, (b) 30°, (c) 45°, (d) 60°, and (e) 90°.

behaviour of the fire, but for the case with 0 slope angle (Figure 7.10(b), the HRR decreased relatively slowly, reflecting the reduction of ROS in that case (deceleration phase).

For the remaining junction angles, the HRR, after a decrease from the maximum value, fluctuated more or less steadily around a certain value (a quasi-steady phase up to ~20 s), then decreased gradually. A slower decrease for smaller slope angles was observed (Figure 7.10(c), (d) and (e)). We expected such behaviour owing to the almost steady propagation (only slight initial acceleration) of the junction point for junction angles more than or equal to 45°.

Chapter 8 : Parametric Study – Junction Fire with Wind

8.1 Configuration Description and Numerical Parameters

In this chapter, we add the wind speed variable to the junction fire configuration to examine fire behaviour in low and intermediate wind conditions. The simulated cases are tabulated in Table 8.1, showing the wind speeds adopted in each case. The following notation is used in this section: simulation S1520V1 refers to $\theta = 15^\circ$, $\alpha = 20^\circ$ and $U = 1$ m/s.

Table 8.1: Wind speeds (m/s) used in parametric study for different angles of slope (α) and junction fire (θ).

α (θ)	15°	30°	60°	90°
0°	1, 2, 4	2, 4	2, 4	2, 4
10°	1, 2, 4	–	–	–
20°	4	2, 4	2, 4	2, 4
40°	1, 2, 4	2, 4	2, 4	2, 4

The parametric study focused on the influence of 1-m open wind speed (i.e. wind speed 1 m above the junction point prior to ignition) on fire behaviour in terms of ROS, HRR and modes of heat transfer. The simulations were carried out for three values of the 1-m open wind speed: 1, 2 and 4 m/s, parallel to the longitudinal X axis.

In FIRESTAR3D, wind can be implemented through two methods: a pressure gradient and an imposed wind velocity profile. The pressure gradient method maintains wind

velocity constant at a specified point (usually a point where wind is not perturbed by the presence of fire) and allows the code to determine the velocity profile.

The traditional method – the so-called imposed wind velocity profile (also known as ‘wall of wind’) – applies a constant velocity at the inlet of the computational domain. In our case, the velocity was maintained constant at point ($X = 0$, $Y = 14.5$ m, $Z = 1$ m) using the artificial pressure gradient method (see Figure 4.5).

8.2 Streamlines

Junction fire propagation under a driving wind is illustrated in Figures 8.1 and 8.2, showing the flame temperature and the streamlines of the flow fields in the vertical median plane (XZ plane along the centre of the domain). For no-wind cases, we note that fresh air is entrained from the vicinity of the fire front, supplying the thermal plume. The streamlines in Figure 8.1(a) and (c) and in Figure 8.2(a) and (c) show clearly the existence of aspiration regions ahead of the fire front with and without slope conditions. We see that the fire front in the vertical median plane creates a barrier preventing flow of the gas mixture towards the inlet. In stronger wind conditions, the structure of the air flow is less affected by the fire front, as shown in Figure 8.1(b) and (d) and in Figure 8.2(b) and (d); this effect is limited to local acceleration of the flow. We note the clear tilt of the flame in the wind direction. It can be noticed a very high scale of turbulence above the flame zone. The interactions of fire fronts lead to intense turbulence production in and around the fire front. The production of the turbulence at the surface near the fire front was caused by increased variance of the ambient wind, while the buoyancy was strongest at higher levels within the fire plume.

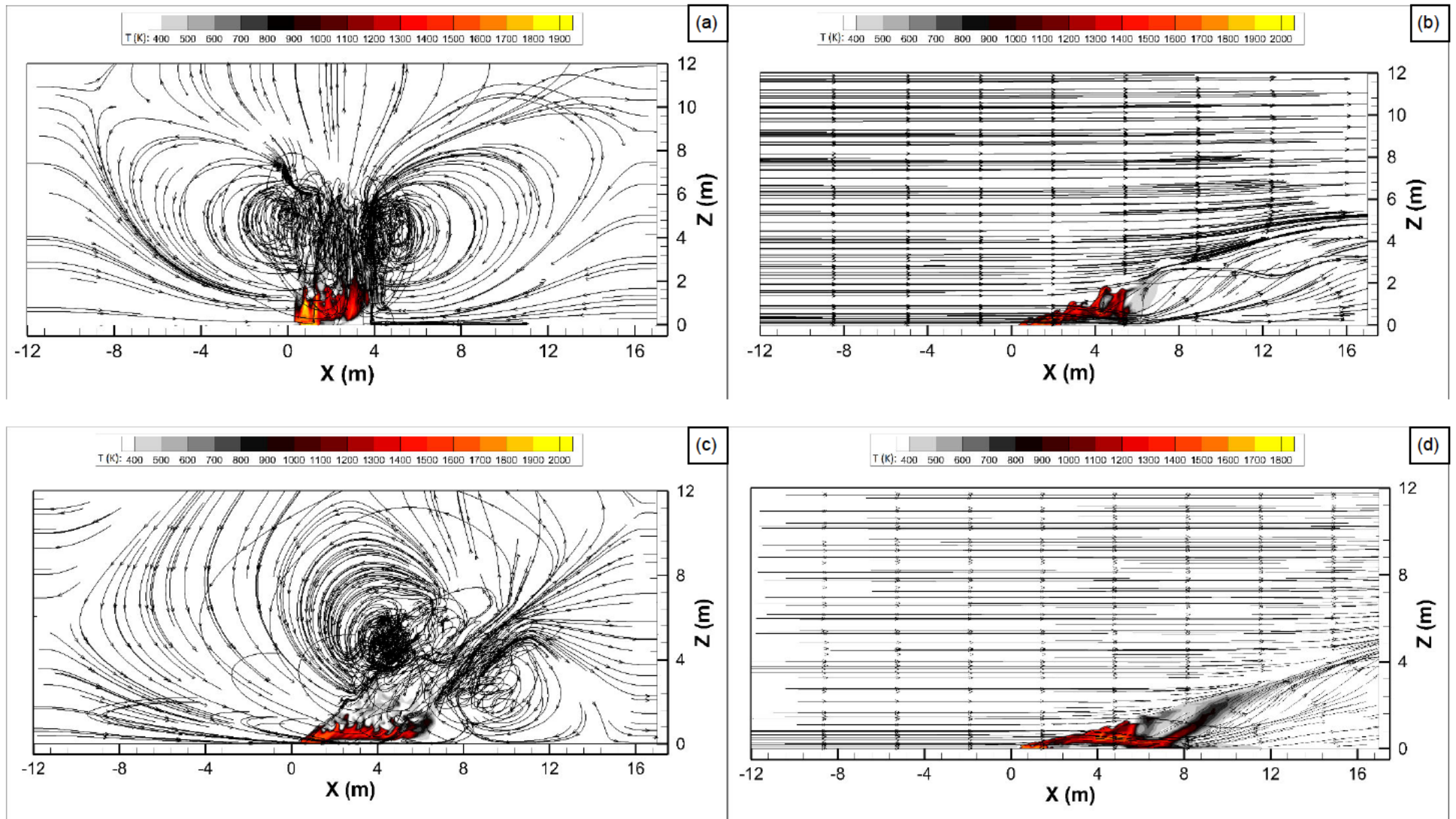


Figure 8.1: Temperature fields and streamlines of the gaseous phase obtained numerically at $t - t_{\text{ignition}} = 6$ s in the vertical median plane for junction angle $\theta = 15^\circ$, and (a) $\alpha = 0^\circ$, $U = 0$ m/s; (b) $\alpha = 0^\circ$, $U = 4$ m/s; (c) $\alpha = 40^\circ$, $U = 0$ m/s; and (d) $\alpha = 40^\circ$, $U = 4$ m/s.

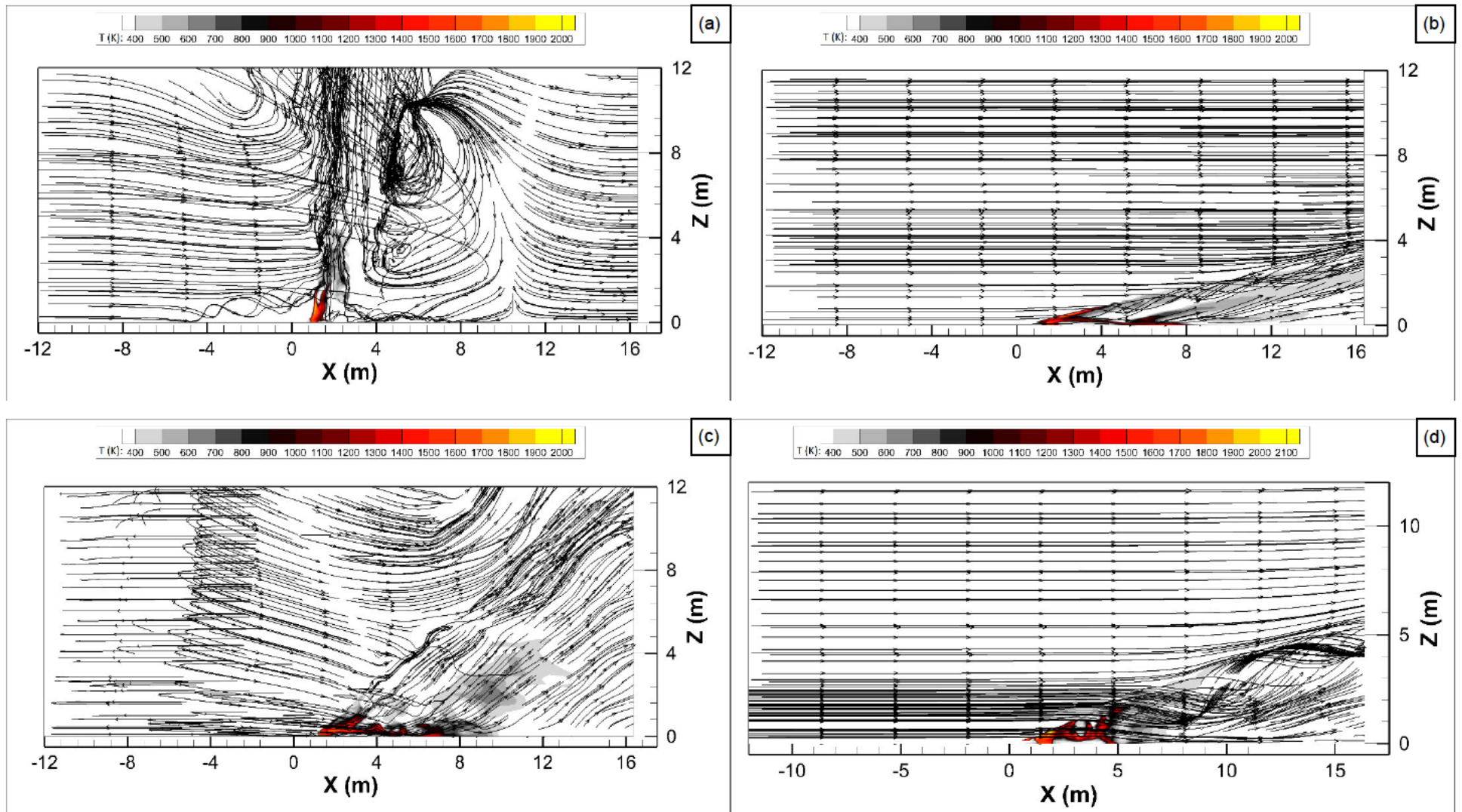


Figure 8.2: Temperature fields and streamlines of the gaseous phase obtained numerically at $t - t_{\text{ignition}} = 15$ s in the vertical median plane for junction angle $\theta = 60^\circ$, and (a) $\alpha = 0^\circ$, $U = 0$ m/s; (b) $\alpha = 0^\circ$, $U = 4$ m/s; (c) $\alpha = 40^\circ$, $U = 0$ m/s; and (d) $\alpha = 40^\circ$, $U = 4$ m/s.

8.3 Fire Front and ROS

Results in the left-hand columns of Figures 8.3, 8.4, 8.5 and 8.6 represent the junction point position, highlighting the nominal value of ROS (the value that lasts for the longest time and dominates in the simulation) along with the evolution of ROS over time. The nominal value of ROS is representative of the dominant junction point propagation speed (roughly averaging the spikes and sudden variations in ROS due to the dynamic effect of wind). We assumed that the variation in the nominal ROS lies between 1 and 2 cm/s. Taking the derivative of junction point positions, we obtained dynamic ROS variation as a function of time, shown in the Appendix, and we then obtained the dynamic-averaged ROS for each simulation case.

The black lines in the left-hand column of Figures 8.3, 8.4, 8.5 and 8.6 represent the nominal ROS in each case. For a junction angle of 15° (Figure 8.3 left), the propagation speeds are identical, as seen from the inclination of the black lines. The maximum ROS of 34.5 cm/s is the highest among all cases and approximately the same for all simulations with a junction angle of 15° . The ROS of the special case of the junction fire with $\theta = 15^\circ$ appeared to be uninfluenced by any external parameters (neither slope nor wind speed) owing to strong interaction between the close fire lines.

For $\theta = 30^\circ$ (Figure 8.4 left), variation of the nominal ROS due to wind speed change was seen. For no slope, the ROS increased by 5 cm/s when driving wind speed rose from 2 to 4 m/s; however, this increase was smaller (1 cm/s) when driving wind speed rose from 0 to 2 m/s. Such behaviour with the change of wind speed was similar for all

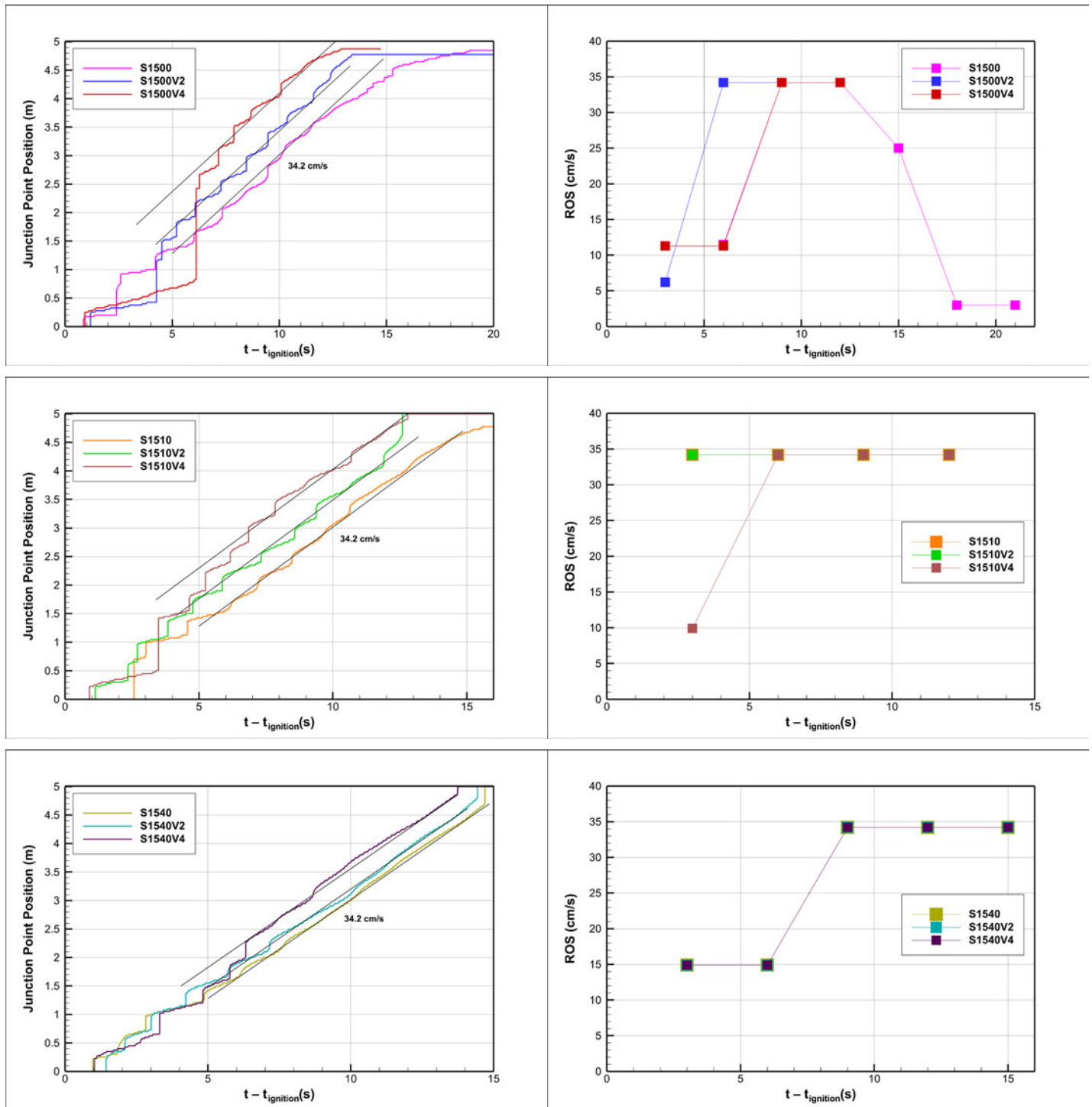


Figure 8.3: Junction point position (left-hand column) and evolution of ROS (right-hand column) as a function of time for three different slope angles for $\theta = 15^\circ$.

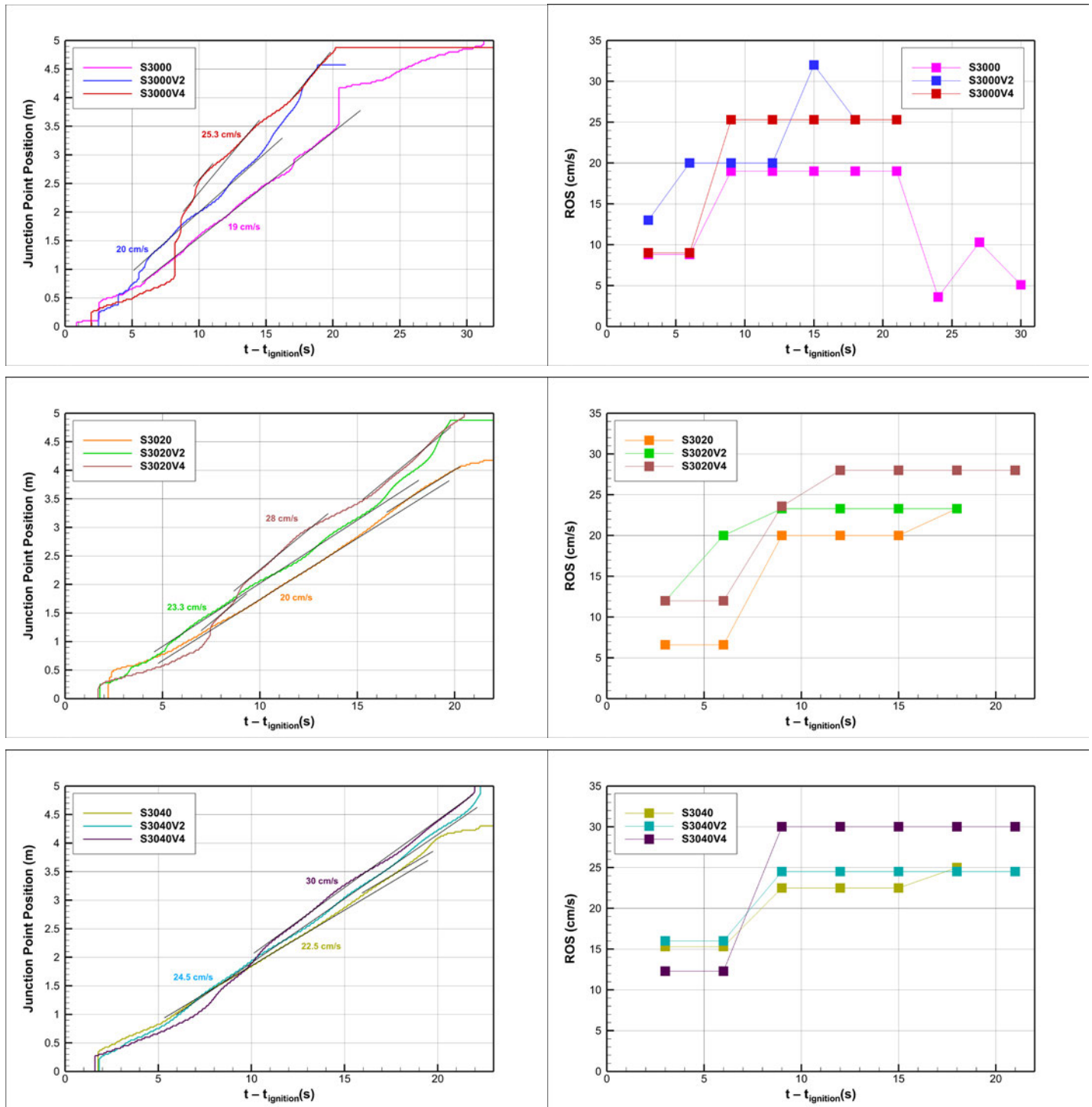


Figure 8.4: Junction point position (left-hand column) and evolution of ROS (right-hand column) as a function of time for three different slope angles for $\theta = 30^\circ$.

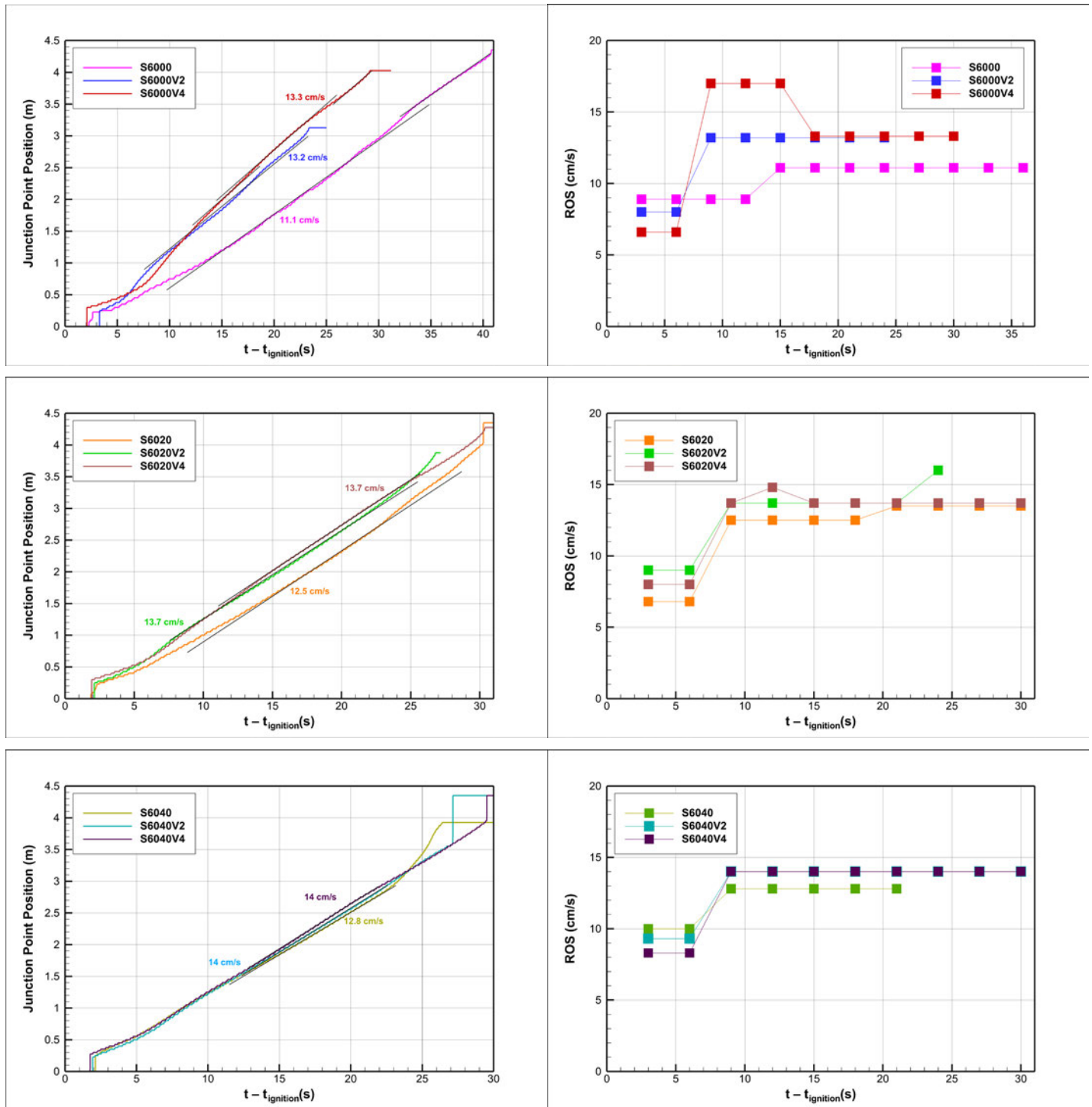


Figure 8.5: Junction point position (left-hand column) and evolution of ROS (right-hand column) as a function of time for three different slope angles for $\theta = 60^\circ$.

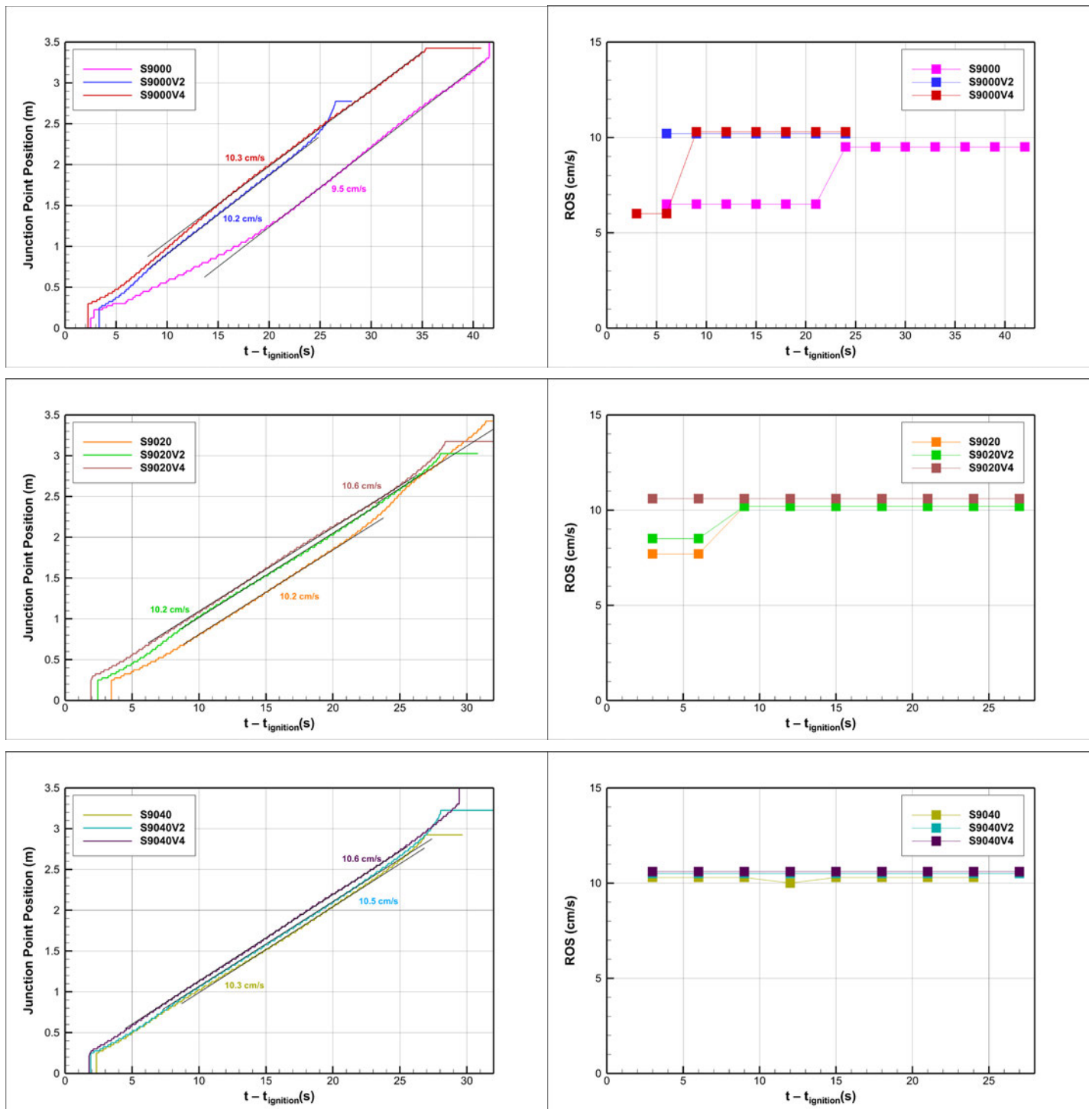


Figure 8.6: Junction point position (left-hand column) and evolution of ROS (right-hand column) as a function of time for three different slope angles for $\theta = 90^\circ$.

$\theta = 30^\circ$ cases. We believe that strong interaction between the fire fronts with the moderate wind speed (4 m/s) is the reason behind the non-linear relationship.

The speed of junction point propagation appeared to be less influenced by wind speed for junction angles 60° and 90° . For $\theta = 60^\circ$, the increase of wind speed from 2 to 4 m/s did not significantly influence the ROS. However, the initial fire establishment period showed variation in the junction point propagation. For 0 and 20° slope with no wind, fire took a longer time to become established (i.e. reach the main ROS value). The simulations with $\theta = 90^\circ$ show a very slight change due to wind, regardless of slope angle (Figure 8.6). Once again, fire establishment takes longer for 0 and 20° slope with no wind velocity.

Figure 8.7 shows the combined results for the main simulations of junction fire with wind. In agreement with previous findings, the junction angle played the most significant role in the ROS of the junction point for driving wind speeds up to 4 m/s. The nominal ROS is more sensitive to change in the lower junction angle range; for instance, nominal ROS decreased about 14 cm/s when θ changed from 15° to 30° , while it dropped approximately 4 cm/s when θ changed from 60° to 90° ($\alpha = 20^\circ$, second vertical column (green) in Figure 8.7).

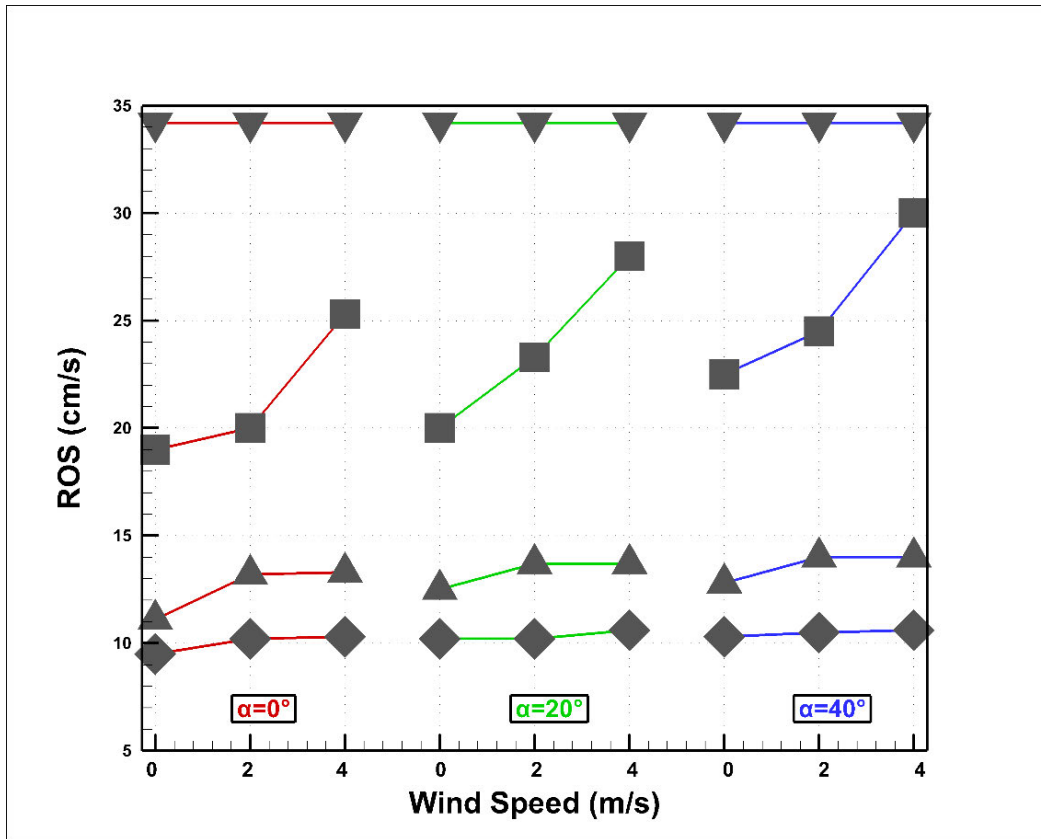


Figure 8.7: Evolution of the nominal ROS for three slope angles: 0° (red), 20° (green), and 40° (blue), showing the effect of wind and junction angle ($\theta = 15^\circ$, ▼; $\theta = 30^\circ$, ■; $\theta = 60^\circ$, ▲; and $\theta = 90^\circ$ ◆).

Figure 8.7 demonstrates that the effect of slope was slight for high junction angles, while for $\theta = 30^\circ$, the wind appeared to be the dominant factor for ROS. The 15° junction angle is a special case where the strong interaction between fire lines controls the propagation rather than any other geometrical or atmospheric factors.

8.4 Heat Transfer Mode

The power density in terms of radiation and convection is presented for different junction angles in Figure 8.8. In case S1500V4, the vegetation received energy through convection for $t - t_{\text{ignition}} < 6$ s, while it was cooled by radiation for the entire simulation (orange line in Figure 8.8(a)). However, both radiation and convection seemed to follow

a similar pattern for $t - t_{\text{ignition}} > 7$ s, unlike the case without wind where radiation was relatively dominant (comparing it with convection, which was negative for the entire simulation).

For a 40° slope angle (case 1540V4), both radiation and convection followed a similar pattern for the entire simulation time. Such behaviour can account for the similarity of ROS for different simulations with $\theta = 15^\circ$ (Figure 8.8(b)). In both cases, with and without slope, the power density ranged between $+10$ and -50 kW/m³ for $t - t_{\text{ignition}} > 10$ s, when the ROS was reaching its maximum value (34.2 m/s in Figure 8.3).

The effect of wind is observed from the relative reduction of radiative heat transfer for all simulations with no-slope conditions (comparing orange and red lines in the left-hand column of Figure 8.8). This reduction is compensated by an increase in convection for junction angles 60° and 90° (black and blue lines in Figure 8.8(e) and (g)) and could explain the minimal changes in ROS for these two junction angles (Figures 8.5 and 8.6).

However, in cases S3000 and S3000V4, the amounts of convective heat transfer are almost identical (Figure 8.8(c)). In the case of junction angle 30° , we saw the highest increase of ROS as an effect of wind (Figure 8.7). Further investigation into the relationship between heat transfer modes and ROS in the special case of $\theta = 30^\circ$ must be done.

In high slope conditions (right-hand column of Figure 8.8), the power densities follow an almost identical trend for the different cases. Both convection and radiation curves are quite close; the effect of wind speed is insignificant. This is not the case for simulations

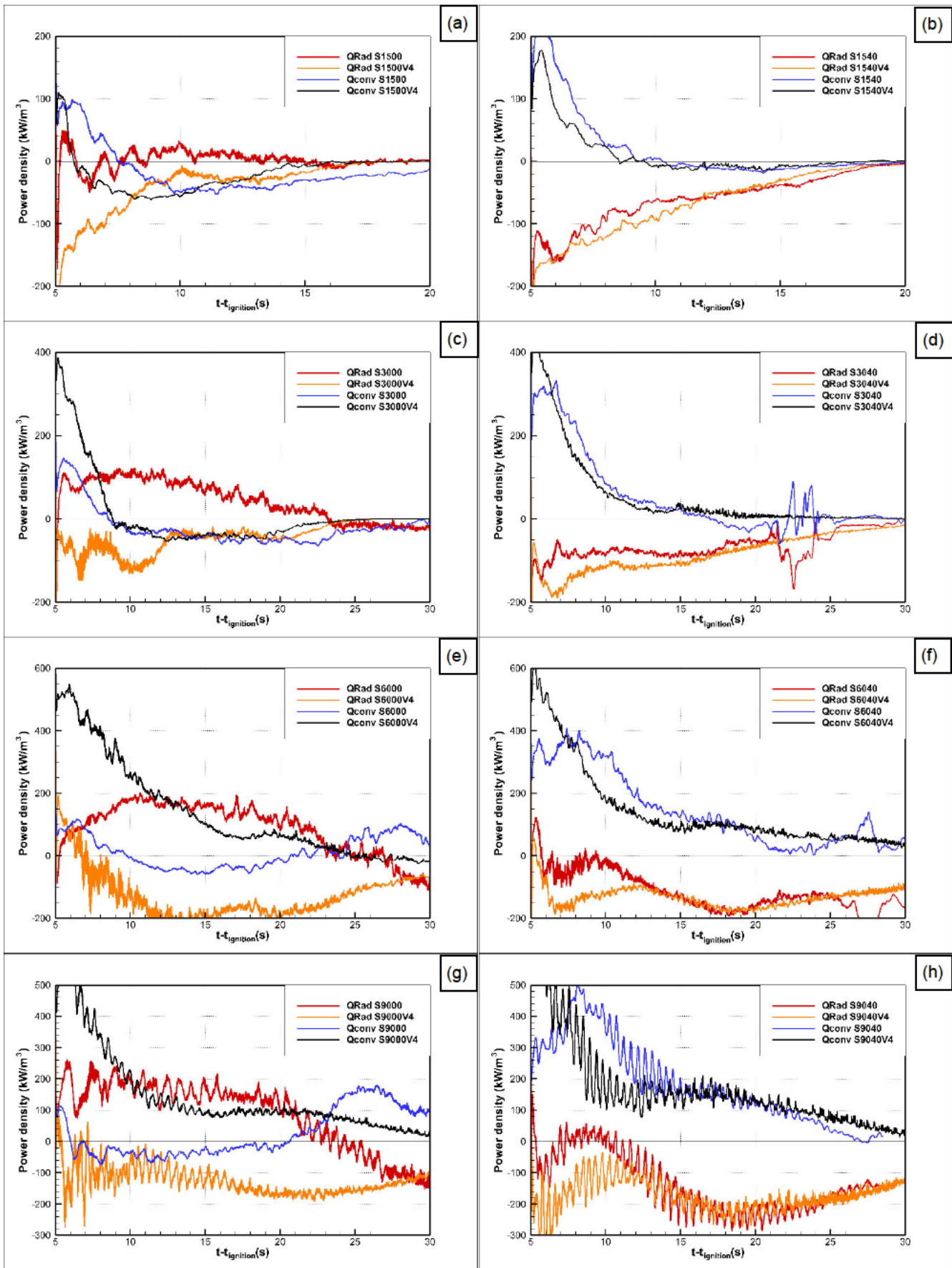


Figure 8.8: Power density received by the solid fuel by convection and radiation for two wind speeds (0 and 4 m/s) in cases: (a) S1500, (b) S1540, (c) S3000, (d) S3040, (e) S6000, (f) S6040, (g) S9000, and (h) S9040.

with no slope (discussed previously). This could be attributed to significant convective flow in high-slope cases, which may be comparable with the imposed wind speed. Appropriately, convection dominates in all cases with high slopes; fuel heated by convection (comparing black and orange lines in all right-hand columns of Figure 8.8) and the vegetation lose energy by radiation for the entire simulation time.

The results in Figure 8.8 provide interesting information about possible relationships between the mode of heat transfer and junction fire behaviour. For the cases with no slope, the change in the modes of heat transfer was irregular, and we found an increase in convection angle for higher junction angles. Still, radiation decreased for all simulations as an effect of wind. In high terrain slope cases, convection and radiation were almost unchanged. The comparison between the fire-induced wind (the fire's own wind) and the imposed wind speed is interesting, especially for higher slope cases, but limited at this step as it is difficult to determine its value (owing to the existence of many vortices and highly turbulent flow).

8.5 Heat Release Rate

As an effect of wind, the maximum value of HRR increased significantly in cases without slope (see the difference between orange and red lines in Figure 8.9). However, for higher slopes, such an effect was not clearly seen (blue and green lines), and the overall HRR curves appeared to have a higher peak value for cases with wind (green lines).

In the case of junction angle 90° , the maximum heat was released for the highest slope and highest wind speed case (green line). For 15° , 30° and 60° junction angles, green and blue lines lie between orange and red lines. In Figure 8.9(a), approximately 1 MW

HRR difference is observed between no-wind and 4 m/s wind velocity simulations for no-slope conditions. A relatively faster decrease in HRR is seen in cases simulated with wind for zero slope cases. For this limited range of wind speeds, the slope angle appears to be the main parameter governing the relationship between HRR (fire intensity) and wind speed.

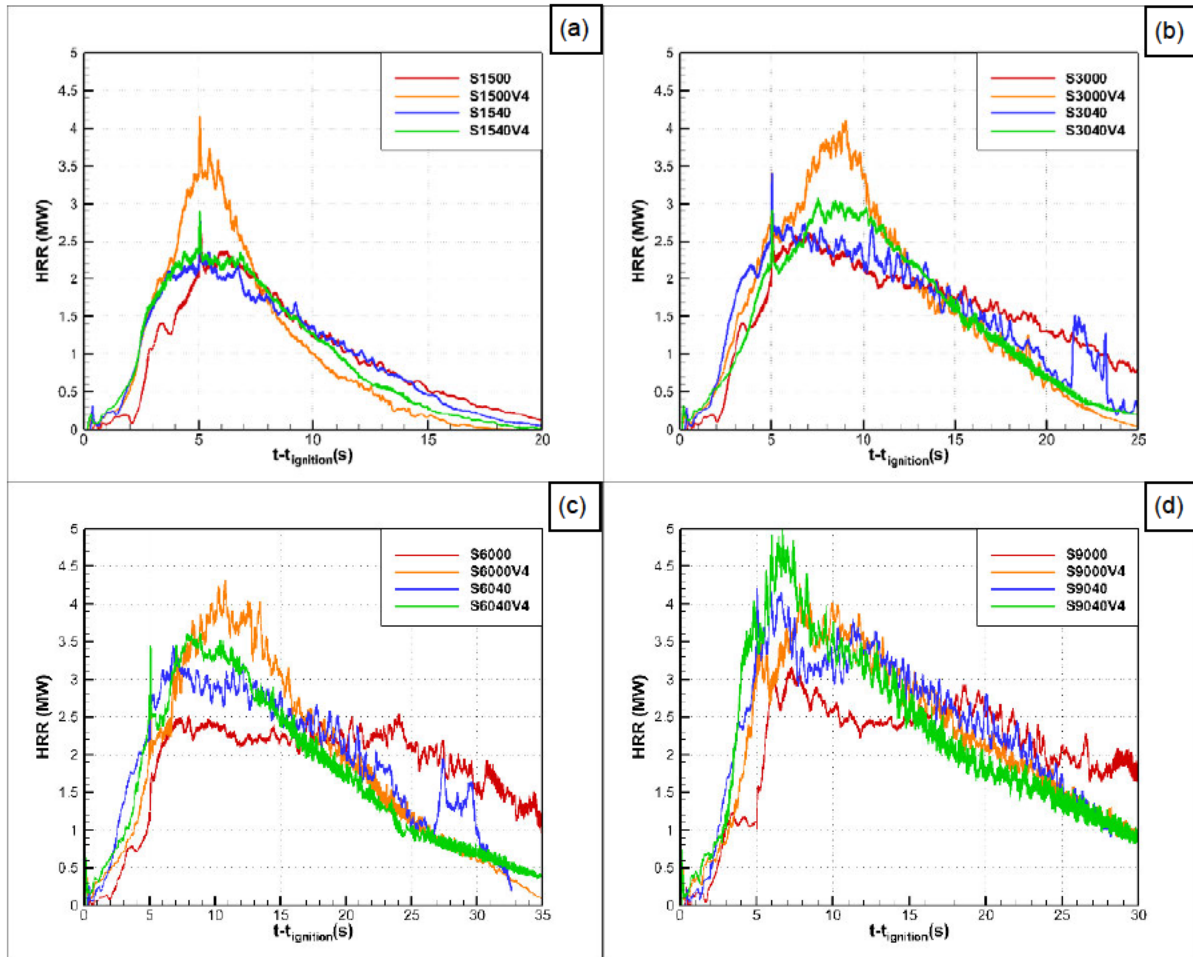


Figure 8.9: Time evolution of the heat release rate (HRR) obtained from the rate of total mass-loss evaluated for the whole solid-fuel layer with two slope angles (0 and 40°) in cases simulated with junction angles (a) 15°, (b) 30°, (c) 60°, and (d) 90° without wind and with wind speed $U = 4$ m/s.

Chapter 9 : Conclusion

9.1 Discussion

The parametric study starts from a case of complex model to allow the exploration of more fundamental processes which might lead to extreme spread rates in junction fires. The main parameters slope, junction angle and wind were extensively examined over a wide range. For a very small junction angle, the huge interaction between the fronts takes control over the fire behaviour as no significant change due to the increasing slope and driving-wind speed has been noticed (see fig. 7.3 and 8.3). The only exception was the existence of a deceleration phase in the non-slope case. The increase of junction angle during the propagation (see Fig. 7.2 a) may be the reason for this slowing; nevertheless, the existence of a slight slope angle (10°) or small wind speed (2m/s) removes totally this deceleration and maintains a constant junction angle during the propagation.

In the specific case of a junction angle of 30° , the effects of the other parameters normally existed (acceleration and deceleration phases), but for higher junction angles, no deceleration was found.

According to these results, we can select the value $\theta = 45^\circ$ as the threshold angle where no changes in the propagation phases were noticed and a steadier behaviour was seen. Similarly for the cases with wind, where the accelerating effect of the wind was less impactful for wider junction angles. The large scale of turbulence above the flame (fig. 8.1 and 8.2) has an important role in creating a full or partial barrier to the wind.

Taking into account the dominant mode of heat transfer, the main feature was the switching between radiation-dominant fire and convection-dominant fire as a function of the slope angle. Such change was not surprising and may be acceptable as demonstrated by Dupuy et al. [73]. Oppositely, the application wind was having less impact on higher slope cases. Such results require further investigations in future works.

Finally, the HRR trend was changing with the change of junction angle, where wider-junction-angle fires release more heat. For the simulations with wind, the effect was more complicated and requires further investigation.

9.2 Conclusion

The modelling of junction fire using a physics-based model to describe the behaviour of two fire fronts that intersect and merge is reported in this thesis. The simulations were conducted at a laboratory scale. Physics-based simulations solve pertinent physical and chemical equations to predict fire behaviour and intensity. FIRESTAR3D includes a multiphase formulation in which it solves equations that govern the behaviour of the coupled system formed by the fire, the vegetation and the surrounding atmosphere inside elementary control volumes including both the solid phase (the vegetation) and the gaseous phase. The physics-based approach provides the best results when it comes to simulating extreme fire behaviour like junction fires, which is among the most severe and complicated of wildfire phenomena.

A validation study and sensitivity analysis for the numerical model were done by comparing numerical outcomes with experimental results of laboratory-scale junction fire. The laboratory fire experiments were conducted at Coimbra University with shrub with a

low packing ratio as vegetation for a range of slope and junction angles, providing many experimental measurements. The laboratory-scale experiments provided insights into the main phenomena associated with junction fires.

The sensitivity of the numerical model FIRESTAR3D was tested for grid size, domain size and burner parameter and showed that the results are not significantly influenced by these. Atmospheric temperature and humidity ratio slightly affected the results and should be used in the physics-based model in a close range to the experimental conditions. The physical parameters seemed to exert a complicated influence, especially the heat transfer parameters, but overall, ROS was not much affected.

The model reasonably predicted the ROS and the correct experimental trends caused by variation of the junction angle and the slope angle (good qualitative and quantitative agreement). The dynamic behaviour of junction fire, represented by acceleration and deceleration, was shown to be function of the slope angle. The maximum value of ROS was determined in strong relation to the junction angle and in good agreement with experimental measurements (maximum of 5 cm/s difference). Therefore, the model can be used for a wider range of geometrical angles.

A parametric study of the main geometrical parameters that govern junction fire behaviour (slope and junction angles) encompassed a wide range of values. Smaller junction angles (such as 15° and 30°) induced different propagation behaviours (acceleration or deceleration) as a function of slope angle. However, an angle of 45° was found to be the threshold at which no deceleration phase was observed. The ROS for high junction angles accelerated slightly and propagation appeared to be steady. For lower junction

angles, the deceleration phase was only evident for no-slope conditions where the junction angle increased during propagation. The acceleration could be related to the significant initial convective flow. However, the vegetation received more energy through convection than through radiation in steeper slope cases while it lost more heat through convection in no-slope conditions; such behaviour was common for most simulated cases. Considering HRR, the fire released more energy for higher junction angles. The relatively slow ROS in cases with higher junction angles accounts for the higher HRR.

The junction angle greatly affects junction fire behaviour under the influence of a driving wind. For a very narrow junction angle, very strong interactions exist between fire fronts, and ROS did not change with the influence of wind, although variation due to a driving wind was manifest to different degrees for different junction angles. Junction fires with higher junction angles were affected less than with a 30° angle. Under the effect of wind, the fuel lost more energy by radiation in no-slope cases, while no significant change in heat transfer modes was found in cases with higher slopes. In the case with a lower junction angle and lower slope, the maximum heat release rate rose owing to the effect of wind. It was found this maximum was higher in no-slope cases, except with a junction angle of 90°.

This research showed how, as a complement to experimental investigations, detailed physics-based models can help develop an understanding of the basic physical mechanisms governing the behaviour of extreme wildfires. The modelling allowed examination of a greater range of fire experiments (than can be carried out in practice) and provided explanations for some fire behaviour.

More work must be carried out to explore extreme fire phenomena. Many stakeholders have raised questions about the effects of fuel, packing ratio and scale on junction fire propagation.

Modelling junction fire at a greater scale would be challenging and interesting, especially in cases with intermediate and high wind speeds. Thorough investigation of the modes of heat transfer, HRR and fire line intensity can be done by comparing these quantities for both junction fires and single fire lines, which can be implemented easily and effectively when we scale the fire up. Quantifying the fire line intensity of a real large-scale fire, then using Byram's convective number can help in drawing deeper conclusions about the dominant propagation regime for various cases of junction fire.

The investigation of different propagation phases in field-scale fires could provide useful findings for use in operational tools for fighting such extreme fires. The study of interactions between fire fronts could also be done for non-intersecting fire fronts and parallel fire fronts. Modelling multiple fire fronts would also provide useful insights.

References

- [1] E. Pastor, L. Zarate, E. Planas and J. Arnaldos, "Mathematical models and calculation systems for the study of wildland fire behaviour," *Progress in Energy and Combustion Science*, vol. 29(2), pp. 139-153, 2003.
- [2] N. Frangieh, D. Morvan, S. Meradji, G. Accary, O. Bessonov, "Numerical simulation of grassland fires behaviour using an implicit physical multiphase model," *Fire Safety Journal*, vol. 102, pp. 37-47, 2018.
- [3] D. Morvan, G. Accary, S. Meradji, N. Frangieh, O. Bessonov, "A 3D physical model to study the behavior of vegetation fires at laboratory scale," *Advances in Forest Fire Research*, vol. 101, pp. 39-52, October 2018.
- [4] D. Viegas, J. Raposo, D. Damvim and C. Rossa, "Study of the jump fire produced by the interaction of two oblique fire fronts. Part 1. Analytical model and validation with no-slope laboratory experiments.," *International Journal of Wildland Fire*, vol. 21, p. 843–856, 2012.
- [5] S. Lahaye, J. Sharples, S. Matthews, S. Heemstra, O. Price and R. Badlan, "How do weather and terrain contribute to firefighter entrapments in Australia?," *International journal of wildland fire*, vol. 27(2), pp. 85-98, 2018.
- [6] J. Sharples, G. Cary, P. Fox-Hughes, S. Mooney, J. Evans, M. Fletcher, M. Fromm, P. Grierson, R. Mcrae and P. Baker, "Natural hazards in Australia: extreme bushfire," *Climatic Change*, vol. 139(1), p. 85–99, 2016.
- [7] M. Doogan, *The Canberra Fire Storm: Inquests and Inquiry into Four Deaths and Four Fires Between 8 and 18 January 2003*, vol. 1, Canberra: ACT Coroners Court, 2003.
- [8] R. McRae, J. Sharples, S. Wilkes and A. Walker, "An Australian pyro-tornadogenesis event," *Natural Hazards*, vol. 65(3), pp. 1801-1811, 2013.
- [9] J. Raposo, Viegas D, X. Xie, M. Almeida, A. Figueiredo, L. Porto and J. Sharples, "Analysis of the physical processes associated with junction fires at laboratory and field scales," *International Journal of Wildland Fire*, vol. 27(1), p. 52–68, 2018.
- [10] D. Viegas, J. Raposo and A. Figueiredo, "Preliminary analysis of slope and fuel bed effect on jump behavior in forest fires.," *Procedia Engineering*, vol. 62, p. 1032–1039, 2013.

- [11] A. Sullivan, W. Swedosh, R. Hurley, J. Sharples and J. Hilton, "Investigation of the effects of interactions of intersecting oblique fire lines with and without wind in a combustion wind tunnel," *International Journal of Wildland Fire*, vol. 28, p. 704–719, 2019.
- [12] A. Filkov, B. Cirulis, T. Penman, "Quantifying merging fire behaviour phenomena using unmanned aerial vehicle technology," *International Journal of Wildland Fire*, vol. 30, p. 197–214, 2021.
- [13] C. Thomas, J. Sharples and J. Evans, "Modelling the dynamic behaviour of junction fires with a coupled atmosphere–fire model.," *International Journal of Wildland Fire*, vol. 26, p. 331–344, 2017.
- [14] C. Thomas, "Investigation of spotting and intrinsic fire dynamics using a coupled atmosphere-fire modelling framework.," PhD dissertation, University of New South Wales, Canberra, 2019.
- [15] P. Higuera, "Taking time to consider the causes and consequences of large wildfires," *Proceedings of the National Academy of Sciences of the United States of America*, vol. 112(43), pp. 13137-13138, 2015.
- [16] M. Moritz, M. Morais, L. Summerell, J. Carlson and J. Doyle, "Wildfires, complexity, and highly optimized tolerance," *Proc Natl Acad Sci USA*, vol. 102(50), p. 17912–17917, 2005.
- [17] A. Sullivan, "Wildland surface fire spread modelling, 1990–2007. 1: Physical and quasi-physical models," *International Journal of Wildland Fire*, vol. 18, p. 349–368, 2009.
- [18] R. Linn, J. Reisner, J. J. Colman, and J. Winterkamp, "Studying wildfire behavior using FIRETEC," *International Journal of Wildland Fire*, vol. 11, pp. 233-246, 2001.
- [19] W. Mell, M. Jenkins, J. Gould and P. Cheney, "A physics-based approach to modelling grassland fires," *International Journal of Wildland Fire*, vol. 16, pp. 1-22, 2007.
- [20] J. Mandel, J. Beezley, J. Coen and M. Kim, "Data assimilation for wildland fires," *IEEE Control Systems Magazine*, vol. 29, no. 3, pp. 47 - 65, 2009.
- [21] M. Jenkins, T. Clark and J. Coen, Forest Fires: Behavior and Ecological Effects, Chapter 8. :In "Coupling Atmospheric and Fire Models", Elsevier Inc., 2001.
- [22] P. Cheney and A. Sullivan, Grassfires: Fuel, Weather and Fire Behaviour, Melbourne: CSIRO Publishing, 2009.
- [23] N. Cheney, J. Gould and W. Anderson, "Prediction of Fire Spread in Grasslands," *International Journal of Wildland Fire*, vol. 8(1), pp. 1-13, March 1998.

- [24] A. McArthur, Fire behaviour in eucalypt forests, Canberra: Forestry and Timber Bureau, Department of National Development, Leaflet No. 107, 1967.
- [25] J. Fayad, "Junction Fires on Sloped Terrain," Masters Thesis, Lebanese University, Tripoli, 2020.
- [26] J. Raposo, S. Cabiddu, D. Viegas, M. Salis and J. Sharples, "Experimental analysis of fire spread across a two-dimensional ridge under wind conditions," *International journal of wildland fire*, vol. 24(7), pp. 1008-1022, 2015.
- [27] D. Morvan and N. Frangieh, "Wildland fire behaviour: wind effect versus Byram's convective number and consequences on the regime of propagation," *International Journal of Wildland Fire*, vol. 27, p. 636–641, 2018.
- [28] R. Nelson, "Re-analysis of wind and slope effects on flame characteristics of Mediterranean shrub fires," *International Journal of Wildland Fire*, vol. 24(7), p. 1001–1007, 2015.
- [29] P. Pagni and T. Peterson, "Flame spread through porous fuels," *Proceedings of the Combustion Institute*, vol. 14, p. 1099–1107, 1973.
- [30] N. Khan, D. Sutherland, R. Wadhvani and K. Moinuddin, "Physics-based simulation of heat load on structures for improving construction standards for bushfire-prone areas," *Frontiers in Mechanical Engineering* 5, vol. 35, 2019.
- [31] J. Coen, C. Marques, J. Michalakes, E. Patton, P. Riggan and K. Yedinak, "WRF-Fire: coupled weather–wildland fire modeling with the weather research and forecasting model," *Journal of Applied Meteorology and Climatology*, vol. 52, p. 16–38, 2013.
- [32] A. Grishin, Mathematical Modeling of Forest Fires and New Methods of Fighting them, Tomsk: House of the Tomsk State University, 1997.
- [33] D. Morvan, "Physical phenomena and length scales governing the behaviour of wildfires: a case for physical modelling," *Fire Technology*, vol. 47, p. 437–460, 2011.
- [34] D. Morvan, S. Meradji and G. Accary, "Wildfire behavior study in a mediterranean pine stand using a physically based model," *Combust. Sci. Technol.*, vol. 180, p. 230–24, 2008.
- [35] D. Morvan and J. Dupuy, "Modeling the propagation of a wildfire through a Mediterranean shrub using a multiphase formulation," *Combustion and Flame*, vol. 138(3), pp. 199-210, 2004.
- [36] D. Morvan, S. Meragji and G. Accary, "Physical modelling of fire spread in Grasslands," *Fire Safety Journal*, vol. 44, pp. 50-61, 2009.

- [37] A. Gill, R. Groves and I. Noble, *Fire and the Australian Biota*, Canberra: Australian Academy of Science, 1981, p. 151.
- [38] N. Burrows, "Flame residence times and rates of weight loss of eucalypt forest fuel particles," *International Journal of Wildland Fire*, vol. 10, pp. 137-143, 2001.
- [39] C. Blasi, C. Branca, A. Santoro and E. Hernandez, "Pyrolytic behavior and products of some wood varieties," *Combustion and Flame*, vol. 124, pp. 165-177, 2001.
- [40] D. Evans and H. Emmons, "Combustion of wood charcoal," *Fire Safety Journal*, vol. 1(1), pp. 57-66, 1977.
- [41] A. Faver, L. Kovaszny, R. Dumas, J. Gaviglio and M. Coantic, "La turbulence en mecanique des fluides," *Gauthier-Villars*, 1976.
- [42] Y. Horibata, "Numerical simulation of a low-mach-number flow with a large temperature variation," *Computers and fluids*, vol. 21(2), pp. 185-200, 1992.
- [43] S. Paolucci, "Filtering of sound from the Navier-Stokes equations," Sandia National Laboratories Livermore, CA, USA, 1982.
- [44] R. Kee, F. Rupley and J. Miller, "The chemkin thermodynamic data base," Sandia National Lab., United States, 1990.
- [45] C. Kaplan, C. Shaddix and K. Smyth, "Computations of enhanced soot production in time-varying CH₄/air diffusion flames," *Combustion and Flame*, vol. 106 (4), pp. 392-405, 1996.
- [46] G. Cox, *Combustion Fundamentals of Fire*, Academic Press, 1995.
- [47] G. Katul, L. Mahrt, D. Poggi and C. Sanz, "One-and two-equation models for canopy turbulence," *Boundary-Layer Meteorology*, vol. 113(1), pp. 81-109, 2004.
- [48] B. Magnussen and H. Hjertager, "On mathematical modeling of turbulent diffusion flame in cross flow," *Combustion Science and Technology*, vol. 140, pp. 93-122, 1998.
- [49] K. Syed, C. Stewart and J. Moss, "Modelling soot formation and thermal radiation in buoyant turbulent diffusion flames, 23rd Symposium (International) on Combustion," *The Combustion Institute Pittsburgh*, vol. 23, p. 1533-1541, 1991.
- [50] Z. Li, F. Wei and Y. Jin, "Numerical simulation of pulverized coal combustion and NO formation," *Chemical Engineering Science*, vol. 58, pp. 5161-5171, 2003.
- [51] J. Moss and G. Cox, "Turbulent Diffusion Flames," *Academic Press*.

- [52] E. Meinders, T. Van Der Meer and K. Hanjalic, "Local convective heat transfer from an array of wall-mounted cubes," *International Journal of Heat and mass transfer*, vol. 41 (2), pp. 335-346, 1998.
- [53] H. Versteeg and W. Malalasekera, *An Introduction to Computational Fluid Dynamics, the Finite Volume Method*, Prentice Hall, 2007.
- [54] J. Nagle and R. Strickland-Constable, "Oxidation of carbon between 1000–2000°C," in *5th Carbon Conference*, London, 1962.
- [55] M. Modest, *Radiative heat transfer*, Academic Press, 2003.
- [56] B. Leonard, "A stable and accurate convective modelling procedure based on quadratic upstream interpolation," *Computer methods in applied mechanics and engineering*, vol. 19(1), pp. 59-98, 1979.
- [57] P. Gresho, R. Lee, R. Sani and T. Stullich, "Time-dependent FEM solution of the incompressible navier-stokes equations in two-and three-dimensions," in *Conference on numerical methods in laminar and turbulent flow*, Swansea, UK, 1978.
- [58] D. Viegas and C. Rossa, "Fireline Rotation Analysis," *Combustion Science and Technology*, vol. 181, p. 1495–1525, 2009.
- [59] N. Frangieh, G. Accary, D. Morvan, S. Meradji and O. Bessonov, "Wildfires front dynamics: 3D structures and intensity at small and large scales," *Combustion and Flame*, vol. 211, pp. 54-67, 2020.
- [60] J. Gillies, W. Nickling and J. King, "Drag coefficient and plant form response to wind speed in three plant species: Burning Bush (*Euonymus alatus*), Colorado Blue Spruce (*Picea pungens glauca.*), and Fountain Grass (*Pennisetum setaceum*)," *Journal of Geophysical Research Atmospheres*, vol. 107(D24), pp. ACL 10-1-ACL 10-15, 2002.
- [61] D. Morvan, "Numerical study of the effect of fuel moisture content (FMC) upon the propagation of a surface fire on a flat terrain," *Fire Safety Journal*, vol. 58, pp. 121-131, 2013.
- [62] K. McGrattan, S. Hostikka, R. McDermott, J. Floyd, C. Weinschenk, and K. Overholt, "Fire Dynamics Simulator, Technical Reference Guide, Volume 1: Mathematical Model," *NIST Special Publication 1018-1, National Institute of Standards, Technology, Gaithersburg, Maryland USA, and VTT Technical Research Centre of Finland, Espoo, Finland*, 2013.
- [63] G. Byram, *Forest fire: Control and Use*, New York: Mc Graw-Hill, 1959.

- [64] C. Bankston, B. Zinn, R. Browner and E. Powell, "Aspects of the mechanisms of smoke generation by burning materials," *Combustion and Flame*, vol. 41, pp. 273-292, 1981.
- [65] V. V. Calmidi, R. L. Mahajan, "Forced Convection in High Porosity Metal Foams," *Journal of Heat Transfer*, vol. 122, 2000.
- [66] I. Ghosh, "Heat-Transfer Analysis of High Porosity Open-Cell Metal Foam," *Journal of Heat Transfer*, Vols. 130/ 034501-1, 2008.
- [67] W. Khan, J. Culham and M. Yovanovich, "Convection heat transfer from tube banks in crossflow: Analytical approach," *International Journal of Heat and Mass Transfer*, vol. 49, p. 4831–4838, 2006.
- [68] K. Moinuddin, N. Khan, D. Sutherland, "Numerical study on effect of relative humidity (and fuel moisture) on modes of grassfire propagation," *Fire Safety Journal*, Vols. 125, October 2021, 103422.
- [69] Y. Perez-Ramirez, P. A. Santoni, J. B. Trameni and F. Bosseur, "Examination of WFDS in Modeling Spreading Fires in a Furniture Calorimeter," *Fire Technology*, vol. 53, pp. 1795-1832, 2017.
- [70] J. Pereira, N. Sequeira, and J. Carreiras, "Structural Properties and Dimensional Relations of Some Mediterranean Shrub Fuels," *International Journal of Wildfire*, vol. 5(1), pp. 35-42, 1995.
- [71] P. A. M. Fernandes, "CARACTERIZAÇÃO DO COMBUSTÍVEL E DO COMPORTAMENTO DO FOGO EM COMUNIDADES ARBUSTIVAS DO NORTE DE PORTUGAL," Masters Thesis, UNIVERSIDADE DE TRÁS-OS-MONTES E ALTO DOURO, VILA REAL, 1997.
- [72] V. Babrauskas and R. Peacock, "Heat Release Rate: The Single Most Important Variable in Fire Hazard," *Fire Safety Journal*, vol. 18, p. 255–292, 1992.
- [73] J. Dupuy and J. Marechal, "Slope effect on laboratory fire spread: contribution of radiation and convection to fuel bed preheating," *International Journal of Wildland Fire*, vol. 20, p. 289–307, 2011.

Appendix A : Junction Point Positions and Dynamic ROS

The junction point position using the averaged fire front position in the midplane of the vegetation zone and its derivative over time (dynamic ROS) are represented in this appendix for various cases of the parametric study of junction fire with and without wind (the horizontal line represents the nominal value of ROS for each case).

